

ADVANCES IN MINIATURE ULTRASOUND-GUIDED HISTOTRIPSY  
TRANSDUCERS FOR PRECISION TISSUE ABLATION

by

Matthew Mallay

Submitted in partial fulfilment of the requirements  
for the degree of Doctor of Philosophy

at

Dalhousie University  
Halifax, Nova Scotia  
February 2024

Dalhousie University is located in Mi'kma'ki, the  
ancestral and unceded territory of the Mi'kmaq.  
We are all Treaty people.

*To my wife, Jasmine,  
for encouraging me to start this journey,  
and my daughter, Emilia,  
for being my inspiration to finish it.*

# TABLE OF CONTENTS

List of Tables .....	vii
List of Figures .....	viii
Abstract.....	xiv
List of Abbreviations and Symbols Used .....	xv
Acknowledgements.....	xvii
Chapter 1: Introduction.....	1
1.1 Research Objective.....	4
Chapter 2: Background .....	7
2.1 Glioblastoma Treatments .....	7
2.2 Minimally Invasive Surgical Approaches .....	10
2.2.1 Endoscopes and Laparoscopic Instruments .....	12
2.2.2 Percutaneous Ablation.....	13
2.2.3 Ultrasonic Surgical Aspirators.....	17
2.2.4 Other Thermal Ablation Technologies.....	18
2.2.5 Radiosurgery.....	19
2.3 Focused Ultrasound Therapy .....	21
2.3.1 High Intensity Focussed Ultrasound (HIFU).....	21
2.3.2 Histotripsy .....	22
2.3.3 Histotripsy Immune Response.....	24
2.4 Ultrasound Transducers .....	25
2.4.1 Piezoelectric Materials .....	26
2.4.2 Focused Ultrasound Transducers.....	33

2.5 Transducer Models.....	39
2.5.1 FEM Model.....	40
2.5.2 KLM Model.....	45
2.5.3 HITU Simulator.....	48
Chapter 3: A Dual Frequency Lens-focused Endoscopic Histotripsy Transducer .....	50
3.1 Preamble .....	50
3.2 Introduction.....	51
3.3 Methods.....	54
3.3.1 Design Summary .....	54
3.3.2 FEM Modelling .....	55
3.3.3 Acoustic Lenses.....	56
3.3.4 Pump Transducer.....	58
3.3.5 Transducer Fabrication.....	60
3.3.6 Ex Vivo Ablation Experiment .....	61
3.4 Results.....	63
3.4.1 Lens Results.....	63
3.4.2 Dual Frequency Transducer Results.....	67
3.4.3 Ex Vivo Ablation Experiment .....	73
3.5 Discussion.....	75
3.5.1 Lens Results.....	75
3.5.2 Dual Frequency Transducer.....	77
3.5.3 Ex Vivo Ablation Experiment .....	77
3.5.4 Future Work.....	79

3.6 Conclusion .....	80
Chapter 4: Evaluation of Piezoelectric Ceramics for Use in Miniature Histotripsy Transducers .....	81
4.1 Preamble .....	81
4.2 Introduction.....	82
4.3 Methods.....	85
4.3.1 Transducer Fabrication .....	85
4.3.2 Transducer Simulations .....	87
4.3.3 Experimental Setup.....	89
4.4 Results.....	93
4.4.1 Electrical Impedance .....	93
4.4.2 Transmit Sensitivity.....	93
4.4.3 Cavitation Threshold in Water .....	95
4.4.4 Saturation.....	96
4.4.5 Failure Test.....	97
4.5 Comparison to Simulations.....	99
4.6 Discussion .....	102
4.7 Conclusion .....	105
Chapter 5: An 8 mm Endoscopic Histotripsy Array with Integrated High-Resolution Ultrasound Imaging .....	107
5.1 Preamble .....	107
5.2 Introduction.....	108
5.3 Methods.....	113
5.3.1 Transducer Design and Fabrication .....	113
5.3.2 Transducer Characterization.....	117

5.3.3 Acoustic Simulations.....	120
5.3.4 Co-registered Histotripsy and Imaging.....	123
5.4 Results.....	124
5.4.1 Low Voltage Characterization.....	124
5.4.2 Cavitation Voltage in Water.....	128
5.4.3 Tissue Phantom.....	131
5.4.4 In Vivo Rat Brain.....	132
5.5 Discussion.....	134
5.6 Conclusion.....	137
Chapter 6: Conclusion.....	139
6.1 Future Work.....	141
Bibliography.....	143
Appendix A: Copyright Permission.....	156

## LIST OF TABLES

Table 2.1: Material properties of PZT-5A ceramic, Spurr epoxy, and 45% volume fraction composite.....	42
Table 3.1: Material properties used in the FEM model.....	56
Table 3.2: Comparison of FEM and measured results for each lens .....	66
Table 4.1: Relevant material properties for each material. The clamped dielectric constants and k33 coupling coefficients from the datasheet for each material are shown for reference. The remaining properties are measured from the fabricated composite materials before bonding the lens or estimated using the KLM model. ....	89
Table 4.2: Summary of Failure Test Results. The transducers marked with an asterisk failed during the saturation measurements. The transducer peak currents were estimated from the measured voltage waveforms and the electrical impedances. ....	98
Table 5.1: Design details of the 16-element annular array. ....	114
Table 5.2: Comparison of acoustic field measurements from annular array and lens-based transducer to FEM simulations.....	127
Table 5.3: Cavitation threshold voltages measured in water and the corresponding surface peak acoustic intensity, acoustic power, and focal pressures from non-linear simulations. ....	130

## LIST OF FIGURES

Figure 2.1: Laparoscopes and instruments with 45 cm and 34 cm lengths (Reprinted from [57]).	13
Figure 2.2: Various percutaneous ablation instruments. (a) Laser ablation diffuser tip and cooling system. (b) Single RF ablation electrode. (c) Expandable electrode for large RF ablations. (d) Monopolar IRE applicator. (Reprinted from [58])	16
Figure 2.3: Example of an ultrasonic surgical aspirator handpiece. The cutting tip is located at the left end of the probe (Reprinted from [73]).	18
Figure 2.4: (a) Gamma knife stereotactic radiosurgery system (Reprinted from [80]). (b) Gamma rays focussed to a target in the brain (Reprinted from [81]).	20
Figure 2.5: HIFU devices with three different form factors: (a) MRI-guided extracorporeal, (b) ultrasound-guided transrectal, and (c) ultrasound-guided endoscopic. (Reprinted from [42])	22
Figure 2.6: Piezoceramic/epoxy 1-3 composite material with copper electrodes.	28
Figure 2.7: Electrical impedance of a piezoceramic composite with resonance and anti-resonance frequency indicated by the dashed lines.	32
Figure 2.8: Three different transducer focussing methods: (left) curved transducer, (middle) acoustic lens, and (right) annular array. The top row shows a cross section of each, with the blue and green lines indicating rays with equal time of flight.	34
Figure 2.9: Diagram showing the transmission of an acoustic wave from one acoustic medium, through a thin layer of a second medium and into a third medium. The transmission coefficient, $T$ , is the ratio of acoustic intensity that is transmitted into the third medium.	38
Figure 2.10: Graphs of the transmission coefficient as a function of the layer thickness normalized by wavelength, for two different sets of acoustic impedances.	38
Figure 2.11: Block diagram of the transducer modelling methodology used in Chapters 3, 4, and 5.	40
Figure 2.12: FEM model geometry for a lens-focussed transducer.	41
Figure 2.13: FEM model geometry after meshing (center), detailed view of the triangular mesh in the lens, matching layer, and water domains (left). Simulated pressure field (right), low pressure amplitude is shown as blue, high pressure is red.	44



Figure 2.14: Comparison of the electrical impedance from the FEM model and measurements, for a composite in air (left), and a finished transducer (right) (reprinted from [100], ©2018 IEEE).....	44
Figure 2.15: Comparison of the measured (left) (reprinted from [100], ©2018 IEEE), and simulated (right) acoustic radiation patterns. ....	45
Figure 2.16: The KLM model for a thickness mode transducer. The equivalent circuit relate the electrical domain to mechanical (acoustic) domain. The equations on the right are used to calculate the circuit component values based on the input parameters.....	47
Figure 2.17: Axial pressure distribution from a 10 mm diameter transducer with 7 mm focal length for various voltage pulse amplitudes. Note the peak positive (blue) and negative pressures (orange) become increasingly asymmetric with increasing voltage. ....	49
Figure 2.18: Non-linear peak positive and negative focal pressure amplitude versus linear pressure amplitude. The highlighted point corresponds to the intrinsic cavitation threshold in water. ....	49
Figure 3.1: Diagram of dual frequency stack with silicone Fresnel lens. ....	55
Figure 3.2: Images of the four lens designs: resin conventional lens (A), resin Fresnel lens (B), silicone conventional lens (C), silicone Fresnel lens (D), and the dual frequency transducer (E). A through D include a section view through the center of each lens (corner to corner). ....	59
Figure 3.3: Measured electrical impedance magnitude and phase from each of the four transducers used to characterize the lens designs.....	63
Figure 3.4: Simulated radiation pattern from the FEM model (left column) compared to a measured radiation pattern (right column) for the silicone conventional (top row) and Fresnel (bottom row) lens transducer. The transducer model geometry is shown at the bottom of FEM model plots. The white rectangles show the area covered by the measured radiation pattern.....	65
Figure 3.5: Measured electrical impedance magnitude and phase from the therapy transducer portion of the dual-frequency devices. ....	67
Figure 3.6: Simulated radiation pattern from the FEM model (left column) compared to a measured radiation pattern (right column) for the dual frequency transducer. The upper row is from the 5 MHz PZT-5A composite therapy transducer (3.6V pulse), while the lower row is from the 1.2 MHz pump transducer (36 V pulse). ....	68

Figure 3.7: Measured pressure waveforms from the PZT-5A composite therapy transducer driven with a 5.2 MHz, 5 V, single cycle pulse (top), pump transducer driven with 1.2 MHz, 5 V, 3 cycle pulse (middle), and the two transducers pulsed together (bottom). The therapy pulse is delayed by 1.7 $\mu$ s to align the peak negative pressures from the two transducers. ....	69
Figure 3.8: Peak negative pressure versus pulse voltage for the therapy transducer in the dual frequency devices. The lower graph shows the low voltage hydrophone measurements and linearized pressure per volt. The upper graph shows measurements from the PMN-PT plate, scaled based on the hydrophone results, with the dashed line showing the extrapolated pressure per volt. ....	70
Figure 3.9: Results from the extrinsic cavitation threshold experiment for both dual frequency devices, showing the therapy transducer drive voltage required to extrinsically cavitate on the surface of the PMN-PT plate for several pump transducer drive voltages. The mean from 5 trials is shown by the line graph, with the error bars showing the standard deviation.....	72
Figure 3.10: A picture of the rat brain ablation experiment. The co-registered imaging (A) and dual frequency histotripsy (B) endoscopes are positioned over the rat brain. The inset picture in the lower right corner shows two small holes (indicated by arrows) created by the histotripsy transducer. ....	74
Figure 3.11: Ultrasound images from the rat brain ablation experiment, with arrows indicating the forward-looking axis of the histotripsy transducer. The left image shows the bubble cloud (A) forming a small lesion in the cerebellum, and the image on the right shows the lesion (B) following a few seconds of histotripsy treatment. ....	74
Figure 4.1: A) Piezoceramic after dicing to produce a grid of pillars. B) Finished 8 mm diameter 1-3 composite. C) Four 8 mm diameter aluminum acoustic lenses, as machined (top row) and after sand etching (bottom row). D) Composite and lens stack-up being pressed in bonding jig. E) Transducers in the case with blue arrows indicating the interposer PCBs. F) Full set of 20 finished transducers.....	86
Figure 4.2: Measured electrical impedance from a PZT-5H composite sample, compared to the simulated impedance from the KLM model after fitting the data. ....	88
Figure 4.3: Block diagram showing the experimental setup for cavitation threshold measurements. ....	92
Figure 4.4: Measured electrical impedance magnitude and phase for one transducer from each material group. ....	93
Figure 4.5: Mean transmit sensitivity versus frequency for each material, with error bars showing the standard deviation. ....	94

Figure 4.6: Data for a single trial from the cavitation threshold experiment for a PZT-5H transducer.....	95
Figure 4.7: Box and whisker plot showing measured cavitation threshold voltage for each material group. The overlaid diamonds show the cavitation threshold voltage predictions for each material, using HITU to non-linearly extrapolate the FEM model sensitivities to the published intrinsic cavitation threshold in water. ....	96
Figure 4.8: Normalized surface pressures recorded using a fiber hydrophone for single cycle pulses (left), and eight cycle pulses (right). ....	97
Figure 4.9: Examples of transducer failures, Parylene delamination (left) and electrode failure (right). ....	99
Figure 4.10: Measured electrical impedance magnitude and phase for one transducer from each material group, compared to the impedance simulated using the FEM model. ....	100
Figure 4.11: Mean transmit sensitivity versus frequency for each material, compared to the simulated transmit sensitivity from the FEM model. The error bars on the measured data show the $\pm 17\%$ hydrophone sensitivity uncertainty. ....	101
Figure 4.12: Surface pressure along the lens from the center to the perimeter of the transducer. Results from the FEM and KLM models are compared. ....	102
Figure 5.1: Concept diagram of an image guided histotripsy device ablating residual tumor during removal of a 40 mm tumor through a 20 mm burr hole. The field-of-view of the ultrasound imaging phased array, the histotripsy focal region and the residual tumor are annotated in the inset image. ....	110
Figure 5.2: Diagram of the new image-guided annular-array histotripsy transducer concept compared to the previously published image-guided lens-focussed transducer. ....	112
Figure 5.3: Linear focal pressure per volt versus focal length for annular arrays with 8, 16, 24 and 32 elements, simulated using FEM. ....	114
Figure 5.4: Fabrication of the forward-looking annular array. (a) Piezoelectric composite with array outline laser diced and elements etched. (b) Two interposer PCBs used to route array elements to cable bundle. (c) Array with interposer PCB bonded to back, with wirebonds used to connect array elements to traces. (d) Array after soldering wires to pads and applying backing epoxy. (e) Array stack and PCB before soldering wires to pads. (f) Finished array with imaging probe attached. ....	116

Figure 5.5: Fabrication of an annular array with a side-looking form factor. (a) Piezoelectric composite after laser dicing outline, etching array elements, and wirebonding elements to traces on the PCB. Small sections of the PCB were used to connect the inner four elements around the hole. (b) Wirebond contact points potted in alumina-loaded epoxy. (c) Front of the array after wirebonding to the ground plane on the PCB. (d) Side view of the finished array.....	117
Figure 5.6: The custom designed 16-channel pulse generator connected to the cable bundle. The motherboard (green) contains an FPGA which was used to trigger N-FETs on the pulser cards (red) with the required beamforming delays to focus the array. ....	119
Figure 5.7: Measured electrical impedance magnitude and phase of each array element. The column on the left shows elements 5 through 15 separately to highlight the excellent grouping observed between array elements. The column on the right shows elements 1 through 4, which have reduced area due to the square hole, and element 16, which appeared to be damaged from laser cutting the array outline.....	125
Figure 5.8: Measured transmit sensitivity compared to FEM model results for the array focussed to several foci, and the lens focussed transducer. Error bars on the measured data represent the $\pm 17\%$ uncertainty of the hydrophone sensitivity.....	126
Figure 5.9: Measured and simulated radiation patterns showing the normalized peak focal pressure of the lens focussed transducer compared to the array focussed to 3 mm, 5 mm, and 7 mm. The vertical axis shows the distance from the surface of the composite, with the dashed line illustrating the maximum thickness of the lens.....	127
Figure 5.10: A typical 5.4-MHz 12-cycle voltage pulse probed across the tuning capacitors at the end of the cable with the high voltage supply set to 195 V.....	129
Figure 5.11: An example probability curve from the cavitation threshold voltage measurement in water for the array focused to 3 mm. The asterisks show the average cavitation percentage across three trials of 100 pulses each, for each drive voltage. The red line is a sigmoid curve fit to this data. The circle indicates the estimated cavitation threshold voltage corresponding to a 50 % cavitation probability.....	129
Figure 5.12. Simulated non-linear focal pressure waveforms at the array focus, using the measured transmit sensitivity (linear focal pressure per volt) and driving voltages corresponding to the cavitation threshold voltages given in Table 5.3. ....	130

Figure 5.13: (Top) Image of the side looking array operating in water with a bubble cloud visible at 3-, 5- and 7-mm focal lengths, composed of separate images for each focal point. (Bottom) Four B-mode images captured during the tissue phantom test, from 3 individual focal lengths and the line pulse sequence. The Doppler signal was overlaid to show the bubble cloud. .... 132

Figure 5.14: *In vivo* rat brain ablation experiment results. (a) B-mode image during ablation with doppler overlay showing bubble cloud. (b) B-mode image of the ablated line after treatment, the endpoints of the line are indicated by the arrows. (c) Composite image of several tissue slices overlaid to show the full extent of the ablated line. The black rectangle highlights the region of interest. .... 133

## ABSTRACT

Histotripsy is a type of focused ultrasound therapy that uses a very high focal pressure to ablate (surgically remove) tumors with high precision, without damaging the surrounding healthy tissue. Unlike other ablation modalities there is no risk of thermal injury or ionizing radiation exposure because it uses the mechanical forces produced by a cavitation bubble cloud to kill cells. Many surgeons are moving toward minimally invasive procedures due to significant benefits compared to open surgery, such as reduced blood loss, shorter hospital stays, less pain and faster recovery times. The goal of this work is to develop a high precision surgical device for minimally invasive neurosurgery that combines ultrasound imaging and histotripsy.

The first study explored a dual frequency (1.2- and 5-MHz) histotripsy transducer with a 5 mm square aperture. The quarter wavelength coupling layer behind the 5 MHz transducer resulted in a pressure output similar to an air backing, while the output from the 1.2 MHz transducer added to the overall focal pressure. The dual frequency device was tested on an *ex vivo* rat brain, ablating tissue at up to 4 mm depth, with lesion sizes as small as 500  $\mu\text{m}$ .

The second study involved evaluating several piezoelectric materials for use in miniature histotripsy transducers. Five piezoelectric ceramics were evaluated, including PZT-5A, PZT-5H (CTS 3203HD), Pz39, Pz54 and PMN-38. 5 MHz, 1-3 dice and fill, piezo/epoxy composites were fabricated for all except Pz39, a low acoustic impedance porous ceramic. For each, four air-backed 8 mm diameter aluminum lens transducers were built and tested. PZT-5H was identified as the best material from this set.

In the third study, an 8 mm diameter annular array histotripsy transducer was fabricated and tested, motivated by eliminating the lens curvature and providing axial focal steering capability. The histotripsy array was designed to be co-registered with a 30 MHz phased array imaging probe. Real time B-mode and Doppler imaging were used to target tissue and monitor ablation progress, while producing an elongated lesion *in vivo* in a rat brain by rapidly steering from 3- to 8-mm. Histology confirmed the targeted tissue was fully homogenized.

## LIST OF ABBREVIATIONS AND SYMBOLS USED

Abbreviation/Symbol	Description
$\alpha$	Attenuation coefficient
$\beta$	Wave number
$c$	Speed of sound
$c^E$	Elastic stiffness matrix
$C_0$	Clamped capacitor
CT	Computed Tomography
CUSA	Cavitron ultrasonic surgical aspirator
$D$	Electric displacement field
$E$	Electric field
E	Young's modulus
$e$	Piezoelectric strain constant matrix
EOR	Extent of resection
$f_a$	Anti-resonance frequency
$f_r$	Resonance frequency
FDA	Food and Drug Administration
FEM	Finite-element method
G	Shear modulus
GBM	Glioblastoma multiforme
GTR	Gross total resection
HIFU	High intensity focussed ultrasound
IEEE	Institute of Electrical and Electronics Engineers
$k$	Electromechanical coupling coefficient
k	Spring constant
KLM	Krimholtz, Leedom, and Matthaei

<b>Abbreviation/Symbol</b>	<b>Description</b>
$\ell$	Layer thickness of thin transmission layer
$\lambda$	Wavelength
LITT	Laser interstitial thermal therapy
MIS	Minimally invasive surgery
MRA	Magnetic resonance angiography
MRgHIFU	MRI-guided transcranial HIFU
MRI	Magnetic resonance imaging
MWA	Microwave ablation
OS	Overall survival
$\varepsilon^S$	Clamped dielectric constant matrix
PML	Perfectly matched layer
PRF	Pulse repetition frequency
RFA	Radiofrequency ablation
$\rho$	Density
$S$	Strain
STR	Subtotal resection
$T$	Stress
$t$	Thickness of piezoceramic (or epoxy layer thickness)
$T_I$	Intensity transmission coefficient
$v$	Piezoceramic volume fraction
$\nu$	Poisson's ratio
WAKZK	Wide-angle Khokhlov-Zabolotskaya-Kuznetsov
$Z$	Acoustic impedance



## **ACKNOWLEDGEMENTS**

I would like to thank:

My supervisors Dr. Jeremy Brown, and Dr. Tom Landry for their incredible support and guidance. I could not have asked for better mentors.

The other members of my supervisory committee, Dr. Rob Adamson, and Dr. James Robar for their feedback during committee meetings, and for getting me to think critically about comparing endoscopic histotripsy to existing surgical techniques.

My colleagues at the Microsonic Lab for creating such a positive and collaborative work environment. A special thanks to, Chris for getting my foot in the door, Jeff for teaching me how to use the lab equipment, Justin for his contributions to Chapter 4, and Nick for our many conversations over a great cup of coffee.

My parents, Agnes and Kevin, and my sister, Nicole, for always being there to listen, and offer advice and encouragement.

## **CHAPTER 1:**

### **INTRODUCTION**

Over the past several decades the field of minimally invasive surgery (MIS) has grown rapidly due to improved postoperative outcomes, including decreased risk of complications, less blood loss and faster recovery times than open surgery [1], [2]. This is especially true when comparing full craniotomies to MIS approaches for brain tumor resection, which typically use a 15 – 25 mm burr hole (often referred to a keyhole) [3], [4]. Endoscopic tools and preoperative planning based on brain imaging, usually magnetic resonance imaging (MRI), allow surgeons to significantly reduce the craniotomy size, leading to less surgical exploration and brain retraction [3], [5].

Craniotomies often result in the brain shifting from the position in the preoperative scans, making them less accurate [6]. Also, other than using optical microscopes and endoscopes, which can only visualize the surface of tissue, these procedures are typically performed with limited intraoperative real-time image guidance. The most commonly used tools for tumor removal are ultrasonic aspirators, such as the cavitron ultrasonic surgical aspirator (CUSA), which have relatively large ablation sizes and lack image guidance [7]. This limitation in combination with brain shift restricts the extent of resection, which is directly related to patient survival and quality of life outcomes [8], [9]. Surgeons also don't want to risk over-resecting into healthy tissue to ensure the cancer is fully removed as this

results in poor quality of life outcomes for the patient. For this reason, residual tumor tissue is often left behind post-surgery [10].

Residual tumour is particularly dangerous for glioblastoma multiforme (GBM) as it is an aggressive form of brain cancer, with a mean patient survival time of only 15 months [11]. It tends to have a diffuse growth pattern, branching out to infiltrate healthy tissue beyond the radiographically visible tumor boundaries, making it difficult to completely resect [12]. While there are other treatments for GBM, such as radiotherapy and more recently laser interstitial thermal therapy (LITT), they still only provide at best a 2 – 6 month improvement to overall survival compared to conventional surgery [13].

Histotripsy is a therapeutic ultrasound approach that is capable of non-thermal, non-ionizing, mechanical tissue ablation. It works by using focussed ultrasound to generate cavitation at a target location; the highly localized strain produced by the expansion and collapse of these bubbles fractures cells, resulting in mechanically homogenized tissue [14]. It was pioneered at the University of Michigan by a group led by Dr. Charles Cain [15], [16], [17]. This ablation method results in minimal cellular damage margins, as small as 100  $\mu\text{m}$  [18], at the boundaries of the ablated region. Additionally, it can be readily monitored using ultrasound imaging in real time due to the high echogenicity of the bubbles. Preclinical research has shown that histotripsy treatment produces a stronger immune response than radiotherapy or thermal ablation and produced an abscopal effect (regression of untreated tumors) [19]. The abscopal effect was also observed in a case report from a preclinical trial on treating liver tumors with histotripsy [20].

In much of the work published to date, a 50 – 145 mm diameter extracorporeal transducer is used to generate the histotripsy pulses at frequencies between 250 kHz and 3 MHz, at focal depths of 70 – 150 mm through soft tissue [17], [21], [22], [23]. This has been investigated in pre-clinical studies for several indications, especially liver cancer [24], [25], [26], [27], [28]. Schuster et al [29] conducted an in-human trial to assess the clinical safety of histotripsy for the treatment of symptomatic benign prostatic enlargement using an extracorporeal 700 kHz, 36 element transducer with an 11 cm focal distance, observed with transrectal ultrasound imaging. Applying histotripsy to neurosurgery is appreciably more challenging due to the presence of the skull, which strongly attenuates the signal and produces aberrations at the focus, reducing accuracy.

There has been significant progress on non-invasive methods of brain tumor ablation in recent years. Transcranial thermal high intensity focussed ultrasound (HIFU) has successfully been used to partially ablate a recurrent glioblastoma tumor with no adverse effects [30]. More recently, transcranial histotripsy has been demonstrated using a 128 element, 700 kHz, MR compatible phased array transducer inside an MRI scanner to treat eight pigs *in vivo*, with a section of the pig skull replaced with a human cadaver skull cap [31]. While this is a very promising step toward a fully non-invasive method of brain tumor ablation, the mean shift between the target and observed ablation zone was 2.3 mm, which could lead to residual tumor or over resection comparable to surgical resection. Also, this surgical approach requires MR imaging to monitor the progress, which is time consuming, expensive, and often has limited availability. Finally, homogenizing large tumour volumes noninvasively could result in high levels of toxicity for the brain without a means of suctioning out the blood.

Ultrasound imaging has been shown to be useful in comparing preoperative and intraoperative anatomic data, and can be used to update navigation based on intraoperatively collected ultrasound images [10], [32]. There is also evidence that it can locate residual tumor, improving patient outcomes [33]. Given these benefits of integrated ultrasound image guidance, and the advantages of histotripsy compared to resection, there is a strong justification for developing an endoscopic form factor device that combines histotripsy ablation with real time high-resolution ultrasound imaging.

Although the development of this device is discussed throughout this work with neurosurgical applications in mind, the further miniaturization image-guided histotripsy devices provide the flexibility to apply histotripsy to more indications. In general, it would be valuable for many procedures where a tumor borders on delicate anatomy that is difficult to avoid using conventional methods and/or is sensitive to thermal damage. The high-resolution ultrasound image guidance could accurately determine the tumor depth so it could be fully ablated without risking over resecting.

## 1.1 RESEARCH OBJECTIVE

The work compiled in this thesis is divided into three sections, with an overall research aim of developing a miniature image guided histotripsy device for minimally invasive neurosurgical applications. While the background section discusses clinical applications of MIS tools, this work is not focussed on the clinical application of miniature histotripsy devices. It is from a technical perspective, concentrating on the engineering challenges of fabricating and evaluating the performance of these devices. The *in vivo* experiments are

used as a proof of concept and not analyzed to the degree that would be expected of a preclinical research paper.

Each section explores a different method of improving the performance of endoscopic form factor histotripsy devices, as shown below:

1. **Explore methods of increasing the pressure output from a 5 x 5 mm lens-focussed histotripsy device.** This work concentrated on exploring several lens designs, as well as modifying the transducer design into a dual frequency acoustic stack. This work is described in Chapter 3 and includes the transducer design, fabrication, simulations, and experimental results.
2. **Evaluate several piezoelectric ceramic materials for use in miniature histotripsy transducers.** This was motivated by the results of the first study, and subsequent experimentation with some higher output piezoelectric materials. One material, Pz39, seemed promising at low voltages but was found to fail regularly at high drive levels. The goal of this study, included in Chapter 4, is to test a selection of piezoelectric materials, to identify ones that can provide a higher output pressure for a given input pulse, while surviving the high voltages required by small histotripsy devices.
3. **Create an 8 mm diameter annular array histotripsy device that fits around the existing 30 MHz ultrasound imaging endoscope.** The objective of this study was to create a flat aperture therapy transducer to simplify acoustic coupling, and to add electronic focal steering for increased ablation rate. The material used to fabricate the array was based on the results from the previous

study. In Chapter 5, the performance of the new array design is described, and compared to a lens-focussed device with the same transmit aperture.

Chapter 2 contains background information that is relevant to the content presented in the main chapters. This is divided into an overview of current glioblastoma treatments, a review of surgical instruments used in minimally invasive surgeries, clinical applications of focussed ultrasound therapy, a basic explanation of piezoelectric materials and focussed ultrasound transducers, and finally an explanation of the transducer modelling approaches used throughout the remaining chapters. As mentioned, Chapters 3 through 5 contain the three main research studies. Finally, Chapter 6 contains a conclusion and recommended future work.

## **CHAPTER 2:**

### **BACKGROUND**

#### **2.1 GLIOBLASTOMA TREATMENTS**

Glioblastoma (GBM) is an especially aggressive form of brain cancer, with no significant improvement to survival rates achieved over the past few decades [13]. The average life expectancy after a diagnosis is between 14 and 16 months, and the recurrence rate is nearly 100% [34]. It has been shown that the overall survival (OS) and progression free survival are directly related to the extent of resection (EOR). For example, a meta-analysis of 37 studies showed a mean 1- and 2-year OS of 56% and 25% for gross total resection (GTR), and 40% and 14% for subtotal resection (STR) [35].

A review of 1229 patients with GBM treated with surgical resection compared GTR with resection of the area surrounding the tumor boundary as identified by T1-weighted MRI. This region is thought to contain invasive cells and is shown by T2 fluid-attenuated inversion recovery (FLAIR) images. Including a significant portion of this region increased the median survival time from 15.5 to 20.7 months, with no increase in complications [36]. This supports the belief that residual tumor tissue is left behind after surgical resection using conventional approaches.

On average, surgical resection extends survival by six to ten months, while post-operative radiotherapy extends survival by 1 year [13]. Although whole brain radiotherapy



is used as an adjunct therapy after surgical resection of GBM, stereotactic radiosurgery is often only used for low-grade gliomas in critical areas of the brain, near the brainstem, or for recurrent/residual tumors [37]. For the treatment of small metastatic brain tumors, radiosurgery has been shown to be equally as effective as resection [38].

Laser interstitial thermal therapy (LITT) has become more common in the past several years for treating recurrent GBM, especially for treating small deep seated tumors [39]. In a meta-analysis on the survival outcomes from LITT treatment for recurrent GBM (after being initially treated with surgical resection), the median OS after LITT treatment was 10.2 months, while the median OS after repeat surgery was 18.5 months. In a study comparing 17 patients treated with LITT to 23 similar patients treated using surgical resection, there were only minor differences between the two modalities in terms of EOR (90.7% vs 95.1%), OS (14.1 months vs 13.8 months) and progression free survival (3.7 months vs 3.3 months) [40].

Early clinical trials studying the treatment of GBM using high intensity focussed ultrasound (HIFU) have been promising. In the first published clinical trial for MRI-guided transcranial HIFU (MRgHIFU), three GBM patients were treated using a single focal spot, but the device power prevented a dose sufficient to achieve thermal coagulation. The only reported side effect was pain during treatment in one patient [41]. In 2014, a case report of partial tumor ablation of a centrally located recurrent GBM using HIFU showed no adverse effects [30]. To date, no clinical trials reporting GBM tumor response, survival, or complications statistics have been published [42]. The relatively low frequency (210 - 860 kHz [43]) used to overcome skull attenuation limits the ablation precision; skull aberrations and brain surface heating restricts tumors that can be treated to those that are

centrally located [41] [30]. Due to the branching nature of GBM tumors, MRgHIFU is likely not the best candidate for improving on surgical outcomes. While there are challenges using MRgHIFU therapy to thermally ablate tumors, it has opened the door for targeted drug delivery in the brain by enabling the localized opening of the blood brain barrier [44].

One of the main challenges during glioma resection is the brain shift associated with opening the dura, making the preoperative MR images inaccurate. Intraoperative MRI has been shown to increase the rate of GTR from 53% to 86%, compared to traditional navigation methods, but this increases surgery time by 1-2 hours, requires compatible tools, and occupies an MRI machine for the entire surgery [13]. 5-Amino-levulinic acid (5-ALA) fluorescence-guidance is another assistive technology for increasing the EOR. A meta-analysis reported a mean GTR of 75.4%, and overall survival of 6.2 months for 5-ALA fluorescence image guided GBM resections [13]. However, intraoperative ultrasound image guidance is a more flexible and lower cost alternative to intraoperative MRI guidance for correcting for brain shift [45].

In a retrospective analysis of navigated ultrasound image-guidance during glioma resection in 210 patients, the addition of ultrasound image guidance resulted in the detection of residual tumor with a sensitivity of 78% and a specificity of 83%. Additionally, intraoperative ultrasound imaging led to additional tumor resection in 42.5% of cases [10]. For ultrasound-guided operations on high-grade gliomas, greater image quality was shown to result in better clinical outcomes [46]. However, using a separate ultrasound imaging probe during tumor removal can interfere with the surgery by restricting the placement of surgical instruments [32]. Based on this it's clear that a surgical instrument combining

high-resolution ultrasound imaging and precision ablation would be an extremely beneficial addition to the existing GBM treatments.

## 2.2 MINIMALLY INVASIVE SURGICAL APPROACHES

This section contains a review of the minimally invasive surgical approaches that are currently used clinically, including typical sizes of the instruments. This is included to provide context and motivation for the miniature histotripsy devices that are discussed in Chapters 3 – 5. While these were developed with neurosurgery in mind, the review in this section is not restricted to that application, to show that miniature image guided histotripsy technology could also be useful for other purposes.

Since its inception in the 1980s, the field of minimally invasive surgery (MIS) has grown in popularity. Over the past few decades MIS has become the standard of care for many procedures, such as cholecystectomies and appendectomies, the vast majority of which are performed using laparoscopic procedures [1]. From 2000 – 2018, Bingmer et al. showed a 462% increase in laparoscopic general surgeries performed by residents [47]. Laparoscopy has been shown to have significant benefits compared to open surgery, such as reduced blood loss, shorter hospital stays, less pain and faster recovery times [2].

While laparoscopic abdominal surgeries are what usually comes to mind when discussing MIS procedures, the philosophy of improving patient outcomes through developing less invasive techniques is becoming the trend in many surgical fields [48]. For example, endoscopic-based procedures for gastrointestinal cancers have gained significant traction. This field originates in 1968, when fibrogastroscopy-guided procedure for removal of gastric polyps was first developed [49]. Endoscopic mucosal resection (EMR)

and endoscopic submucosal dissection (ESD) have become an accepted treatment for early gastric cancers, for tumors up to 3 cm diameter [50]. MIS approaches are also common for colorectal cancers, initially using Parks retractor. This was then improved through the application of transanal endoscopic microsurgery (TEM), and more recently transanal minimally invasive surgery (TAMIS) [51]. Video-assisted thoracic surgery (VATS) for lung cancer has become more prevalent over the past decade, with VATS producing better health-related variables and slightly better survival rate compared to thoracotomy [52]. Advancements in MIS techniques have also made their way into the field of neurosurgery, particularly with keyhole procedures. Here the focus is not only on limiting the size of the craniotomy, but also minimizing damage to normal tissue by selecting the best approach through pre-operative planning based on medical imaging, such as MRI [5]. In many cases of brain metastases, non-invasive stereotactic radiosurgery (SRS) has replaced traditional surgery as the initial treatment option [53].

There are numerous tools specifically designed for minimally invasive surgical procedures, represented by a broad range of sizes and mechanism of action for tumor removal. These include more traditional resection tools such as micro-cutters, micro-forceps, and micro-graspers, that can be employed using endoscopes or laparoscopic form factors. There are also many thermal ablation-based instruments using a variety of technologies to remove tumor tissue using hyperthermic injury, including radio frequency (RF), microwave, focussed ultrasound or laser ablation, as well as cryoablation, which uses liquified gasses to induce cell death through hypothermia [54]. Radiosurgery is a non-invasive treatment option for tumors, especially brain metastases, in which many overlapping sources of radiation directed at the surgical target creating a high dose of

radiation in the tumor while maintaining a safe dose in the surrounding healthy tissue [55]. Finally, irreversible electroporation is one of the newest tumor ablation technologies available. A short pulse of DC current is used to generate an electric field, which causes cell death [54].

### 2.2.1 ENDOSCOPES AND LAPAROSCOPIC INSTRUMENTS

This category of tool is an evolution of traditional surgical instruments miniaturised for MIS. Reducing patient trauma through modifying surgeries to be less invasive produced a significant challenge in creating the tools to make up for the reduced vision and physical operating space and the lack of depth perception and haptic feedback [56]. Figure 2.1 shows two laparoscopes with an appropriate instrument for each.

Advances in technology, particularly in miniature optical cameras, have enabled relatively small multi-functional endoscopes to be used in a number of procedures. Modern endoscopes employ dual high-definition cameras for depth perception, and either LED or xenon bulb illuminated optical fibers as a light source [56]. The outer diameter of surgical endoscopes range in size from about 2 – 5 mm for accessing the sinus, urinary bladder, bile duct or pancreatic duct, to about 5 – 14 mm for the gastrointestinal tract, or abdominal cavity, while proctoscopes can be as large as 23 mm in diameter. Many of these surgical endoscopes have an instrument channel between 1.2 – 6 mm to accommodate various electro-surgical knives, or ablation devices.

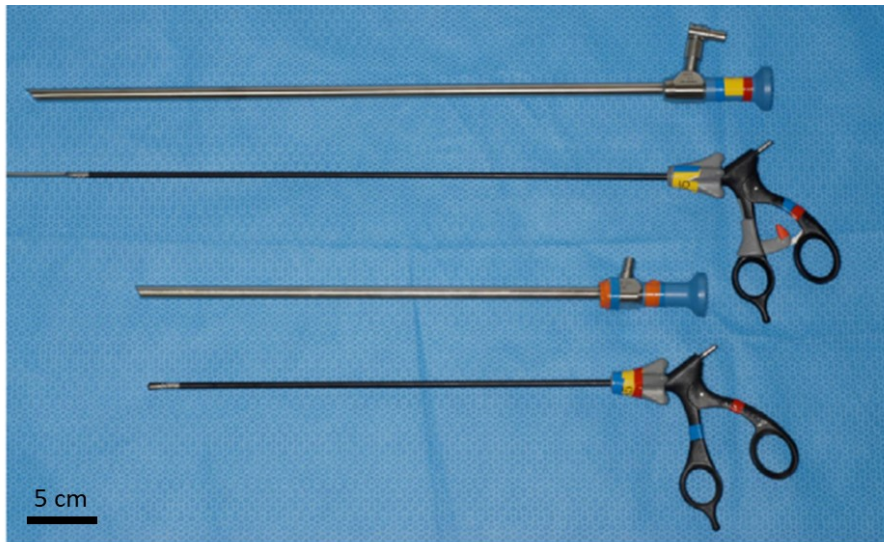


Figure 2.1: Laparoscopes and instruments with 45 cm and 34 cm lengths (Reprinted from [57]).

### 2.2.2 PERCUTANEOUS ABLATION

Percutaneous ablation uses needle-based devices that are inserted into the body to reach and ablate tumors. These methods depend heavily on image guidance and appropriate anatomical access for positioning the applicator. For liver and lung tumors, a margin of 0.5 - 1 cm of healthy tissue is typically included, and for tumors larger than 3 cm in diameter multiple ablation zones are often required for a full treatment [58]. These devices all have similar form factors but use different methods of action.

Thermoablative devices use extreme temperature to destroy cells through either hyperthermic injury, namely radiofrequency ablation (RFA), microwave ablation (MWA) and laser interstitial thermal therapy (LITT), or through hypothermia, also known as cryoablation [54]. Examples of these are shown in Figure 2.2.

Hyperthermic devices heat the tissue surrounding the probe to increase the temperature above 50°C inducing coagulation necrosis. Surrounding this there is a

transition zone with a steep temperature gradient to normal body temperature. Temperatures between 41°C and 45°C result in a reversible heat-induced cell injury, which increases oxygenation and blood flow that improves both tumor cell radiation sensitivity and liposomal chemotherapy drug delivery [54].

RFA uses a 350 - 500 kHz electromagnetic signal to produce resistive heating, generating friction through the movement of ions in the tissue. This method is usually limited to tumors up to 3 cm in diameter, but more recently this has increased to 5 cm. The main limitation of this method is the heat-sink effect of large blood vessels drawing heat away and preventing the tissue near vessels from reaching the necessary temperatures [54].

MWA also uses EM waves to generate heat, but at a much higher frequency of 900 - 2500 MHz. Heat is generated through dielectric hysteresis, from the rotation of polar water molecules following the oscillating field. MWA can reach higher temperatures over a larger volume than RFA, with less susceptibility to the heat sink effect as it doesn't rely on thermal conduction. Microwave power is more difficult to generate and deliver, requiring larger diameter coaxial cables, often with active cooling to prevent shaft heating. This means MWA devices are typically larger diameter than RFA [59].

Laser interstitial thermal therapy (LITT) is similar to RFA and MWA in that it uses a percutaneous probe to deliver electromagnetic energy to generate heat at the tumour site. However, LITT uses laser radiation from either a Nd:YAG (1000-1100 nm) or diode laser (800-980 nm), achieving 2-10 mm penetration depending on the tissue properties. LITT probes are made from quartz or sapphire optical fibers, typically around 600 µm in diameter. They often have a sheath for liquid cooling to prevent the interface between the

probe and tissue from reaching vaporization temperatures. This both increases treatment depth and prevents the probe from fusing to ablated tissue [60].

Cryoablation devices use liquified gasses, such as argon, to drop the temperature at the treatment site to as low as  $-140^{\circ}\text{C}$  through gas expansion at the tip of the probe [58]. The temperature gradient produced results in several distinct regions near the applicator. In the center of the lesion where the temperature drops below  $-40^{\circ}\text{C}$ , there is ice crystal formation and direct cell death. Surrounding this is a region of cell death stemming from reduced blood flow followed by a region of sublethal temperatures leading to a mixture of reversible injury and apoptosis, with a peripheral zone of partly damaged cells [54]. To ensure complete ablation, temperatures between  $-20^{\circ}\text{C}$  and  $-40^{\circ}\text{C}$  have to extend 1 cm past the tumor boundary [61].

There are two common non-thermal percutaneous ablation technologies: chemical ablation and irreversible electroporation (IRE). Chemical ablation has been studied for the longest of all percutaneous techniques, especially for hepatocellular carcinoma. It usually involves the injection of ethanol, called percutaneous ethanol injection (PEI), or less commonly acetic acid. Randomized trials comparing PEI to RFA, showed that RFA has better clinical outcomes [62]. It requires more operations and is more painful compared to thermal ablation, and during injections air bubbles can form, interfering with ultrasound guidance. It does have some advantages: it is a cheaper, low-tech solution, that is relatively safe, and does not suffer from the heat sink effect near large blood vessels [63].

Irreversible electroporation is the newest technology discussed so far. It uses a short high voltage pulse to create a strong electric field (greater than  $800\text{V}/\text{cm}$ ) at the distal end



of a needle probe. When a cell is exposed to a strong electric field nano-sized pores appear in the cell membrane. Up to a certain threshold this process is reversible, meaning a cell can seal the pores. This was studied for many years for applications such as gene therapy. However, if the cells are exposed to a sufficiently strong electric field, they can no longer repair the damage, and die. This technology has become a very promising advancement for treating solid tumors. It does not thermally or chemically damage cells, which means it leaves behind vessels and extracellular matrix promoting faster tissue regrowth [64]. One commercial example, the NanoKnife system, uses a pulse generator to deliver microsecond length pulses (up to 100 pulses with amplitude up to 3000 V and maximum pulse length up to 100  $\mu$ s) to up to 6 electrode probes that are positioned near the tumor [65].

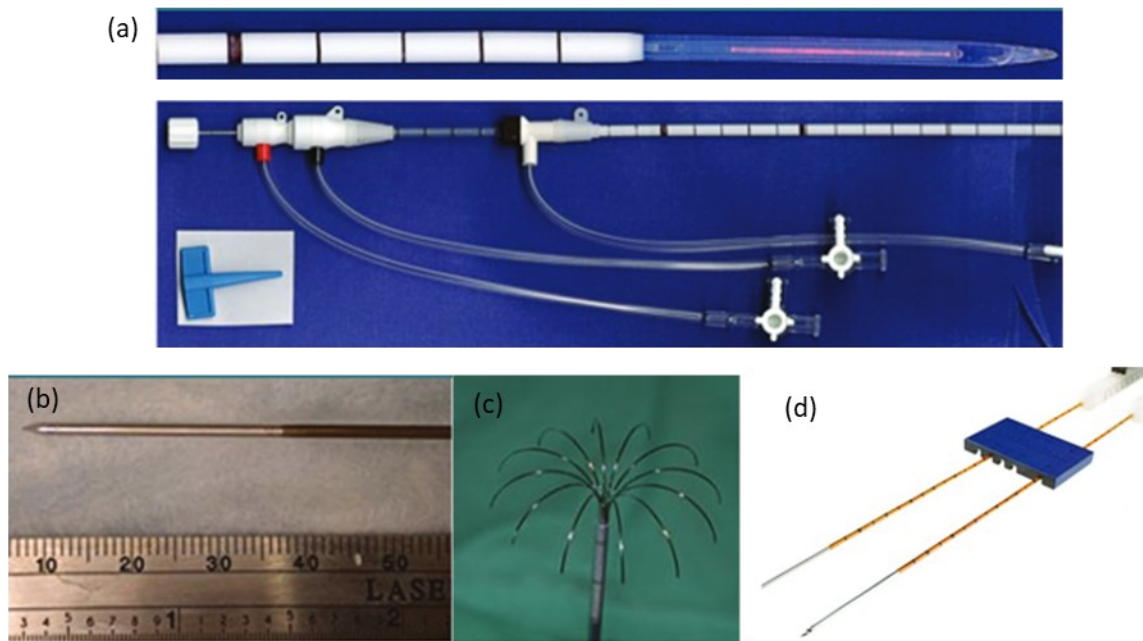


Figure 2.2: Various percutaneous ablation instruments. (a) Laser ablation diffuser tip and cooling system. (b) Single RF ablation electrode. (c) Expandable electrode for large RF ablations. (d) Monopolar IRE applicator. (Reprinted from [58])

### 2.2.3 ULTRASONIC SURGICAL ASPIRATORS

An ultrasonic surgical aspirator, shown in Figure 2.3, uses high amplitude ultrasound vibrations at the tip of a long, narrow probe to remove tissue, most commonly brain or liver tumors. They typically operate at either 24 kHz for fibrous tissue and bone, or 35 kHz for more delicate tissue removal. Common commercial examples include the Styker Sonopet [66], Integra CUSA [67] and Söring HEPACCS/LEVICS [68]. These devices are often all generically referred to as cavitation ultrasonic surgical aspirators (CUSA). When applied to brain surgery they are sometimes called neuroendoscopic ultrasonic aspirators (NUA) [69] or microCUSA [70].

The device is pulsed with an electrical signal which is converted to ultrasound vibrations using a magnetostrictive transducer and coupled to a long hollow rod called a sonotrode. The vibrating rod is surrounded by a rigid sheath, called a flue, that both prevents unintended tissue damage, and is used to irrigate the surgical site. Suction is used to aspirate fluid and debris away from the tip of the probe, through the hole in the sonotrode [71]. The device tips are swappable and come in a variety of designs, ranging from 1.6 - 2.6 mm in diameter, including standard flat tips, angled tips for calcified and fibrous tissue, and bone cutting tips. For brain applications, the ultrasonic aspirator MIS is often guided using either a separate endoscope for optical imaging, or a flue-less aspirator can be inserted through the instrument channel in a rigid endoscope with integrated irrigation [69]. Neuro-navigation systems can also be used to overlay preoperative MRI to assist the surgeon. For liver procedures, intraoperative ultrasound can also be used to provide better probe positioning [72].



Figure 2.3: Example of an ultrasonic surgical aspirator handpiece. The cutting tip is located at the left end of the probe (Reprinted from [73]).

#### 2.2.4 OTHER THERMAL ABLATION TECHNOLOGIES

Two emerging technologies for thermal ablation which still haven't seen significant clinical adoption are magnetic hyperthermia (MHT) and nanoparticle-mediated photothermal therapy (PTT). MHT is approved as an adjuvant therapy for recurrent Glioblastoma (GBM) in combination with Radiotherapy (RT). In MHT treatment, magnetic nanoparticles are deposited, and an alternating magnetic field is applied generating heat through magnetic hysteresis losses. However, there is still limited data on magnetic nanoparticle safety in humans, and it cannot be monitored using MRI because it causes artifacts [74]. In nanoparticle-mediated PTT, plasmonic nanoparticles are delivered to a tumor which are designed to produce heat by optimally absorbing near-infrared light (650 – 1350 nm) using a source outside the body to penetrate up to 10 cm of tissue [75].

### 2.2.5 RADIOSURGERY

Radiotherapy (RT) uses an external radiation source to deliver beams of either photons (gamma rays), protons, or electrons to tumors. Photons are the most commonly used particles as they penetrate deep into the body and are cheaper to generate. Proton beams can also penetrate deep and have the added benefit of stopping at the tumor, sparing posterior tissue but are more difficult to generate. Electron beams can only travel a short distance through tissue (less than 6 cm), making them ideal for applications such as skin cancer, and shallow tumors in front of critical parts of the body such as face and neck, or breast. This is referred to as modulated electron radiation therapy (MERT) [76]. In recent years RT was used to treat about 60-70% of newly diagnosed cancer patients. Radiation therapy works by damaging cell DNA, killing cells that are actively dividing. Since cancer cells divide more frequently than healthy cells, they are preferentially targeted. RT doses range from 1 – 4 Gy per fraction (a single session of the overall treatment plan) with total doses of 60 – 70 Gy [77].

Multiple external radiation sources can also be focussed to a volume to deliver a much higher dose locally, while minimizing the dose to surrounding healthy tissue. This technique is called radiosurgery (RS), specifically stereotactic radiosurgery (SRS) when applied to the brain, and stereotactic body radiotherapy (SBRT) or stereotactic ablative radiotherapy (SABR) when applied elsewhere in the body. In RS the patient is immobilized, and stereotactic registration and CT or MRI imaging is used to position the tumor in the center of the overlapping beams (usually 10 or more) while avoiding radiation sensitive normal tissue structures [78]. A typical dose for SRS is 18 – 25 Gy in a single fraction, and for SABR is 40 – 60 Gy in 1 – 5 fractions. The first SRS system, the Gamma

Knife, was produced in 1967 and was used for treating metastatic brain tumors. Then in the 1990s a more complex system called CyberKnife was created, which paved the way for extracranial applications such as inoperable early-stage lung cancer [77].

The three main categories of devices used in RS are the linear accelerator (LINAC), the Gamma Knife (GKR), shown in Figure 2.4, and the proton beam therapy (also known as charged particle irradiation). LINAC devices use a single x-ray or electron beam radiation source mounted to a gantry that can swing in arcs around the patient to sum the dose accumulated at the convergence point (called the isocenter). Gamma Knife uses 192 fixed, highly collimated cobalt-60 ( $^{60}\text{Co}$ ) sources positioned along a sphere surrounding the patient to produce a similar dose distribution to a LINAC. It uses a two-stage method for collimating the beams, one attached to the sources, and another located on a helmet-style stereotactic frame that the patient wears that is precisely aligned with the first. Charged particle irradiation devices use the same arc method as LINAC, but the accelerators are significantly larger and use stronger magnets [79].

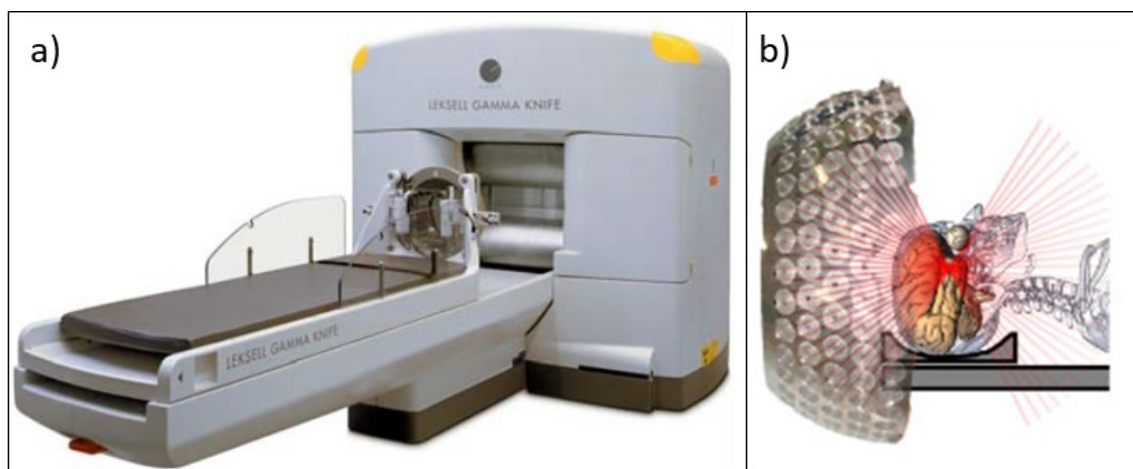


Figure 2.4: (a) Gamma knife stereotactic radiosurgery system (Reprinted from [80]). (b) Gamma rays focussed to a target in the brain (Reprinted from [81]).

## 2.3 FOCUSED ULTRASOUND THERAPY

### 2.3.1 HIGH INTENSITY FOCUSED ULTRASOUND (HIFU)

HIFU therapy is performed by focussing ultrasound waves to produce a high intensity within a small volume ( $0.1 - 10 \text{ kW/cm}^3$ ) using a continuous wave or high duty cycle pulse. Absorption of the acoustic energy at the focus causes rapid tissue heating, leading to coagulation necrosis of cells. Ultrasound can be focused by using a concave piezoelectric transducer element, a flat element focussed by an acoustic lens, multiple elements arranged in a bowl shape, or a flat phased array.

Clinical HIFU transducers can be divided into three main categories: extracorporeal, transrectal, and interstitial. Extracorporeal transducers range in size from about 120 – 370 mm diameter, with a focal length of 90 – 255 mm, operating at a frequency of 0.8 – 3 MHz. Transrectal HIFU probes have approximate cross-sectional dimensions of 30 – 40 mm by 22 mm, with a focal length of 38 – 45 mm, operating at 3 – 4 MHz [82]. Interstitial devices use even smaller transducers incorporated into endoscopes, laparoscopes, or catheters. The device can be rotated using MRI or fluoroscopic guidance to ablate larger volumes [42]. Examples of each are shown in Figure 2.5.

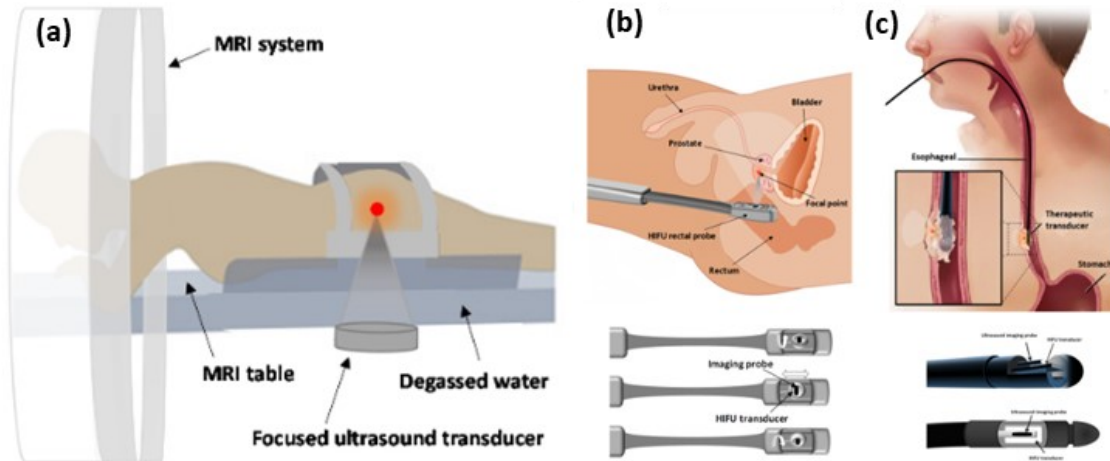


Figure 2.5: HIFU devices with three different form factors: (a) MRI-guided extracorporeal, (b) ultrasound-guided transrectal, and (c) ultrasound-guided endoscopic. (Reprinted from [42])

### 2.3.2 HISTOTRIPSY

Histotripsy is a focussed ultrasound based, non-thermal therapeutic modality. It is similar to HIFU but uses much higher amplitude peak negative pressures ( $> 24.8\text{-}30.6$  MPa), at a low duty cycle ( $< 1\%$ ) to produce a cavitation bubble cloud at the focus that mechanically ablates tissue [83]. Histotripsy is commonly referred to as a completely non-invasive ablation modality because most of the pre-clinical research to date has used extracorporeal transducers to produce lesions at the focal zone.

Due to frequency dependent tissue attenuation and non-linear acoustic propagation, the selection of ultrasound frequency determines the maximum operating depth. The frequency also dictates the ablation spot size and precision. Higher frequencies have reduced operating depth, smaller ablation spot size, but higher precision with fewer extraneous bubbles [84]. For this reason, these devices usually operate between 500 kHz and 3 MHz, to achieve depths between 3.6 cm – 7.8 cm [85]. For example, the first clinical

trial for liver tumor ablation used a 700 kHz array, to produce a 4 mm x 4 mm x 8 mm bubble cloud, which was moved to ablate a volume with ~2.5-3 cm greatest dimension, ~5.6 cm from the skin surface. This first in-human clinical study involved treating 8 patients with incurable liver cancer, and all patients were treated successfully with no reported complications. The median difference between planned ablation volume and actual ablation volume was only 3.2 mm<sup>3</sup> [86].

Endoscopic applications of histotripsy have been studied to a lesser extent. Reducing histotripsy transducers to an endoscopic form factor requires a higher operating frequency to increase the focal gain. The focal depth is related to the transducer diameter by the f-number (focal length/diameter), which is typically between 0.5 – 1 [14]. This leads to a design trade-off: reducing the diameter allows a device to potentially be used in more MIS procedures and increases precision, but reduces the operating depth and ablation rate.

To date there have been limited publications on endoscopic histotripsy devices. The first histotripsy device that could be considered endoscopic, was a 6 MHz, 10 mm diameter aluminum lens focussed transducer with a 4 mm square hole in the center to accommodate a high frequency ultrasound imaging array [1]. The 10 mm ultrasound guided histotripsy device was used to ablate *in vivo* rat brain tissue with extremely high precision, monitored in real-time using ultrasound imaging, supporting the potential of endoscopic histotripsy [4]. This device yielded an ellipsoidal ablation spot size of ~0.94 mm by 0.44 mm with a maximum 0.1 mm zone of cellular damage surrounding the ablated tissue, and a working distance of 3.6 mm.



### 2.3.3 HISTOTRIPSY IMMUNE RESPONSE

One of the most exciting aspects of histotripsy and what can potentially set it even further apart from the other competing ablation modalities is the systemic antitumor immune response associated with treating tumors with cavitation. Histotripsy ablation of melanoma tumors in mice generated a stronger immune response compared to radiotherapy or thermal ablation, and produced an abscopal effect (inhibited untreated tumor growth), which was not seen after the other ablation modalities [87]. This included an upregulation of dendritic cells, which were found to decrease after surgical resection of primary tumors in mice, promoting growth of metastatic tumors [88]. This abscopal effect was also observed in a case report from a histotripsy liver ablation clinical trial [20]. In a refractory neuroblastoma murine tumor model, combining histotripsy ablation with two checkpoint inhibitor therapy drugs was found to increase long term survival rate to 62.5%, compared to 10% using the drugs alone, with no distant metastases [89]. In a recent study by Worlikar et al, 11 rats were inoculated with orthotopic, immunocompetent, metastatic HCC tumors (McA-RH7777). After 7 – 9 days, the 5 – 10 mm tumors were partially ablated (~50 – 75%) using ultrasound guided histotripsy. In nine rats the remaining tumor completely regressed with no recurrence or metastasis over the 12-week period. In the entire untreated control group of 11 rats the tumor progressed, and metastases were observed [90].

Although some researchers have observed increased immune response after thermal ablation therapy [54], two studies have shown evidence of incomplete thermal ablation actually promoting metastasis of HCC tumors in mice. In a 2017 study HCCLM3-G and HepG2-G tumors were implanted in 32 mice, half were treated with incomplete RFA 14 days after implantation and half received a sham treatment (a needle inserted without

ablation). The incomplete RF ablated HCCLM3-G group had a much higher rate of intrahepatic and lung metastasis. The number of lung metastases was compared using hematoxylin-eosin staining and was found to be 26.33 in the treated group and 3.50 in the control group [91]. A 2020 study found similar results using colorectal cancer cell lines injected into the spleen of mice. They injected the tumor cells 24 hours before thermal ablation of the liver using RFA. For both cell lines the mean tumor load was about a factor of 2 higher in the RFA group compared to the control [92].

If histotripsy is as effective at inducing an anti-cancer immune response as pre-clinical studies and initial clinical trials for HCC have suggested, histotripsy could become the ablation modality of choice for many cancers and combined with immunotherapy drugs as part of a larger treatment strategy.

## 2.4 ULTRASOUND TRANSDUCERS

This background section includes the ultrasound transducer theory necessary to give additional context to the content presented in Chapters 3, 4 and 5 of this thesis. Ultrasound transducer theory is a very broad topic, so the focus will only be on the content required to get a basic understanding of focussed therapy transducers fabricated using piezoelectric composite materials operating in the thickness mode and focussed either using an acoustic lens or an annular array.

Although a phased array ultrasound imaging transducer is used in Chapters 3 and 5, this is secondary to the main focus of the work, and thus will not be included in the background. If the reader requires more background on phased array transducers and/or

ultrasound imaging techniques, including B-mode and Doppler imaging, they should consult the following reference [93].

#### 2.4.1 PIEZOELECTRIC MATERIALS

The direct piezoelectric effect was discovered by the Curie brothers in 1880 [94], who demonstrated that certain crystals such as quartz, Rochelle salt, and tourmaline produced a voltage due to an applied mechanical force. It was soon shown that these materials also can produce a mechanical force due to an applied voltage, known as the inverse piezoelectric effect. In general, piezoelectric materials are those which exhibit an ability to convert electrical energy to mechanical energy, and vice versa. This property stems from the intrinsic crystal structure; dipoles within the material are re-oriented to produce an electric field as a result of applied force, or a mechanical force from an applied electric field.

This technology was first applied during World War I by Dr. Paul Langevin, who developed a 40 kHz transducer for submarine detection, consisting of a layer of quartz pellets sandwiched between two steel plates. During World War II, barium titanate ceramics were discovered by researchers in the United States, Japan, and Russia independently. It was soon discovered by R. B. Gray that the polycrystalline barium titanate ceramic became piezoelectric when it was poled electrically [95]. This led to the most widely used piezoelectric ceramic material: lead zirconate titanate (PZT).

In general, piezoelectric materials can be represented by a pair of constitutive equations relating the stress ( $T$ ), strain ( $S$ ), electric field ( $E$ ), and electric displacement field ( $D$ ) throughout the material, shown in Equation 2.1 and 2.2. For a material with three spatial dimensions, there are 6 components in the stress and strain tensors, three

corresponding to the spatial dimensions (annotated 1, 2 and, 3) and three for the shear components (annotated 4, 5 and, 6). There are many different forms of the equations, and notation for the coefficients and variables. The stress-charge form will be used throughout this work, as this form is used by Smith and Auld in the paper that is the foundation for the FEM modelling technique. This form uses the elastic stiffness matrix ( $c^E$ ), piezoelectric strain constant matrix ( $e$ ) and the clamped dielectric constant matrix ( $\varepsilon^S$ ).

$$\mathbf{T} = c^E \mathbf{S} - e^T \mathbf{E} \quad (2.1)$$

$$\mathbf{D} = e \mathbf{S} - \varepsilon^S \mathbf{E} \quad (2.2)$$

Most ultrasound transducer applications use thin piezoelectric plates that are poled and electrically pulsed in the thickness dimension, designated the 3 direction. This is the case for all transducers discussed in this work. The act of poling the ceramic introduces many zeros to the matrix, and significantly reduces the number of independent coefficients as shown in Equation 2.3.

$$\begin{bmatrix} T_1 \\ T_2 \\ T_3 \\ T_4 \\ T_5 \\ T_6 \\ D_1 \\ D_2 \\ D_3 \end{bmatrix} = \begin{bmatrix} c_{11}^E & c_{12}^E & c_{13}^E & 0 & 0 & 0 & 0 & 0 & -e_{31} \\ c_{12}^E & c_{11}^E & c_{13}^E & 0 & 0 & 0 & 0 & 0 & -e_{31} \\ c_{13}^E & c_{13}^E & c_{33}^E & 0 & 0 & 0 & 0 & 0 & -e_{33} \\ 0 & 0 & 0 & c_{44}^E & 0 & 0 & 0 & -e_{15} & 0 \\ 0 & 0 & 0 & 0 & c_{44}^E & 0 & -e_{15} & 0 & 0 \\ 0 & 0 & 0 & 0 & 0 & c_{66}^E & 0 & 0 & 0 \\ 0 & 0 & 0 & 0 & e_{15} & 0 & \varepsilon_{11}^S & 0 & 0 \\ 0 & 0 & 0 & e_{15} & 0 & 0 & 0 & \varepsilon_{11}^S & 0 \\ e_{31} & e_{31} & e_{33} & 0 & 0 & 0 & 0 & 0 & \varepsilon_{33}^S \end{bmatrix} \begin{bmatrix} S_1 \\ S_2 \\ S_3 \\ S_4 \\ S_5 \\ S_6 \\ E_1 \\ E_2 \\ E_3 \end{bmatrix} \quad (2.3)$$

$$\text{where } c_{66}^E = \frac{1}{2}(c_{11}^E - c_{12}^E)$$

Instead of using a solid (a.k.a. monolithic) piezoelectric material, a piezoelectric composite can be used to improve the performance of a specific vibrational mode, and better tailor the material to the application. These composite materials combine a piezoelectric material (often ceramics such as PZT) with a polymer (such as an epoxy resin). This also lowers the acoustic impedance, which is advantageous in terms of matching the transducer to the body for more efficient energy transfer. Composite structures are classified using the concept of connectivity. This is based on the number of dimensions in which a continuous line could be used to connect two parallel faces, while travelling through only one of the materials. The composite connectivity is denoted as two numbers separated by a hyphen, such as 2-2, 1-3 or 3-0, where the first number corresponds to the piezoceramic and the second to the epoxy. Composites with 1-3 connectivity are commonly used for thickness mode ultrasound transducers. These are often fabricated by cutting the ceramic into a grid of pillars using a dicing saw and filling the gaps (kerfs) with epoxy, this is referred to as a dice-and-fill composite. An example of a 1-3 dice-and-fill composite is shown in Figure 2.6.

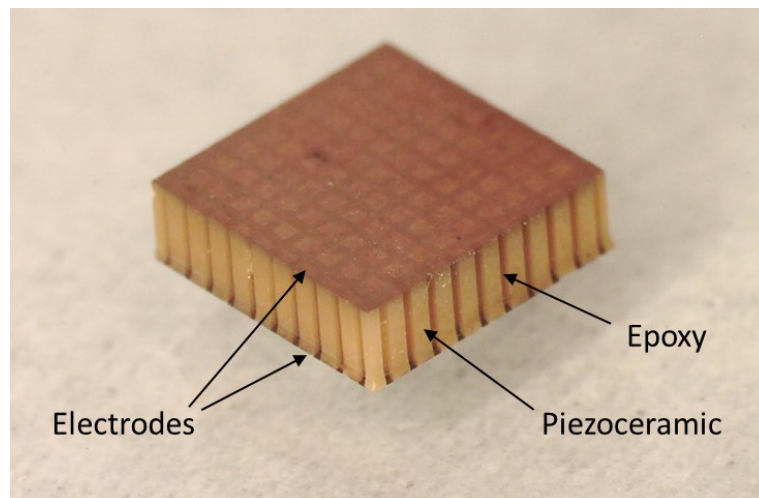


Figure 2.6: Piezoceramic/epoxy 1-3 composite material with copper electrodes.

To increase the thickness mode performance of piezoelectric materials, a 1-3 composite structure is commonly used. In these piezo composites, the structures are sufficiently small so that they act like an equivalent homogeneous piezoelectric material, with the values for the elasticity, coupling and permittivity matrices calculated based on equations derived by Smith and Auld [96] using a series of approximations for a 1-3 composite structure vibrating in the thickness mode. One simplification is that for the homogenous combination of the composite and epoxy phases, only the strain in the thickness mode is considered. The lateral strains ( $S_1$  and  $S_2$ ) are assumed to be zero on average throughout the composite, as the ceramic strain has a complementary strain in the epoxy fill. This implies that the  $c_{11}^E$  and  $c_{12}^E$  can be set to zero. Symmetry in the lateral direction also means that  $E_1 = E_2 = 0$ , which eliminates the  $\varepsilon_{11}^S$  component. Another assumption is that the shear strains ( $S_4$ ,  $S_5$  and  $S_6$ ) can be set to zero, meaning  $c_{44}^E$ ,  $c_{66}^E$ , and  $e_{15}$  can all be set to zero.

This leads to the greatly simplified matrix, shown in Equation 2.4, for an equivalent homogenous piezoelectric material that models the 1-3 piezo/epoxy composite. Equations 2.5 through 2.9 give the formulae for calculating the matrix elements for the composite material based on the parameters for the individual materials, where the overbar indicates the parameter corresponds to the equivalent material. Note, in these equations, the variable “ $v$ ” is the volume fraction of the piezoceramic and  $\tilde{v} = (1 - v)$ . The density of the composite material ( $\bar{\rho}$ ) can be simply calculated using the density of the piezoceramic and the epoxy, and the volume fractions.

$$\begin{bmatrix} T_1 \\ T_2 \\ T_3 \\ T_4 \\ T_5 \\ T_6 \\ D_1 \\ D_2 \\ D_3 \end{bmatrix} = \begin{bmatrix} 0 & 0 & \bar{c}_{13}^E & 0 & 0 & 0 & 0 & 0 & 0 & -\bar{e}_{31} \\ 0 & 0 & \bar{c}_{13}^E & 0 & 0 & 0 & 0 & 0 & 0 & -\bar{e}_{31} \\ \bar{c}_{13}^E & \bar{c}_{13}^E & \bar{c}_{33}^E & 0 & 0 & 0 & 0 & 0 & 0 & -\bar{e}_{33} \\ 0 & 0 & 0 & 0 & 0 & 0 & 0 & 0 & 0 & 0 \\ 0 & 0 & 0 & 0 & 0 & 0 & 0 & 0 & 0 & 0 \\ 0 & 0 & 0 & 0 & 0 & 0 & 0 & 0 & 0 & 0 \\ 0 & 0 & 0 & 0 & 0 & 0 & 0 & 0 & 0 & 0 \\ 0 & 0 & 0 & 0 & 0 & 0 & 0 & 0 & 0 & 0 \\ \bar{e}_{31} & \bar{e}_{31} & \bar{e}_{33} & 0 & 0 & 0 & 0 & 0 & 0 & \bar{\varepsilon}_{33}^S \end{bmatrix} \begin{bmatrix} S_1 \\ S_2 \\ S_3 \\ S_4 \\ S_5 \\ S_6 \\ E_1 \\ E_2 \\ E_3 \end{bmatrix} \quad (2.4)$$

$$\bar{\varepsilon}_{33}^S = v \left[ \varepsilon_{33}^S + \frac{2\tilde{v}(e_{31})^2}{v(c_{11} + c_{12}) + \tilde{v}(c_{11}^E + c_{12}^E)} \right] + \tilde{v}\varepsilon_{11} \approx v\varepsilon_{33}^S \quad (2.5)$$

$$\bar{c}_{13}^E = \frac{vc_{13}^E(c_{11} + c_{12}) + \tilde{v}c_{12}(c_{11}^E + c_{12}^E)}{v(c_{11} + c_{12}) + \tilde{v}(c_{11}^E + c_{12}^E)} \quad (2.6)$$

$$\bar{c}_{33}^E = v \left[ c_{33}^E - \frac{2\tilde{v}(c_{13}^E - c_{12})^2}{(c_{11} + c_{12}) + \tilde{v}(c_{11}^E + c_{12}^E)} \right] + \tilde{v}c_{11} \quad (2.7)$$

$$\bar{e}_{31} = \frac{ve_{31}(c_{11} + c_{12})}{v(c_{11} + c_{12}) + \tilde{v}(c_{11}^E + c_{12}^E)} \quad (2.8)$$

$$\bar{e}_{33} = v \left[ e_{33} - \frac{2\tilde{v}e_{31}(c_{13}^E - c_{12})}{v(c_{11} + c_{12}) + \tilde{v}(c_{11}^E + c_{12}^E)} \right] \quad (2.9)$$

While this detailed description of the material can be useful for FEM modelling, piezoelectric material parameters are often further simplified by eliminating  $\bar{e}_{31}$  and  $\bar{c}_{13}^E$ , which have minimal effect, and calculating the speed of sound ( $c$ ), and electromechanical coupling coefficient ( $k_t$ ), as given in Equations 2.10 and 2.11. This along with the dielectric constant and density are the parameters required to model the transducer using the KLM method that will be discussed later.

The electromechanical coupling factor,  $k$ , is a measure of the effectiveness of conversion between electrical energy and mechanical energy, and vice versa. For the inverse piezoelectric effect, the coupling factor is the square root of the ratio between the mechanical energy produced divided by the input electrical energy. There are several different definitions of the electromechanical coupling factor, indicated by the sub-script. For monolithic piezoceramics, manufacturers specify a thickness mode (clamped) coupling factor,  $k_t$ . They also provide a free coupling factor, referred to as  $k_{33}$ , which is the ideal coupling factor assuming no lateral clamping, or in other words it is the theoretical limit for a 1-3 composite material. Depending on the volume fraction and fill material, the effective coupling factor ( $k_{\text{eff}}$ , or often just  $k_t$ ) for a composite material will fall somewhere between the two values.

$$c = \sqrt{\frac{\bar{c}_{33}^D}{\bar{\rho}}} = \sqrt{\frac{\bar{c}_{33}^E + \frac{(\bar{e}_{33})^2}{\bar{\epsilon}_{33}^S}}{\bar{\rho}}} \quad (2.10)$$

$$k_t = \frac{\bar{e}_{33}}{\sqrt{\bar{c}_{33}^D \bar{\epsilon}_{33}^S}} = \frac{\bar{e}_{33}}{\sqrt{\bar{c}_{33}^E \bar{\epsilon}_{33}^S + (\bar{e}_{33})^2}} \quad (2.11)$$



One of the fundamental ways of characterizing a piezoelectric transducer is by measuring the electrical impedance (magnitude and phase) across a range of frequencies. An example of this is shown in Figure 2.7 for a 1-3 composite, with the transducer resonance ( $f_r$ ) and anti-resonance frequencies ( $f_a$ ) annotated. For thickness mode focussed ultrasound transducers, the thickness of the piezo material is selected based on the desired operational frequency, typically the resonance frequency. To design a composite for a specific resonance frequency given a known speed of sound and coupling factor, Equation 2.12 can be substituted into Equation 2.13 and solved to determine the thickness.

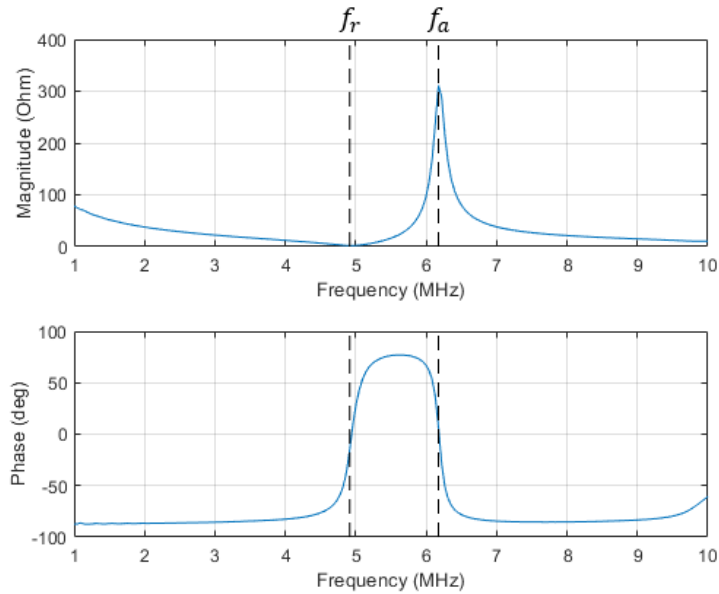


Figure 2.7: Electrical impedance of a piezoceramic composite with resonance and anti-resonance frequency indicated by the dashed lines.

$$f_a = \frac{c}{2t} \quad (2.12)$$

$$k_t = \sqrt{\left(\frac{\pi f_r}{2f_a}\right) \tan\left[\frac{\pi(f_a - f_r)}{2f_a}\right]} \quad (2.13)$$

The approach taken thus far is from the perspective of starting with known material properties for the piezoceramic and the epoxy. Although, given the variation in material properties in practice, when designing a composite, it is common to start from an educated guess for the speed of sound and coupling factor and fabricate a sample composite. Then the resonance and anti-resonance frequencies measured from the electrical impedance curve can be used to calculate the speed of sound and coupling factor, using Equations 2.12 and 2.13. The value of  $\bar{\epsilon}_{33}^S$  can be estimated from the impedance at frequencies below resonance, which will be clarified more in the KLM modelling section. From this it is possible to work backwards to obtain estimates of  $\bar{c}_{33}^E$ , and  $\bar{e}_{33}$  using Equations 2.14 and 2.15. This is useful for creating an FEM model when starting from an existing composite material, when the detailed material properties are unknown.

$$\bar{e}_{33} = c k_t \sqrt{\bar{\rho} \bar{\epsilon}_{33}^S} \quad (2.14)$$

$$\bar{c}_{33}^E = \bar{\rho} c^2 (1 - k_t^2) \quad (2.15)$$

#### 2.4.2 FOCUSED ULTRASOUND TRANSDUCERS

The ultrasound waves generated by the piezoelectric material must be focussed to a point to produce the high peak pressures required by histotripsy. There are several methods of accomplishing this including curved (bowl) transducers, acoustic lenses, and array beamforming. Examples of these focussing methods are shown in Figure 2.8.

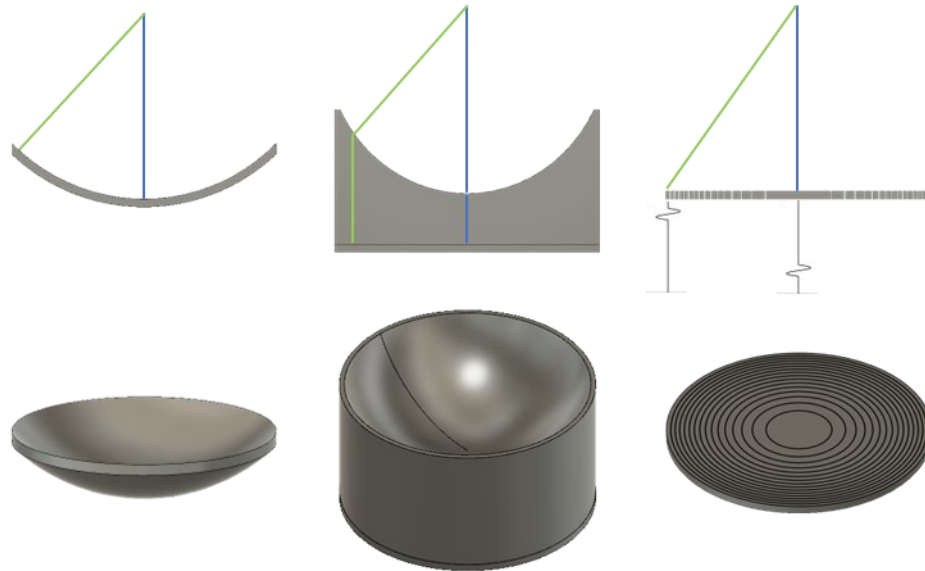


Figure 2.8: Three different transducer focussing methods: (left) curved transducer, (middle) acoustic lens, and (right) annular array. The top row shows a cross section of each, with the blue and green lines indicating rays with equal time of flight.

In general, all of these methods rely on designing the transducer so that the acoustic wave from every point along the surface arrive at the focus at the same time. Bowl transducers have a spherical shape, meaning that the distance between the piezo and the focus is constant across the surface. Piezoceramics can be manufactured in this shape, or less commonly composites can be physically curved.

Lens-focussed transducers use a flat piezoelectric plate and rely on the difference in speed of sound between the lens material and the water (or tissue). The example shown in Figure 2.8 is for an aluminum lens. Aluminum has a speed of sound ( $c_L = 6320$  m/s), much greater than water ( $c_w = 1500$  m/s), meaning that a concave lens is required. To arrive at the equation for the lens height ( $y$ ), as a function of radial position ( $x$ ), we start with Equation 2.16 which is used to represent the constant time of flight for a ray travelling from the bottom of the curvature ( $x=0$ ) directly to the focus ( $y_f$ ), and a ray travelling

perpendicular from the piezo to the lens curvature at an arbitrary (x, y) position, then following a direct path to the desired focus. Solving this equation for “y” yields Equation 2.17, which can be used to calculate the lens height.

$$\frac{y_f}{c_w} = \frac{y}{c_L} + \frac{\sqrt{x^2 + (y_f - y)^2}}{c_w} \quad (2.16)$$

$$y = \frac{\sqrt{y_f^2 c_L^2 (c_w - c_L)^2 + x^2 c_L^2 (c_w^2 - c_L^2) + y_f c_L (c_w - c_L)}}{(c_w^2 - c_L^2)} \quad (2.17)$$

Lens materials with a lower speed of sound, such as silicone, result in a convex lens shape, as illustrated in Chapter 3. This lens type requires a more complicated formula, shown in Equation 2.19, which is derived in the same way, but using the time of flight from the outer point on the lens curvature in the formula ( $x = r$ , where r is the lens radius), as shown in Equation 2.18.

$$\frac{\sqrt{r^2 + y_f^2}}{c_w} = \frac{y}{c_L} + \frac{\sqrt{x^2 + (y_f - y)^2}}{c_w} \quad (2.18)$$

$$y = \frac{-\sqrt{c_L^2 (2y_f c_L - 2c_w \sqrt{y_f^2 + r^2})^2 + 4c_L^2 (c_w^2 - c_L^2) (x^2 - r^2)} - c_L (2y_f c_L - 2c_w \sqrt{y_f^2 + r^2})}{2(c_w^2 - c_L^2)} \quad (2.19)$$

There is another type of lens design called a Fresnel lens that is discussed in Chapter 3. The principle behind this lens type is that the lens thickness can be reduced by integer multiples of a wavelength, so that the first cycle in the pulse from one Fresnel ring will have the same time of flight as the  $n^{\text{th}}$  cycle from the  $n^{\text{th}}$  Fresnel ring. This reduces the overall lens thickness, but at the cost of requiring more cycles for the focal pressure to ramp up to its maximum.

Annular array transducers focus by dividing the transducer into a series of elements, with each element independently pulsed with an electrical signal. The array elements are typically designed to have equal area, so that the electrical load is the same for each element. This also conveniently causes the elements to become progressively narrower toward the perimeter of the array, allowing the elements to send acoustic energy at wider angles. For an  $N$ -element array with outer radius ( $r$ ), the radius for the  $n^{\text{th}}$  element can be calculated using Equation 2.20. The time of flight between each element and the focus are calculated, and the electrical pulses are delayed by the difference in time of flight so that the pulse from each element arrives at the focus at the same time. Equation 2.21 is used to calculate the delays for each element relative to the outer element ( $r_N$ ).

$$r_n = \sqrt{\frac{nr^2}{N}} \quad (2.20)$$

$$t_n = \frac{\sqrt{r_N^2 + y_f^2} - \sqrt{r_n^2 + y_f^2}}{c_w} \quad (2.21)$$

One concept that is critical to transducer design is the case of an acoustic wave travelling from one medium to another through a thin layer. A diagram of this is shown in Figure 2.9. The intensity transmission coefficient for this special case can be derived, as given in Equation 2.22. This equation calculates the acoustic intensity that is transmitted into medium 3, based on the acoustic impedances ( $Z_1, Z_2, Z_3$ ), the layer thickness ( $\ell$ ), and the wavelength in medium 2 ( $\lambda_2$ ). The details of how this is derived, and the fundamentals of transmission and reflections coefficients will not be discussed here, but readers who require more background on this topic should review Foundations of Biomedical Engineering by Cobbold [93].

Graphs of the transmission coefficient versus normalized thickness for two different sets of acoustic impedances are shown in Figure 2.10. The graph on the left shows the case representing a matching layer between an aluminum lens (or piezoceramic composite) and water. The ideal acoustic impedance was selected ( $\sqrt{Z_1 Z_3}$ ), which results in a maximum value of  $T_I$  close to 1 for a thickness of  $\lambda_2/4$ . This is referred to as a quarter wavelength matching layer. Although the optimal for this case is 5 MRayls, Parylene-C ( $Z = 2.7$  MRayls [97]) is often used because a precise thickness can be conformally coated on curved surfaces using vacuum deposition. The graph on the right is for a piezocomposite transmitting through a low impedance material (i.e. epoxy, or plastic) into piezoceramic. This is representative of the backing design used for the dual-frequency transducer in Study 3. In this case a  $\lambda_2/4$  layer gives a minimum in the transmission coefficient, meaning that only about 5% of the acoustic intensity is transmitted into the backing. This is referred to as a destructive backing layer.

$$T_I = \frac{4Z_3Z_1}{(Z_1 + Z_3)^2(\cos(2\pi\ell/\lambda_2))^2 + (Z_2 + Z_1Z_3/Z_2)^2(\sin(2\pi\ell/\lambda_2))^2} \quad (2.22)$$

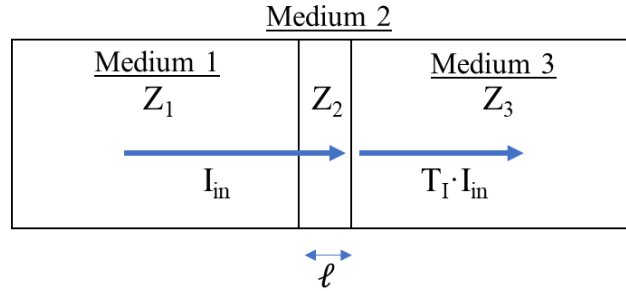


Figure 2.9: Diagram showing the transmission of an acoustic wave from one acoustic medium, through a thin layer of a second medium and into a third medium. The transmission coefficient,  $T$ , is the ratio of acoustic intensity that is transmitted into the third medium.

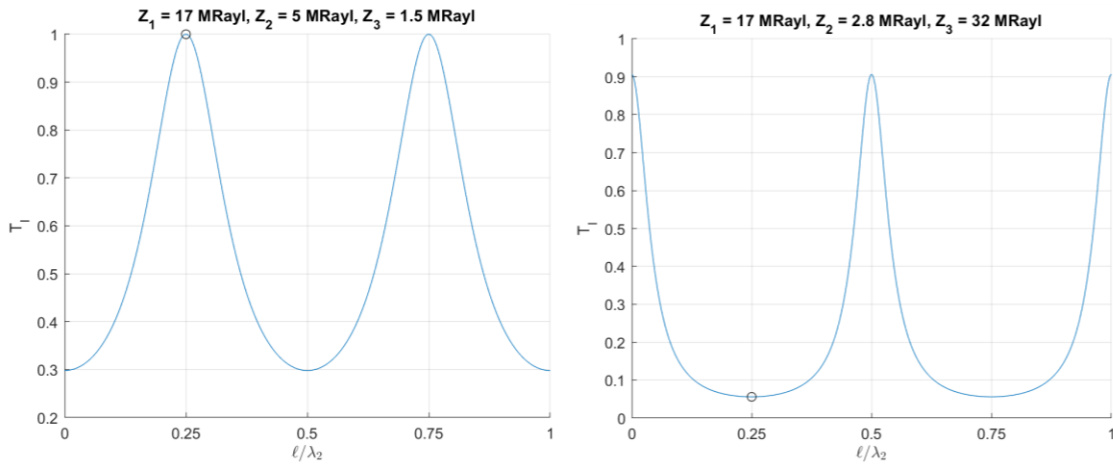


Figure 2.10: Graphs of the transmission coefficient as a function of the layer thickness normalized by wavelength, for two different sets of acoustic impedances.

## 2.5 TRANSDUCER MODELS

The transducer modelling methods used throughout this thesis are discussed in this section, including Krimholtz, Leedom, and Matthaei (KLM) [98], finite-element method (FEM), and HITU simulator [99]. These are used to design and better understand the histotripsy devices, and the experimental data are compared to the results from these simulations.

Figure 2.11 shows an overview of the transducer modelling methodology that was used. The equivalent parameters for the piezoceramic composite are used in the COMSOL transducer model, which is used to simulate the output pressure (linear focal pressure and beamwidths). The transducer surface pressure from the FEM model is input into a non-linear acoustic simulation code, called HITU simulator v2, to calculate the focal pressure with non-linear acoustic effects included.

Alternatively, starting from the measured electrical impedance of a piezocomposite, a KLM model can be fit to the data, and used to estimate the equivalent piezoelectric parameters. This methodology was used in Chapter 4. A KLM approach has also been used to model axisymmetric lens-focussed transducers, by dividing the transducer into a series of 1D rings, which are pulsed in parallel. This provides a quick estimate of the transducer impedance and acoustic output, but is less accurate than the FEM approach, so the latter was used throughout this work.



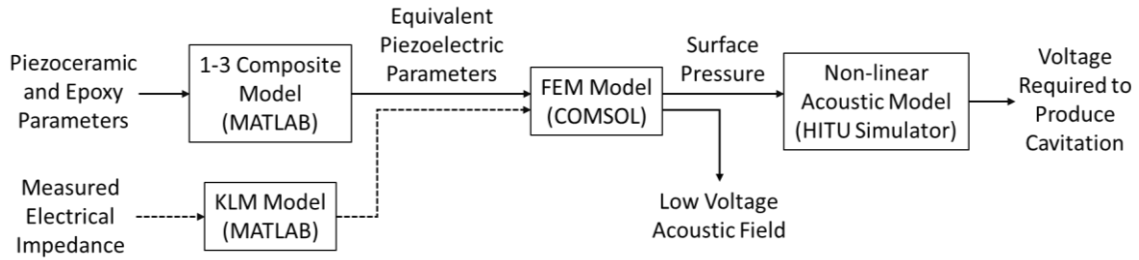


Figure 2.11: Block diagram of the transducer modelling methodology used in Chapters 3, 4, and 5.

### 2.5.1 FEM MODEL

There are many commercially available finite element software packages. For the work presented here, COMSOL Multiphysics was used because of its ability to model the acoustic output of a piezoelectric transducer in a simple and intuitive way. It has built-in electrostatics, solid mechanics, and pressure acoustics physics interfaces, which can be coupled together to model the acoustic pressure field from an applied electrical voltage. For simplicity, axial symmetry was used to significantly reduce the number of degrees of freedom required by the solver. As the focussed transducers simulated are axially symmetric (or close to it) around the central axis, modelling them this way produced results that agreed very well with measurements.

The 10 mm diameter aluminum lens-focussed transducer published by Woodacre et al. [100] was used to initially set up a transducer model in COMSOL, with the results compared to the measured data to validate the model accuracy. The methodology used to create and validate this model with the published results will be discussed here. All FEM models used in the three studies are set up in a similar way.

The model geometry is defined using the built-in user interface, including the piezoelectric composite, aluminum lens, Parylene-C matching layer, and water. The water domain is surrounded by a perfectly matched layer (PML) to simulate free-field conditions. Next, a set of material properties is input for each domain in the model. The model geometry is shown in Figure 2.12, with annotations showing each of the materials. The axis of symmetry runs along the  $r = 0$  line (vertical line along left edge of model geometry).

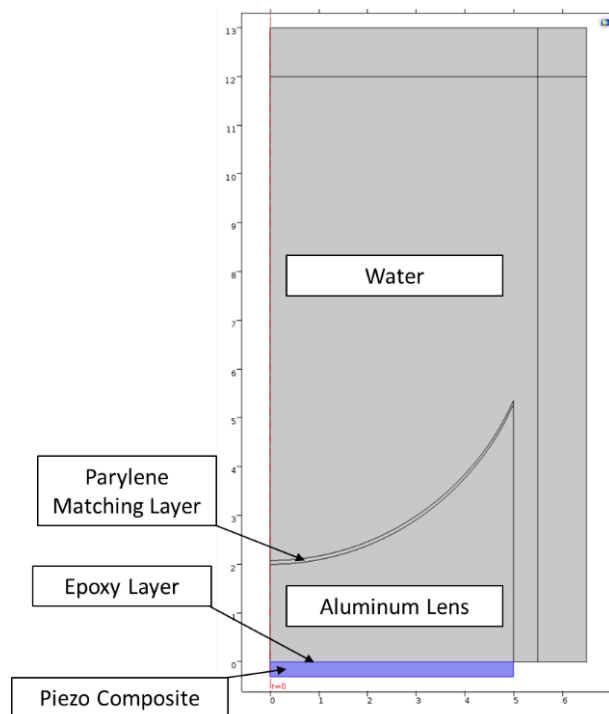


Figure 2.12: FEM model geometry for a lens-focussed transducer.

Next, the physics interfaces are assigned to the model domains. The electrostatics physics is applied to the piezo composite, the solid mechanics physics is applied to the piezo composite, lens and matching layer, and the pressure acoustics physics is applied to the water. The model couples the electrostatics to solid mechanics in the composite to

model the piezoelectric effect, and the vibrations at the boundary between the matching layer and water are converted into an acoustic pressure wave input in the water.

The lens and matching layer are modelled as linear elastic materials, using the density, Young's modulus, and Poisson's ratio. The piezo composite was modelled as an equivalent homogeneous piezoelectric material using the equations described in the previous section. Table 2.1 shows an example of the parameters calculated for a 45% volume fraction composite, calculated from the parameters for PZT-5A and Spurr epoxy [96], using Equations 2.5 through 2.9.

Table 2.1: Material properties of PZT-5A ceramic, Spurr epoxy, and 45% volume fraction composite.

<b>PZT-5A</b>				<b>Spurr Epoxy</b>	
$c_{11}^E$	120 GPa	$e_{31}$	-5.351 C/m <sup>2</sup>	$c_{11}$	5.3 GPa
$c_{12}^E$	75.2 GPa	$e_{33}$	15.783 C/m <sup>2</sup>	$c_{12}$	3.1 GPa
$c_{13}^E$	75.1 GPa	$\epsilon_{33}^S$	$900\epsilon_0$		
$c_{33}^E$	111 GPa				

<b>45% Volume Fraction Composite</b>			
$\bar{c}_{13}^E$	10.61 GPa	$\bar{e}_{31}$	-0.389 C/m <sup>2</sup>
$\bar{c}_{33}^E$	36.52 GPa	$\bar{e}_{33}$	8.71 C/m <sup>2</sup>
		$\bar{\epsilon}_{33}^S$	$405\epsilon_0$

Within the solid mechanics interface, a thin elastic layer was defined between the composite and the lens to model the epoxy bond line. Instead of modelling an actual material layer, which would require a dense mesh for accurate results, the layer is

approximated as a normal and tangential spring constant per unit area along the interface between two meshed domains. The spring constants are calculated from the Young's modulus ( $E$ ), shear modulus ( $G$ ), Poisson's ratio ( $\nu$ ), and layer thickness ( $t$ ), using Equations 2.23 and 2.24.

$$k_n = \frac{E(1 - \nu)}{t_{epoxy}(1 + \nu)(1 - 2\nu)} \quad (2.23)$$

$$k_t = \frac{G}{t_{epoxy}}, \quad \text{where } G = \frac{E}{2(1 + \nu)} \quad (2.24)$$

A free triangular mesh was applied to the piezocomposite, lens, matching layer, and water domains, with the maximum element size set so that there was a minimum of ten points per wavelength in each material. A convergence test was performed to confirm that this was more than sufficient for good model accuracy. The meshed model geometry is shown in Figure 2.13.

The composite model was initially validated by calculating the electrical impedance of the composite alone and comparing it to the measured in-air impedance of an equivalent size sample, and an isotropic loss factor in the composite was added to fit the curve to measured data. The composite damping coefficient was then added in the full model. The thickness of the epoxy layer was varied to fit the impedance curves for the published transducer [100], then a loss factor was added to damp the spurious modes. Figure 2.14 shows a comparison between the model and the measured impedance data.

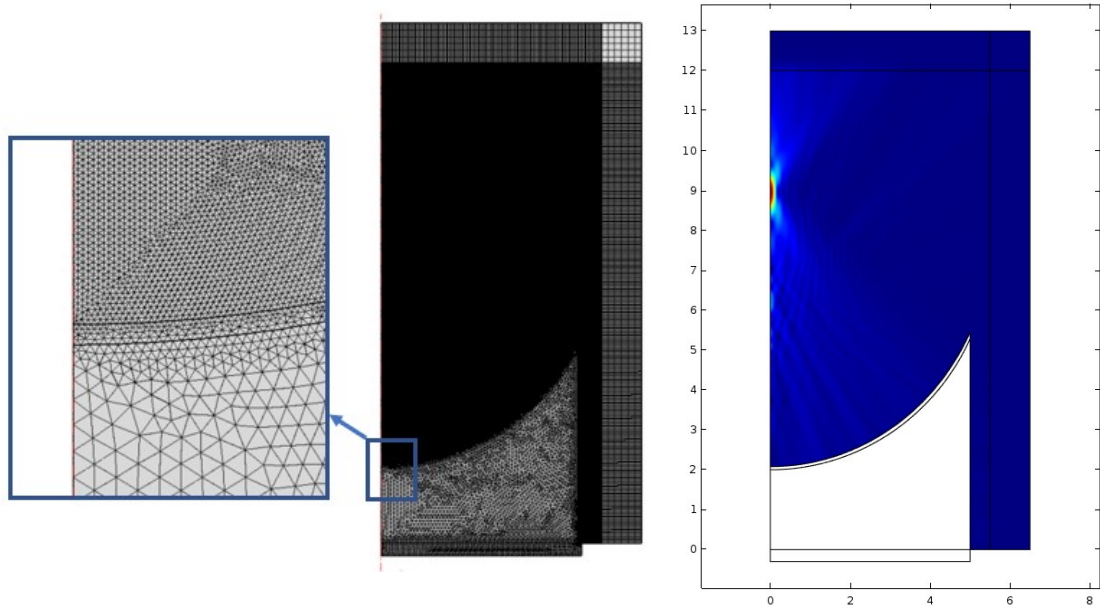


Figure 2.13: FEM model geometry after meshing (center), detailed view of the triangular mesh in the lens, matching layer, and water domains (left). Simulated pressure field (right), low pressure amplitude is shown as blue, high pressure is red.

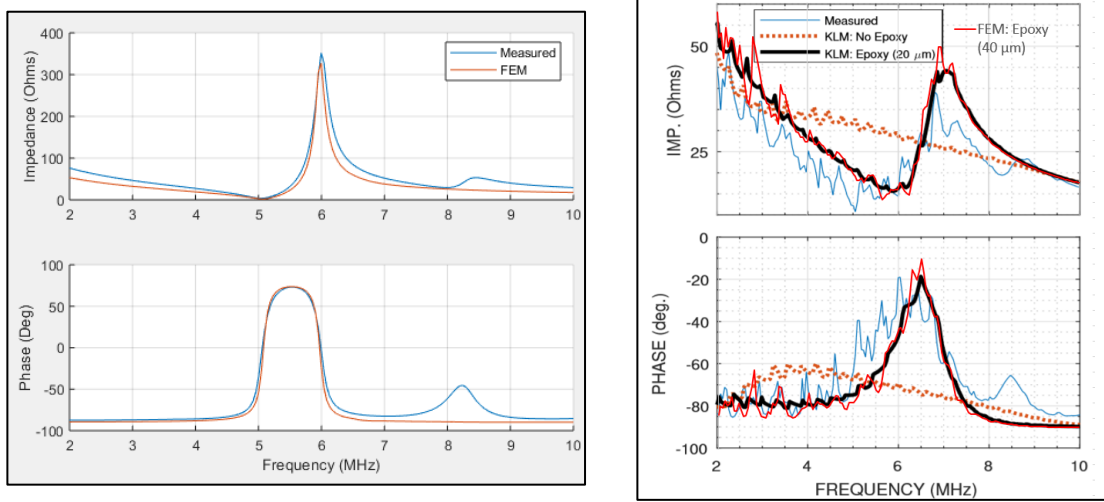


Figure 2.14: Comparison of the electrical impedance from the FEM model and measurements, for a composite in air (left), and a finished transducer (right) (reprinted from [100], ©2018 IEEE).

Finally, the simulated acoustic pressure field was compared to the measured acoustic data. The measured pressure per volt from the publication was 0.29 MPa/V at 6.8 MHz [100]. The result from the model was almost exactly the same at that frequency: 0.30 MPa/V. Figure 2.15 shows a comparison of the shape of the focused acoustic beam, with the axial and radial beamwidths annotated, showing good agreement.

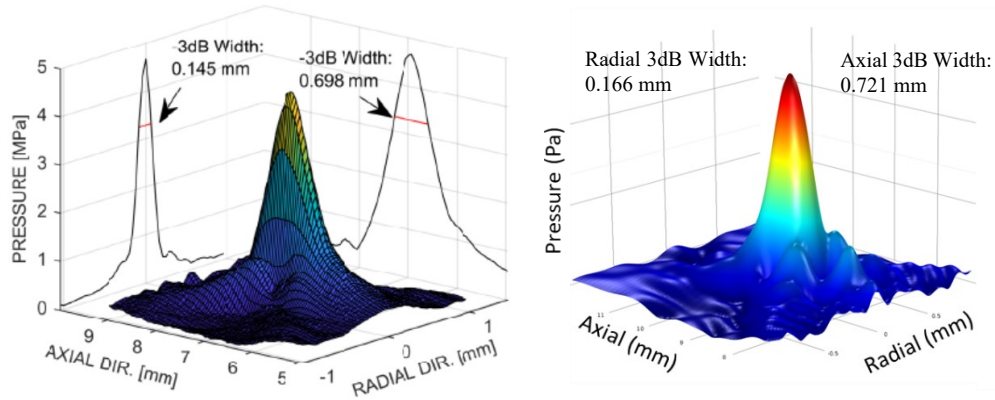


Figure 2.15: Comparison of the measured (left) (reprinted from [100], ©2018 IEEE), and simulated (right) acoustic radiation patterns.

### 2.5.2 KLM MODEL

The KLM model is a simple 1D frequency domain model for thickness mode transducers. Figure 2.16 shows a diagram of an active piezoelectric layer and the equivalent circuit diagram, with the equations for calculating the circuit components from the input parameters. The electrical part of the circuit is represented by a fixed value capacitor ( $C_0$ ), a frequency-dependant capacitor ( $C'$ ), and a frequency-dependant transformer with turns ratio  $\phi$ , that converts from the electrical domain (voltage/current) to the mechanical domain (force/velocity). Acoustic wave propagation in the mechanical domain is

represented as an electrical transmission line. The acoustic signal is interpreted as originating from a plane through the center of the disk's thickness and propagating along sections of transmission lines in both directions, where the output terminals give the force and velocity on the front and back face of the piezo disk. Additional passive acoustic layers, such as matching or backing layers, can be added as sections of transmission lines.

The transfer function of the circuit model is calculated using 2-port network theory. Each circuit component is represented as a 2x2 transmission matrix, and the overall transfer function is calculated using matrix multiplication, as shown in Equation 2.25 for a simple piezoelectric disk in air. The matrix form for series components ( $C_0$ ,  $C'$ ), parallel (shunt) components, transformers, and transmission lines are shown in Equation 2.26, 2.27, 2.28, and 2.29, respectively. The impedance  $Z$  refers to the electrical impedance for components before the transformer, and the mechanical impedance (area multiplied by acoustic impedance) for those after the transformer. In the equation for a transmission line,  $\ell$  is the layer thickness, and  $\gamma = \alpha + j\beta$ , where  $\alpha$  is the attenuation coefficient and  $\beta = 2\pi/\lambda$ . The transfer function matrix is calculated for the frequencies of interest, and the input electrical impedance curve is calculated using  $Z_a = A_{11}^{tr}/A_{21}^{tr}$ , and the force on the front face of the transducer is  $F_2 = V/A_{11}^{tr}$ , where  $V$  is the input signal vector in the frequency domain.

To model a lens-focussed transducer, the KLM modelling approach presented in Woodacre et al. [100] was used. The transducer is approximated as a set of discrete rings, each with a uniform lens thickness. The rings are modelled using 1D KLM models, which are combined in parallel to model the full transducer.

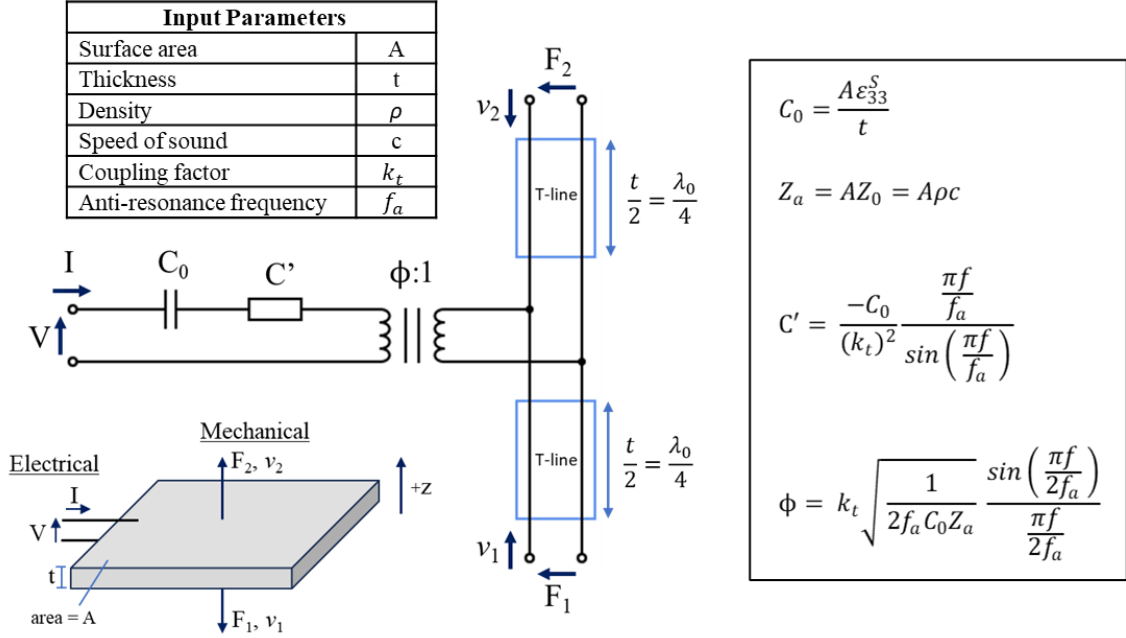


Figure 2.16: The KLM model for a thickness mode transducer. The equivalent circuit relate the electrical domain to mechanical (acoustic) domain. The equations on the right are used to calculate the circuit component values based on the input parameters.

$$[A^{tr}] = [A^{C_0}][A^{C'}][A^\phi][A^b][A^T][A^L] \quad (2.25)$$

$$[A^S] = \begin{bmatrix} 1 & Z_S \\ 0 & 1 \end{bmatrix} \quad (2.26)$$

$$[A^P] = \begin{bmatrix} 1 & 0 \\ 1/Z_P & 1 \end{bmatrix} \quad (2.27)$$

$$[A^\phi] = \begin{bmatrix} \phi & 0 \\ 0 & 1/\phi \end{bmatrix} \quad (2.28)$$

$$[A^T] = \begin{bmatrix} \cosh(\gamma_T \ell_T) & Z_a \sinh(\gamma_T \ell_T) \\ \sinh(\gamma_T \ell_T)/Z_a & \cosh(\gamma_T \ell_T) \end{bmatrix} \quad (2.29)$$



### 2.5.3 HITU SIMULATOR

Non-linear acoustic simulations were performed using HITU Simulator v2.0, which is an open source MATLAB package developed by Joshua Soneson at the FDA [99]. It uses the wide-angle Khokhlov-Zabolotkaya-Kuznetsov (WAKZK) equation in the frequency domain to model continuous wave high intensity focussed ultrasound beams. The spatial pressure distribution is calculated at each harmonic, accounting for non-linear frequency-dependent effects, and from this the temporal average intensity is calculated. Figure 2.17 shows an example of the axial peak maximum and minimum pressure distribution from a 10 mm diameter transducer with a 7 mm focal length, for progressively higher source pressure to show the increased non-linearity.

For a particular transducer diameter and focal length, the peak non-linear focal pressures can be plotted as a function of linearly extrapolated focal pressure as shown in Figure 2.18. This is useful for predicting the transducer pulse voltage that is required to produce cavitation. Starting with a cavitation threshold pressure of -27.4 MPa in water [24], the corresponding linear focal pressure is 45.9 MPa. From this the expected cavitation voltage can be calculated by dividing the linear focal pressure by the low voltage transmit sensitivity (focal pressure per volt applied to the transducer, in MPa/V). In this example, the predicted cavitation voltage is  $45.9/0.30 = 153$  V.

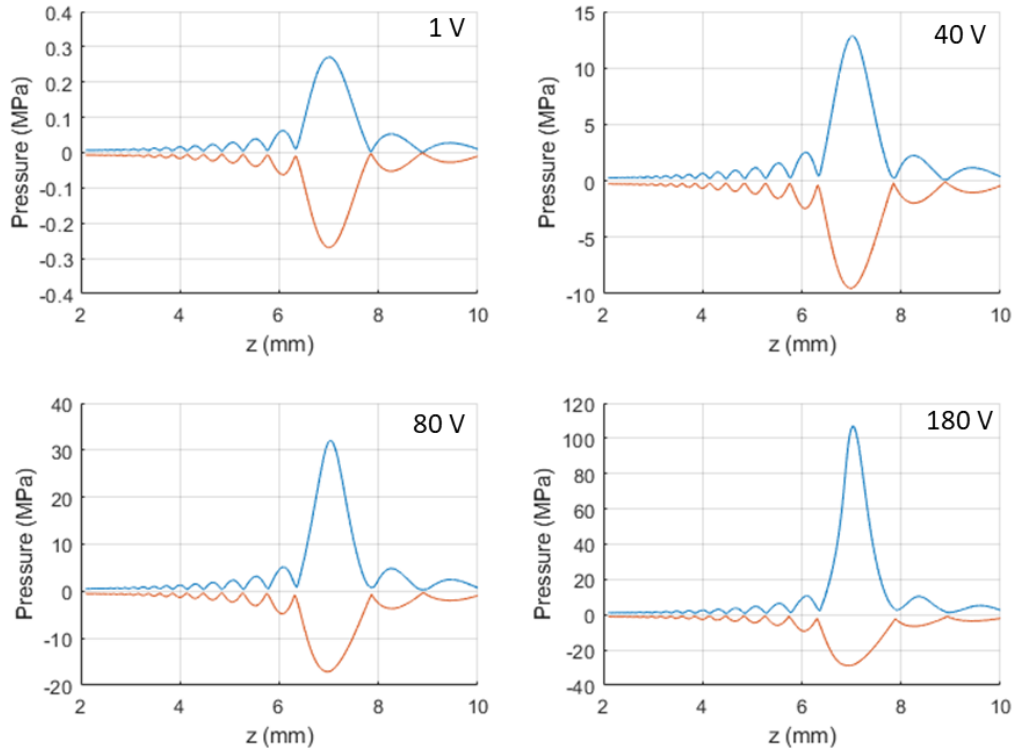


Figure 2.17: Axial pressure distribution from a 10 mm diameter transducer with 7 mm focal length for various voltage pulse amplitudes. Note the peak positive (blue) and negative pressures (orange) become increasingly asymmetric with increasing voltage.

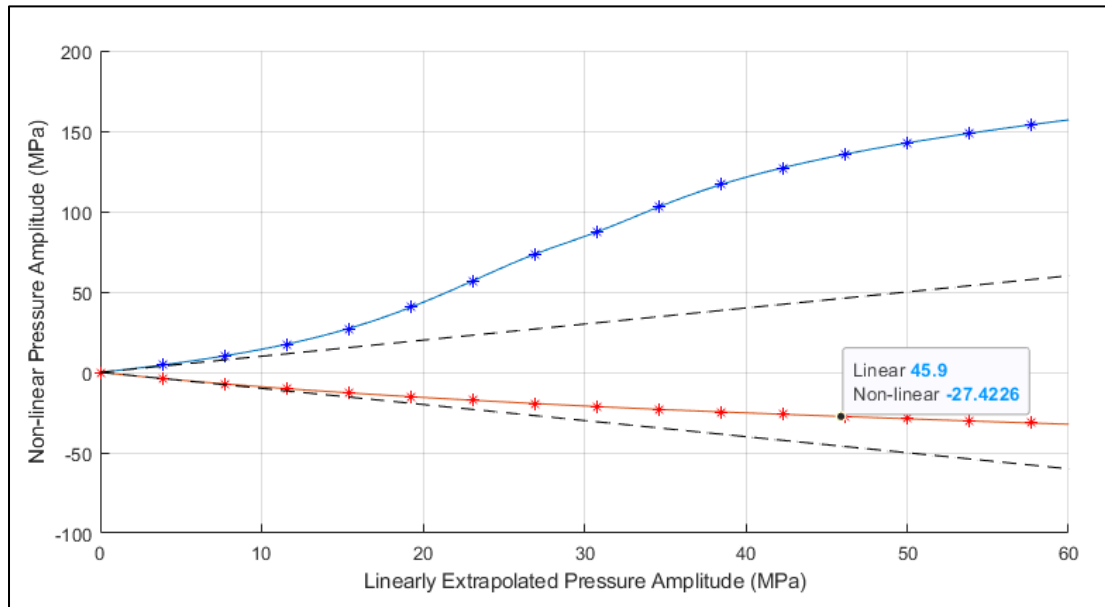


Figure 2.18: Non-linear peak positive and negative focal pressure amplitude versus linear pressure amplitude. The highlighted point corresponds to the intrinsic cavitation threshold in water.

## **CHAPTER 3:**

# **A DUAL FREQUENCY LENS-FOCUSED ENDOSCOPIC HISTOTRIPSY TRANSDUCER**

### **3.1 PREAMBLE**

Much of the content in this chapter has previously been published in IEEE Transactions on Ultrasonics, Ferroelectric, and Frequency Control [101]. Some redundant introduction content from Chapter 1 has been omitted from the original manuscript and some has been kept retaining the original flow of the published work. Methods, results, and discussion have been expanded upon from the original paper as deemed appropriate.

© 2021 IEEE. Reprinted, with permission, from M. G. Mallay, J. K. Woodacre, T. G. Landry, N. A. Campbell and J. A. Brown, "A Dual-Frequency Lens-Focused Endoscopic Histotripsy Transducer," in IEEE Transactions on Ultrasonics, Ferroelectrics, and Frequency Control, vol. 68, no. 9, pp. 2906-2916, Sept. 2021, doi: 10.1109/TUFFC.2021.3078326.

In reference to IEEE copyrighted material, which is used with permission in this thesis, the IEEE does not endorse any of Dalhousie University's products or services. Internal or personal use of this material is permitted. If interested in reprinting/republishing IEEE copyrighted material for advertising or promotional purposes or for creating new collective works for resale or redistribution, please go to

[http://www.ieee.org/publications\\_standards/publications/rights/rights\\_link.html](http://www.ieee.org/publications_standards/publications/rights/rights_link.html) to learn how to obtain a License from RightsLink. If applicable, University Microfilms and/or ProQuest Library, or the Archives of Canada may supply single copies of the dissertation.

### 3.2 INTRODUCTION

Histotripsy is a therapeutic ultrasound technique for non-invasively ablating tissue. A focused transducer is used to cause tissue fractionation by applying short, high amplitude ultrasound bursts which induce cavitation. The collapse of these bubbles mechanically destroys the tissue [102]. Typically, an extracorporeal transducer (50 – 145 mm diameter) is used to generate the histotripsy pulses through soft tissue, at a focal depth of 70 – 150 mm [17], [21], [22], [23]. This has been investigated in pre-clinical studies for several indications, especially liver cancer [24], [25], [26], [27], [28]. Schuster et al [29] conducted an in-human trial to assess the clinical safety of histotripsy for the treatment of symptomatic benign prostatic enlargement using an extracorporeal 700 kHz, 36 element transducer with an 11 cm focal distance, observed with transrectal ultrasound imaging. Applying histotripsy to neurosurgery is appreciably more challenging due to the presence of the skull, which strongly attenuates the signal and produces aberrations at the focus, reducing accuracy.

Minimally invasive keyhole surgery is a very common approach to resecting brain tumors that are relatively close to the surface of the brain. In this technique, a 15 – 20 mm hole [3] is made in the skull through which a cavitron ultrasonic surgical aspirator (CUSA) or similar device is used to ablate the tumor tissue through mechanical vibration of the tip. Even with deeper tumor locations in which a larger craniotomy is used, a small endoscopic

surgical aspirator is used to create a pathway to the tumor from the surface of the brain. Other than using optical microscopes and endoscopes, which can only visualize the surface of tissue, these procedures are typically performed with limited intra-surgical real-time image guidance. Preoperative imaging such as CT, MRI and MRA [103], however, is typically used to plan and navigate the surgery but these can be unreliable due to brain shift that occurs during the craniotomy and surgical resection itself [45]. Ultrasound has also recently been useful in comparing preoperative and intraoperative anatomic data, and can be used to update navigation based on intraoperatively collected ultrasound images [104].

In a very promising recent study, Sukovich et. al. [105] demonstrated in vivo histotripsy on a porcine brain, producing lesions with sharp boundaries and without causing excess hemorrhage. In this study a 5 cm craniectomy was used to provide an acoustic window for the relatively large histotripsy transducer. Transcranial histotripsy has also been shown [106], using a 30 cm aperture, 500 kHz, 256-element ultrasound array to ablate a tissue phantom through a human skull cap. The lesions generated in this study were mostly well contained but showed small extraneous lesions, on the order of 0.2 mm diameter, well outside of the focal region. This suggests that endoscopic aspirators may still be necessary for resecting primary tumors with fine margins, while avoiding highly sensitive healthy tissue.

We hypothesize that an endoscopic histotripsy transducer could potentially replace surgical aspirators such as the CUSA because of the inherent advantages. First, a histotripsy-based aspirator has higher precision than conventional low-frequency contact ablation devices such as the CUSA. Second, since a histotripsy transducer will only erode tissue at the focal location, there is more opportunity to avoid sensitive tissues by ablating

across structures such as nerves or vessels. Lastly, a histotripsy endoscope has the potential of integrating endoscopic ultrasound imaging into the same device for real-time image guidance.

Previously, our group has developed a near-endoscope sized prototype of such a device that comprised of a 10 mm diameter transducer with a 4 mm square hole in the center for a co-registered imaging endoscope [100]. Although these results were promising, the device was still too large for common neurosurgical applications. The authors could not find any other publications on histotripsy transducers approaching an endoscopic form factor. A 15 mm aperture laser-generated focused ultrasound (LGFU) device has been used to cut and ablate tissue with high precision ( $\sim 50$   $\mu\text{m}$  resolution) [107]. While trans-rectal or laparoscopic high intensity focused ultrasound (HIFU) probes have been developed, most are still too large for minimally invasive keyhole surgery or to fit down a surgical pathway created by a surgical aspirator [108]. Additionally, HIFU destroys tissue through cell hyperthermia resulting in more peripheral damage to healthy tissue than with histotripsy [82]. Kim et al. recently developed a small aperture ( $< 3$  mm) for intracavitary tissue ablation [109].

In this work, we present an endoscopic histotripsy transducer with an active region of 5 mm by 5 mm and outer package dimensions of 6 mm by 6 mm that is capable of free-field intrinsic cavitation. The active element is a planar piezoelectric element, and a strong focus is generated with an acoustic lens. Four acoustic lens concepts were prototyped and characterized. Additionally, a method of increasing the peak pressure by adding a pump transducer behind the therapy transducer was developed. This concept is similar to dual-beam histotripsy [110], with the key difference being that the two frequencies originate

from the same active surface. A similar single aperture dual-frequency approach has been studied for HIFU [111]. However, in this case the approach was taken to increase heat generation, not to boost the focal pressure. Finally, this device was used to produce lesions in an ex vivo rat brain, to assess its ability to ablate tissue. This was monitored in real time using a high frequency ultrasound imaging endoscope that was co-registered with the histotripsy endoscope. The following sections describe in detail the design and fabrication of the prototype endoscopic histotripsy transducer.

### 3.3 METHODS

#### 3.3.1 DESIGN SUMMARY

Figure 3.1 depicts the overall concept of the transducer and highlights all of the layers within the stack. The furthest layer towards the back of the probe is a low frequency actuator that we would describe as a low frequency “pump” transducer operating at 1.2 MHz. The pump transducer contributes to the peak negative pressure but remains well below any cavitation threshold. Therefore, its primary function is to lower the peak pressure requirements for the primary therapeutic transducer operating at 5 MHz given that the two wavefronts coherently sum together. Between these two transducers a coupling layer is bonded that acts both to efficiently couple the pump transducer’s acoustic energy through to the front face of the probe, and also to maximize the acoustic energy from the therapeutic transducer to the front face. On the front face of the therapy transducer, which would otherwise be in contact with tissue, a low F-number acoustic lens is bonded in order to provide focal gain and therefore increased pressure within the focal region. Different acoustic lens concepts were simulated, and experimentally evaluated.

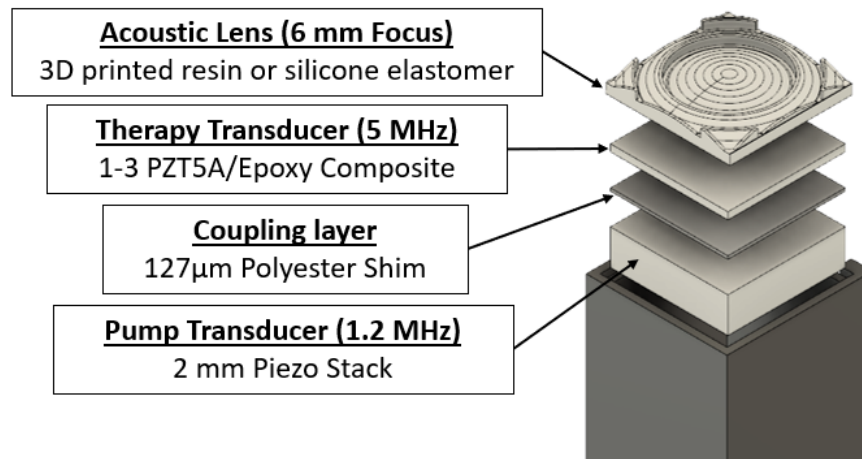


Figure 3.1: Diagram of dual frequency stack with silicone Fresnel lens.

### 3.3.2 FEM MODELLING

A 2D axi-symmetric Finite Element Method (FEM) model of the transducer was developed using COMSOL Multiphysics. While the square transducer design does not have axial symmetry, it was modelled as a cylindrical transducer with an equivalent active area. This was found to match well with electrical impedance and pressure measurements. The therapeutic transducer, which was designed to be a 1-3 piezoelectric composite, was modelled using the equations in [96] based on the volume fraction, the properties of PZT-5A, and the properties of the epoxy. The Poisson's ratio and loss factor of the epoxy were chosen to fit the impedance of a piece of unloaded composite measured in air.

The lens materials were modelled using density and Young's modulus values from the technical data sheet for each material, while Poisson's ratio was adjusted to fit the measured speed of sound for each. The loss factor for the lens materials was initially set to 4% and was later modified to fit measurements for the individual materials. The properties used in the FEM model are given in Table 3.1.



Table 3.1: Material properties used in the FEM model.

	Resin	Silicone	PZT5A Composite
<b>Speed of Sound (m/s)</b>	2624	1017	3650
<b>Density (kg/m<sup>3</sup>)</b>	1090	1030	3790
<b>Young's Modulus (Pa)</b>	2.80E+09	2.46E+06	-
<b>Poisson's Ratio</b>	0.4247	0.499616	-
<b>Loss Factor</b>	5.5%	5.3%	2.5%
<b>Volume Fraction</b>	-	-	40%
<b>Clamped Dielectric</b>	-	-	424
<b>Effective Coupling Factor</b>	-	-	0.573

The model was set up using the electrostatics interface coupled to the solid mechanics interface to simulate the piezoelectric effect in the PZT-5A composite. The lens was modelled as a linear elastic material, coupled to water using an acoustic-structure boundary. The acoustic signal in the water was simulated using the pressure acoustics interface, which solves the Helmholtz equation in the frequency domain. The water was surrounded by a perfectly matched layer to absorb the pressure wave to simulate a transducer in free field conditions. The maximum element size of the mesh was set to ensure at least 6 elements per wavelength at the maximum frequency used in the model (10 MHz).

### 3.3.3 ACOUSTIC LENSES

Four acoustic lens designs were assessed, consisting of conventional and Fresnel lens variants using two different materials: resin, and silicone. These materials were selected in part for their relatively large difference in speed of sound compared to tissue, while having an acoustic impedance close enough to tissue to not require a matching layer. Additionally,

the resin was selected due to being readily available, while the silicone had the benefit of biocompatibility.

As the resin lenses had a higher speed of sound than tissue, these consisted of a concave geometry, while the silicone lenses with a lower speed of sound had a convex geometry. An elliptical lens curvature was calculated for each using an equation based on Fermat's principle of least time. Each lens was designed for a focal depth of 6 mm (f-number of approximately 1). A 5 MHz PZT-5A 1-3 composite transducer was built for each of these lens designs.

The first lens material was a methacrylate photopolymer (Form 2 Clear Resin), which was 3D printed using a Form 2 SLA printer (Formlabs Inc., Somerville, MA, USA). A test piece was printed to measure the acoustic properties of the cured resin. The density was  $1163 \text{ kg/m}^3$ , and the longitudinal speed of sound was 2624 m/s. The plano-concave lenses were printed directly on the Form 2 build platform with a layer resolution of 25  $\mu\text{m}$ . The minimum lens thickness was 0.5 mm, with a peak pressure depth 3.5 mm from the outermost part of the lens face.

The second lens material was a silicone elastomer (MED-6015). This has a density of  $1030 \text{ kg/m}^3$ , and a measured speed of sound of 1017 m/s. A plano-convex lens was cast onto the piezo composite using a 3D printed mold. A thin layer of copper was sputtered over the mold to prevent the 3D printed resin outgassing from interacting with the silicone while curing. PTFE dry film lubricant was applied to the mold to ensure the lens released from the mold. The lens thickness at the center of the convex lens was 1.4 mm, resulting in peak pressure location of 4.6 mm from the lens surface. Convex shape lends itself better

to in vivo application, as it doesn't trap air bubbles. In practical applications, concave lenses would likely have to be filled with a low loss material with properties similar to water.

A Fresnel lens version of these lenses was also designed using each material. This increases the depth of the peak pressure from the transducer face and decreases attenuation due to the thinner lens profile. The procedure for designing the lens is outlined in Sato *et al.* [112]. The equation for the lens is broken up into several segments, with the lens thickness reset to zero each time it reaches a given value. The focal length of each segment is adjusted to account for this shift. To achieve phase continuity across the lens, the shift must be a common integer multiple of the wavelength both in water and in the lens. For silicone this is a  $3\lambda$  shift ( $2\lambda$  in water), or about 0.6 mm at 5 MHz. The resin Fresnel lens was designed in a similar manner using a  $2\lambda$  shift in water, which is close to one wavelength in the resin. A photograph of all four lens designs bonded to the front of therapeutic transducers is shown in Figure 3.2.

#### 3.3.4 PUMP TRANSDUCER

In the dual frequency design, shown in the concept diagram in Figure 3.1, a pump transducer is situated at the back of the 5 MHz (therapy) transducer to boost the overall pressure at the focus. This is done without affecting the device cross section (6 mm by 6 mm including case). A quarter wavelength destructive backing layer between the two transducers mimics the therapy transducer being air-backed. It reflects most of the acoustic wave sent by the therapy transducer into the backing so it's in phase with the next cycle in

the burst. The general case of an acoustic filter between two transducers with a large frequency difference has been studied by Ma *et al.* [113].

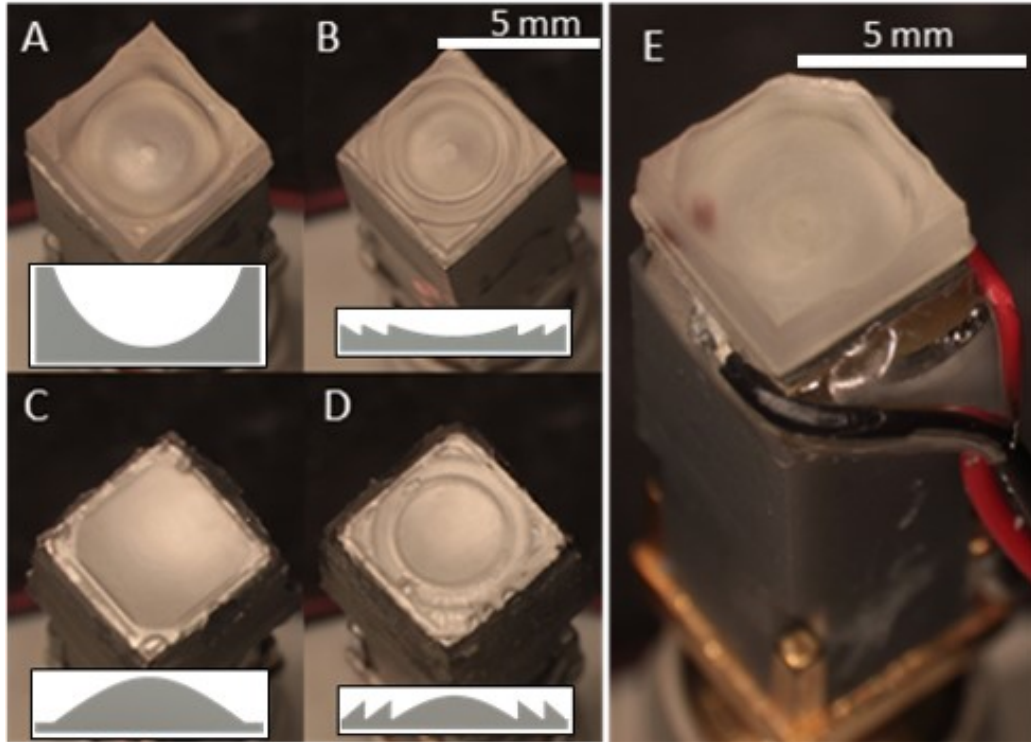


Figure 3.2: Images of the four lens designs: resin conventional lens (A), resin Fresnel lens (B), silicone conventional lens (C), silicone Fresnel lens (D), and the dual frequency transducer (E). A through D include a section view through the center of each lens (corner to corner).

The PZT-5A composite and polyester layers in front of the pump transducer form a mass-spring resonance [114]. To verify this effect, a model was used to run a parametric sweep of the pump transducer operating frequency from 100 kHz to 5 MHz. The average surface displacement on the therapy transducer front face was calculated for an imposed displacement along the inner surface of the coupling layer. The maximum occurred for a frequency of 0.9 MHz. The pump transducer selected for this study was a PA4FE piezoelectric stack (Thorlabs Inc. Newton, NJ, United States), which has a thickness resonance frequency of 310 kHz, with the intention of operating it at the third harmonic,

near this mass-spring resonance frequency. A full acoustic FEM model including this 2 mm thick pump transducer was used to select the frequency that produced the highest pressure at the lens focus, which was 1.2 MHz.

While lower frequency transducers, such as Langevin transducers, can generate much higher output pressures, the maximum pressure occurs at the radiating surface due to the lower frequency (i.e. 15 – 120 kHz). Using a pump transducer in that frequency range would result in undesirably high pressures away from the treatment area. Using a higher frequency pump transducer would provide better focal gain, but at the cost of increased attenuation.

### 3.3.5 TRANSDUCER FABRICATION

In order to quantify the performance of each lens, therapeutic transducers were initially fabricated without a pump transducer. To fabricate these, a 6 mm by 6 mm by 15 mm (XYZ) case was 3D printed. It was designed for an SMA connector to fit in the back and had a hole in the front for mounting the 5 MHz PZT-5A 1-3 dice and fill composite (Smart Materials Corp., Florida, USA). A 40% volume fraction was used due to availability. While a higher volume fraction would boost the therapy pressure per volt, it would also change the optimal pump transducer frequency. The 5.2 mm square composite was epoxied to the 0.2 mm wide inner ledge of the case. A low force spring loaded pin was used to make the electrical connection to the back of the composite. After curing overnight, a wire was soldered between the spring pin and the signal pin of the SMA connector, and the case was sealed using UV cured epoxy. A 2  $\mu\text{m}$  layer of copper followed by a 0.5  $\mu\text{m}$

layer of tin was sputtered over the transducer, creating a reliable electrical connection from the front face of the composite to the SMA connector ground pins.

Following lens performance measurements, a full stack (Figure 3.1) was fabricated with a pump transducer and a resin lens. A 127  $\mu\text{m}$  thick polyester sheet (Artus Corp. Englewood, NJ, United States) was used as a coupling layer, with the color layer removed to ensure a strong bond to the piezo layers. It was fabricated in a similar way to the transducers built in for the lens experiments using the same 5 MHz PZT-5A composite therapy transducer. The composite was diced slightly larger than the pump transducer to leave exposed electrode for soldering. The pump transducer had the electrodes on the sides allowing the entire front face to be bonded directly to the coupling layer, which was then bonded to the therapy transducer.

A second dual frequency device was built, using PMN-PT 1-3 composite with similar volume fraction for the therapy transducer. This was expected to perform better due to having a higher piezoelectric coefficient ( $d_{33}$ ) and electromechanical coupling factor ( $k_t$ ) than PZT-5A [115]. While PMN-PT is often not considered suitable for high electric field applications, in this design it was driven using a unipolar pulse, effectively adding a dc bias to prevent depolarization, and produce linear strains [116].

### 3.3.6 EX VIVO ABLATION EXPERIMENT

The PZT-5A dual frequency resin lens transducer was tested on an ex vivo rat brain to characterize its ability to ablate tissue. The PMN-PT composite transducer failed mechanically due to the stress from the piezo contacting the spring-loaded pin used for the electrical connection. This occurred before reaching the cavitation threshold in water, so it

was unavailable for the ablation experiment. The use of animal tissue was approved by the Dalhousie University Committee on Laboratory Animals (Protocol 20-005). A 64-element, 30 MHz imaging endoscope similar to that described in [117] was used to visualize the experiment in real time. This was driven by a custom-built FPGA based hardware beamformer [118] using focused line-by-line imaging. Images were generated using delay and sum beamforming, with 4 focal zones and 128 lines between +/- 32 degree viewing angle and an axial range of 2 to 10 mm. The beamformer was modified to output a 1 kHz square wave to trigger the histotripsy pulser. This was synchronized as an event that occurred between capturing imaging lines to avoid capturing noise streaks from the histotripsy pulser.

The histotripsy transducer and imaging probe were held in place using independently adjustable fixtures, at an angle of approximately 45 degrees between the forward-looking axes, as shown in Figure 3.10. The histotripsy transducer was positioned to place the focus close to the center of the imaging window. This was verified by generating a bubble cloud in water and adjusting the imaging slice to find the center of the cloud. The rat brain was placed in a dish filled with distilled water; the dish was raised to position it under the probes. The pulser was set to a 360 V amplitude, 8 cycle burst with a 1 kHz pulse repetition frequency (PRF).

## 3.4 RESULTS

### 3.4.1 LENS RESULTS

Four therapy only transducers were fabricated to test the performance of each lens concept. The electrical impedance of each of these transducers was measured and is given in Figure 3.3. The minimum impedance was approximately  $29 \Omega$  for the resin lens transducers, and approximately  $15 \Omega$  for the silicone lens transducers. For each, the resonance frequency was located between 4.8 - 4.9 MHz. The phase angle on resonance was approximately  $-22$  degrees for the resin lens transducers and approximately  $-40$  degrees for the silicone lens transducers. The focal gain for the resin lenses were 10.4 and 8.6 for the conventional and Fresnel variants respectively, while it was 11.1 for both silicone lenses.

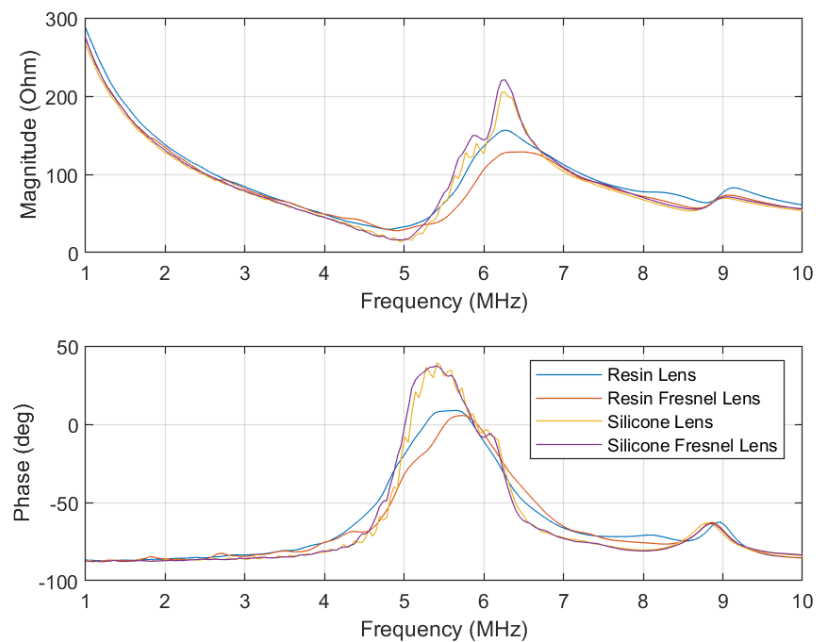


Figure 3.3: Measured electrical impedance magnitude and phase from each of the four transducers used to characterize the lens designs.



Pressure measurements were conducted using an HGL0085 capsule hydrophone with an AG-2010 preamplifier (ONDA Corp., Sunnyvale, CA, USA), which has an 85  $\mu\text{m}$  diameter element size, and a sensitivity at 5 MHz of 36 mV/MPa. The transducers were driven by a pulser similar to the design by Brown and Lockwood [119], with a unipolar 10 cycle burst with a pulse repetition frequency (PRF) of 500 Hz. The number of cycles was selected to ensure the pressure waveform reached steady state. The peak negative pressure was measured for each of the four transducers at nine peak-peak voltage levels between 2 and 6 V. A linear trendline was used to estimate the transmit sensitivity (focal pressure per volt) of each. The air-backed resin lens transducers both had a one-way fractional (-3dB) bandwidth of around 22% (1.10 MHz), while the silicone lens transducers both had a bandwidth of 15% (0.75 MHz). Whether the lens was a Fresnel design or not had no significant impact on the bandwidth of the transducer.

A 3-axis servo-controlled positioning stage was used to measure radiation patterns for each transducer. Measured acoustic radiation patterns for each silicone lens variant is shown in Figure 3.4, along with simulated radiation patterns from the associated COMSOL models. The radiation pattern of the resin conventional lens is shown in the upper row of Figure 3.6. The focal length of the lens was calculated by using the voltage pulse and hydrophone signal to estimate the time of flight. The axial and radial -3 dB beam width was estimated for each based on the radiation pattern. The results from the hydrophone measurements are given in Table 3.2.

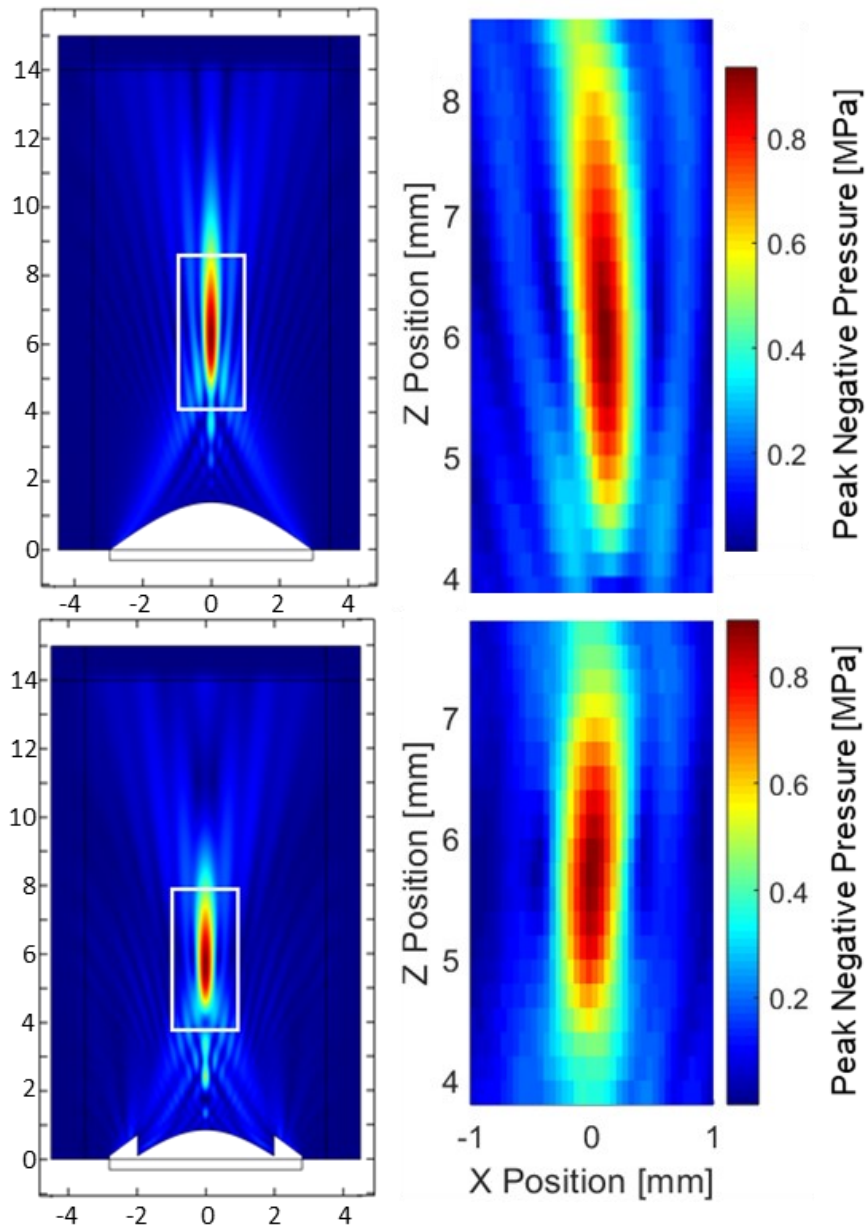


Figure 3.4: Simulated radiation pattern from the FEM model (left column) compared to a measured radiation pattern (right column) for the silicone conventional (top row) and Fresnel (bottom row) lens transducer. The transducer model geometry is shown at the bottom of FEM model plots. The white rectangles show the area covered by the measured radiation pattern.

Table 3.2: Comparison of FEM and measured results for each lens

		Radial Beamwidth (mm)	Axial Beamwidth (mm)	Focal Depth (mm)	Peak Negative Pressure (MPa/V)	Extrinsic Cavitation Voltage (V)
Resin Conventional	Model	0.33	1.61	5.6	0.150	-
	Measured	0.31	1.30	6.1	0.150	123
Resin Fresnel	Model	0.35	2.40	5.7	0.128	-
	Measured	0.33	2.28	6.1	0.124	166
Silicone Conventional	Model	0.32	2.84	6.2	0.160	-
	Measured	0.31	2.71	6.1	0.160	168
Silicone Fresnel	Model	0.34	2.36	5.7	0.172	-
	Measured	0.34	2.11	5.8	0.160	200

To further characterize the lenses without damaging the hydrophone, a simple 5 MHz, 5mm aperture air-backed PMN-PT plate transducer was connected to an oscilloscope and used to measure the peak pressure at the focus for higher drive levels since the calibrated polymer hydrophone cannot be used at higher drive levels. This was used to simply provide relative pressure measurements, which were then scaled based on the low voltage measurements from the hydrophone. The drive voltage was increased until cavitation due to surface reflections from the plate superimposing with the incoming signal was observed (referred to in this paper as extrinsic cavitation). This was easily detected when the measured signal changed from a clean signal to an erratic, jittery signal, as well as the audible bubble cloud noise emitted from the water tank. The voltage at which each transducer exhibited extrinsic cavitation is given in Table 3.2.

The mean intrinsic cavitation threshold in water, measured in [24] was -27.2 MPa at 1.5 MHz and -27.4 MPa at 3 MHz. Based on the minimal increase with frequency, a similar threshold is expected at 5 MHz. The air-backed PMN-PT plate was included in an FEM model. The pressure near the surface of the plate was found to increase by approximately

90% for both the therapy and pump transducers. Based on this increase in pressure, cavitation is expected at 14.4 MPa measured pressure. Both conventional lens transducers cavitated at a pressure extrapolated to 15 MPa, while the Fresnel lens transducers extrapolated to approximately 18 MPa before cavitating.

### 3.4.2 DUAL FREQUENCY TRANSDUCER RESULTS

The electrical impedance curves for the therapy layers in the dual transducer were measured and are shown in Figure 3.5. The impedance at resonance for the therapy transducer had minimal change compared to the air backed composite, while the anti-resonance frequency was more damped.

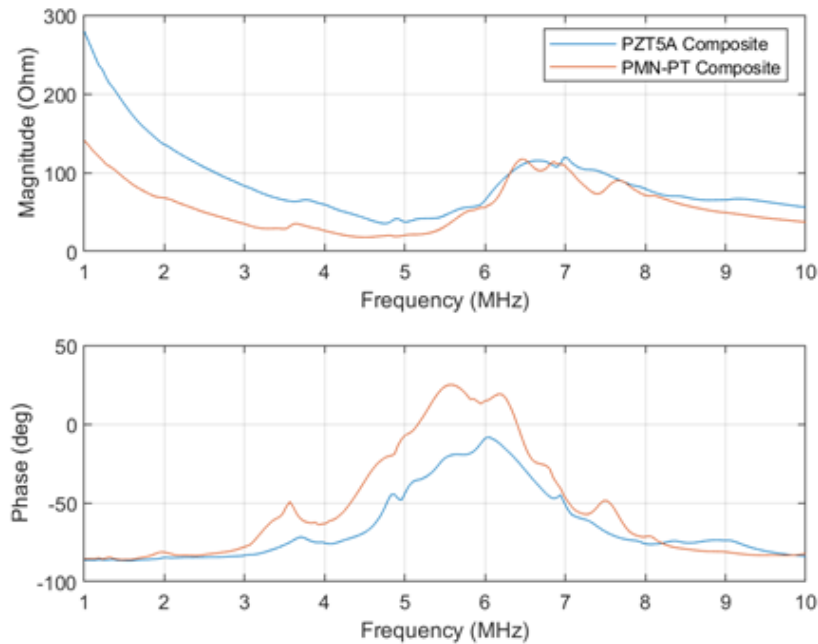


Figure 3.5: Measured electrical impedance magnitude and phase from the therapy transducer portion of the dual-frequency devices.

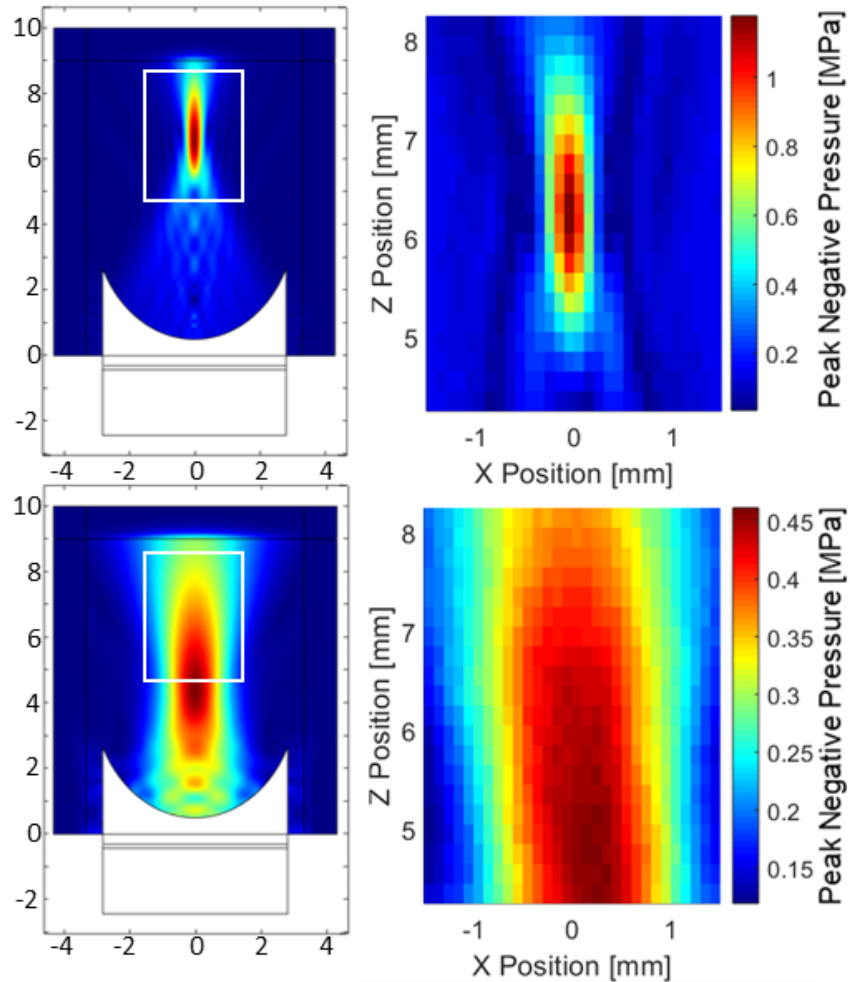


Figure 3.6: Simulated radiation pattern from the FEM model (left column) compared to a measured radiation pattern (right column) for the dual frequency transducer. The upper row is from the 5 MHz PZT-5A composite therapy transducer (3.6V pulse), while the lower row is from the 1.2 MHz pump transducer (36 V pulse).

The dual frequency transducer was positioned in front of the hydrophone and the pump transducer was experimentally found to have a maximum peak pressure of 0.028 MPa/V for a 1.2 MHz, 3 cycle pulse. Radiation patterns of the pump and therapy transducers were measured and are compared to the simulated results from the FEM model in Figure 3.6. With the hydrophone positioned at the focus of the dual frequency device, a delay was added to the 5 MHz therapy pulse to superimpose its peak negative pressure with the peak

negative pressure from the pump transducer. The required delay was found to be 448 ns for a 5 MHz, 10 cycle therapy pulse and 1.2 MHz, 3 cycle pump pulse. An example of the measured pressure waveforms is shown in Figure 3.7, for a different number of cycles (and delay).

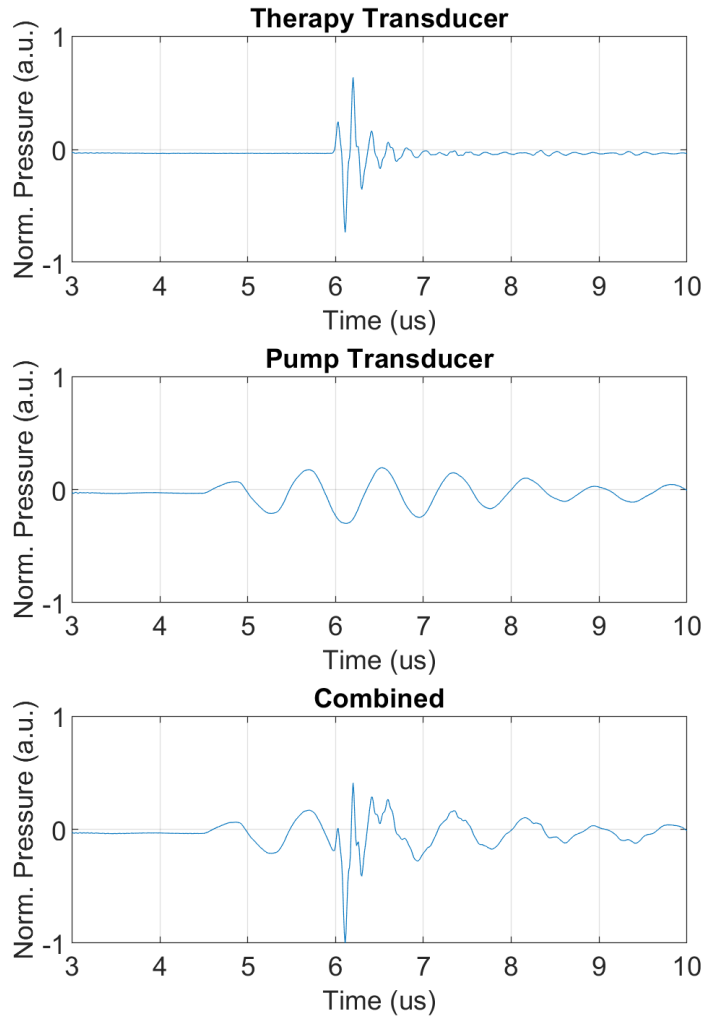


Figure 3.7: Measured pressure waveforms from the PZT-5A composite therapy transducer driven with a 5.2 MHz, 5 V, single cycle pulse (top), pump transducer driven with 1.2 MHz, 5 V, 3 cycle pulse (middle), and the two transducers pulsed together (bottom). The therapy pulse is delayed by 1.7  $\mu$ s to align the peak negative pressures from the two transducers.

The axial beamwidth for the therapy transducer was increased by 0.45 mm, and the bandwidth increased to 35% (1.73 MHz) in the dual design. The pump transducer linearly added to the overall pressure output at the focus even for therapy pulses driven at 130 V (at this voltage the therapy transducer acoustic response had become non-linear).

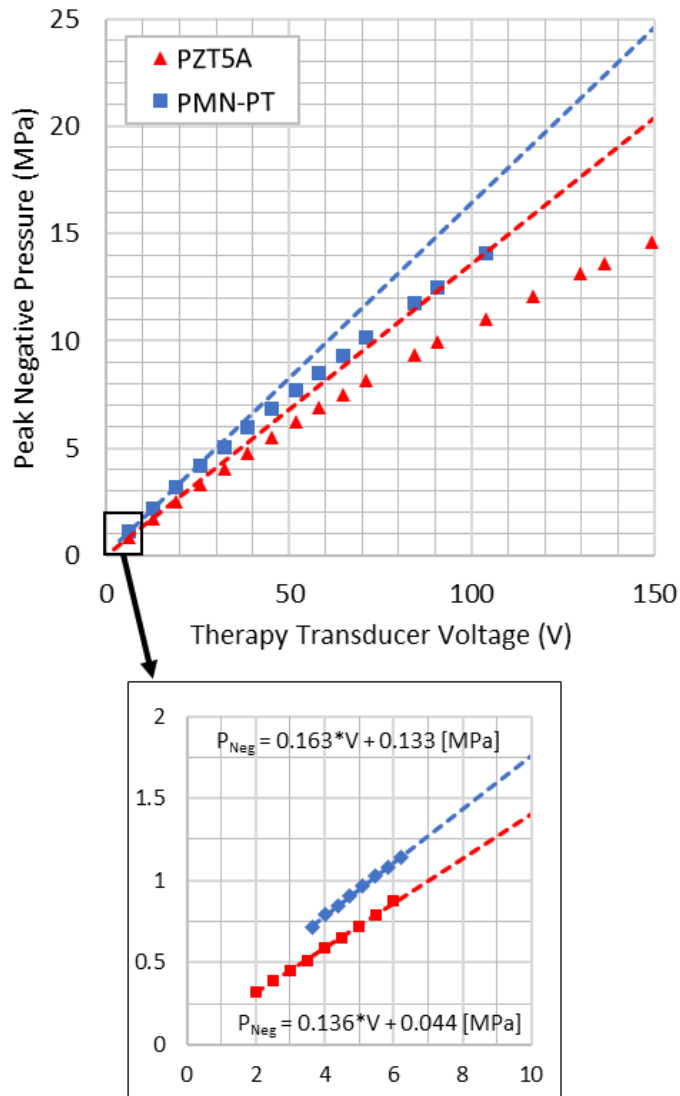


Figure 3.8: Peak negative pressure versus pulse voltage for the therapy transducer in the dual frequency devices. The lower graph shows the low voltage hydrophone measurements and linearized pressure per volt. The upper graph shows measurements from the PMN-PT plate, scaled based on the hydrophone results, with the dashed line showing the extrapolated pressure per volt.

The transmit sensitivities of the therapy transducer portion of the dual-frequency devices were measured. The lower graph in Figure 3.8 shows the hydrophone measurement from the two devices for low amplitude pulses. Again, the PMN-PT plate was used to take pressure measurements at higher drive levels, the result of this is shown in the upper graph of Figure 3.8, with trendlines showing the linearly extrapolated transmit sensitivity using hydrophone measurements. As expected, the PMN-PT composite produced a higher transmit sensitivity while being more linear than the PZT-5A composite transducer. Extrinsic cavitation occurred on the PMN-PT plate surface for pulse voltages of 116 V for the PMN-PT composite and 149 V for the PZT-5A composite. Just before cavitation began, the measured pressure for both was just over 14 MPa.

The extrinsic cavitation threshold test was repeated for various pump transducer voltages, to characterize its contribution to the focal pressure. The pump transducer was pulsed continuously with a fixed amplitude, and the therapy transducer voltage was slowly increased until there was cavitation detected. This was done five times for each pump voltage. Figure 3.9 shows the mean from this test, with the error bars showing the standard deviation. A linear trendline is shown for both curves.

The slope of this curve represents the ratio of the pump transducer transmit sensitivity divided by the therapy pressure per volt. From previous hydrophone measurements, the pump transducer produced 0.028 MPa/V in the PZT-5A based device, and 0.02 MPa/V in the PMN-PT based device.



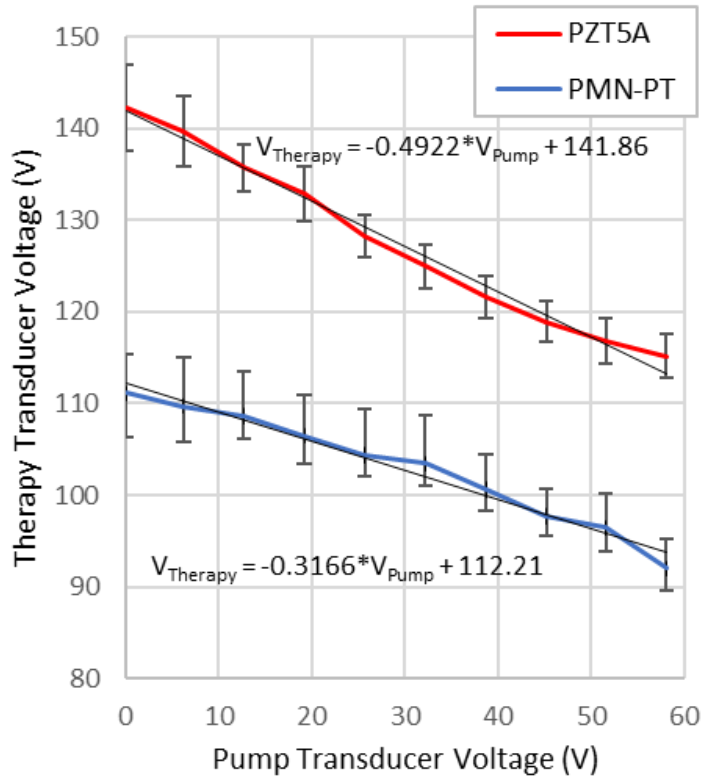


Figure 3.9: Results from the extrinsic cavitation threshold experiment for both dual frequency devices, showing the therapy transducer drive voltage required to extrinsically cavitate on the surface of the PMN-PT plate for several pump transducer drive voltages. The mean from 5 trials is shown by the line graph, with the error bars showing the standard deviation.

The slopes in Figure 3.9, were both about 2.5 times higher than expected from the low voltage measurements, meaning the contribution from the pump transducer was much greater than indicated from the initial hydrophone measurements. This can be partly explained by the decrease in therapy transmit sensitivity for the higher pulse voltages.

The therapy pulse voltage was increased to generate a free-field cavitation bubble cloud in water. For the PZT-5A device, no intrinsic cavitation occurred for voltages up to 400 V using a 4.9 MHz, 10 cycle burst with 500 Hz PRF. The PRF was increased to 1 kHz, and the number of cycles reduced to 8 cycles. With these settings the transducer was able

to intrinsically cavitate in water at 360 V. The linearly extrapolated peak negative pressure at this voltage is -49 MPa. However, the actual pressure is expected to be closer to the cavitation threshold (~27 MPa) in water, due to the non-linear behavior. With the pump transducer pulsed with a 60 V, 1.2 MHz, 3 cycle burst at the same PRF, the therapy voltage pulse could be reduced by around 20 V and still cavitate. This result was similar to the extrinsic cavitation test where the required therapy voltage was reduced by 27 V for the same change in pump voltage.

### 3.4.3 EX VIVO ABLATION EXPERIMENT

The transducer was able to ablate tissue both at the water-brain interface, and with the transducer focused under the surface. The ablation of a single spot was demonstrated in the cerebellum approximately 3 mm under the surface. This produced an ablation region that was approximately 500  $\mu\text{m}$  in diameter (characteristically anechoic in the B-mode image). This can be seen in Figure 3.11, with the arrows indicating the direction of the histotripsy transducer.

Next, the histotripsy transducer was focused to the surface of the cortex. A cavitation bubble cloud formed and immediately started ablating tissue, and was moved to cut a hole into the brain. The imaging probe was used to scan through the hole showing the cylindrical shape. The hole was about 0.75 – 1 mm in diameter and 2 mm deep. The hole is visible in Figure 3.10, in the inset image of the brain after testing.

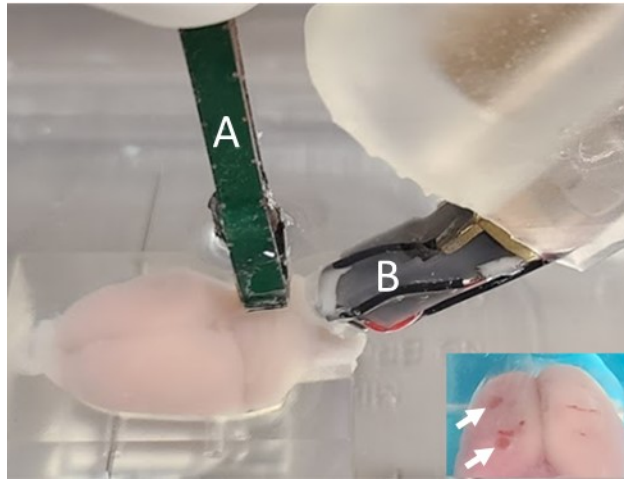


Figure 3.10: A picture of the rat brain ablation experiment. The co-registered imaging (A) and dual frequency histotripsy (B) endoscopes are positioned over the rat brain. The inset picture in the lower right corner shows two small holes (indicated by arrows) created by the histotripsy transducer.

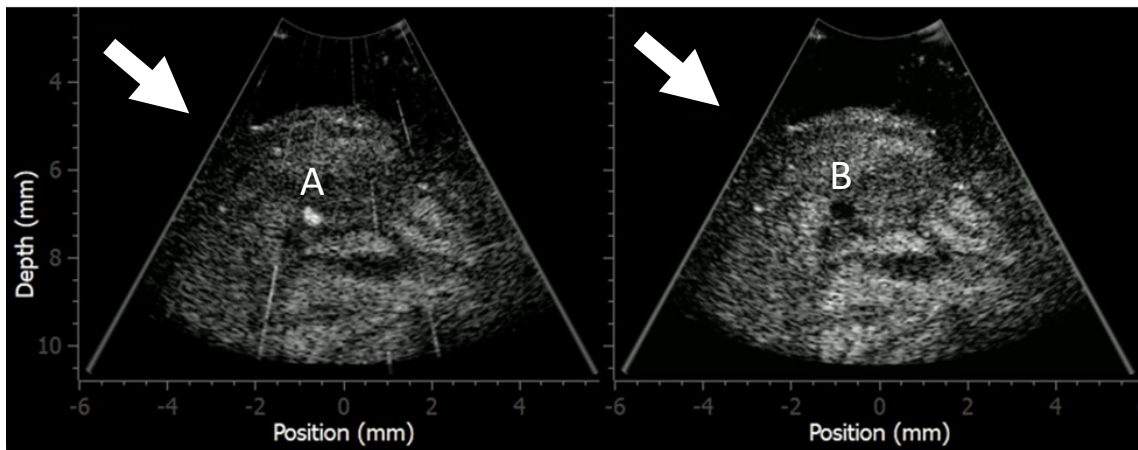


Figure 3.11: Ultrasound images from the rat brain ablation experiment, with arrows indicating the forward-looking axis of the histotripsy transducer. The left image shows the bubble cloud (A) forming a small lesion in the cerebellum, and the image on the right shows the lesion (B) following a few seconds of histotripsy treatment.

In another test, cavitation was initiated at 2 mm under the surface in the cortex and sustained for several seconds producing an approximately 500  $\mu\text{m}$  diameter ablated region. The sample was moved to widen the hole to closer to 1 mm in diameter. The sample was then raised toward the histotripsy transducer to cut a 2 mm deep cylindrical hole. At this point the lens was touching the surface of the rat brain.

### 3.5 DISCUSSION

#### 3.5.1 LENS RESULTS

Despite having a slightly lower transmit sensitivity at low drive levels than the silicone lens transducers, the conventional resin lens transducer had the best cavitation performance. For this reason, along with it being the easiest to reliably fabricate, it was used in the subsequent study that incorporates the pump transducer for boosting peak pressure.

The resin Fresnel lens offers the advantage of having a thinner profile, but at the cost of a lower peak pressure output. This is largely due to concave shape, where the highest part from each ring partially occludes the ring surrounding it. The silicone used in this study is biocompatible, and the lens can easily be integrated into a thin layer encapsulating the entire endoscope. This would translate well to a clinically relevant device. It does however have a significantly more involved fabrication process. The resin has no biocompatibility certification; a device based on this would likely require a sheath or to switch to a comparable material that is biocompatible. It is also much harder than the silicone, which is less appropriate for neurosurgical applications.

The silicone Fresnel lens also has a thinner profile, but without the self-occlusion problem. This lens had a higher cavitation threshold despite having the same output pressure at low voltages as the conventional lens. This could be due to the signal from the Fresnel lens spending less time at peak pressure because it requires more cycles to reach the maximum amplitude than the conventional lens. The model predicted an 8% higher pressure output than was measured. The resolution of the 3D printing and molding process is too low to fully reproduce the fine details in the Fresnel rings. It is possible using a machined mold could improve the silicone Fresnel lens transducer performance. The conventional silicone lens is a much simpler shape that can be molded with higher accuracy, which explains why the model and measurements are in better agreement for this device.

All four of the transducers had relatively good agreement between COMSOL and experimental results, given this the authors deemed it not necessary to show all 4 radiation patterns. The measured focal depth was 0.4 – 0.5 mm greater for than expected for the resin lenses. The most significant difference was the axial beamwidth of the conventional resin lens, which was 19% less than expected. The source of this discrepancy is unclear.

Based on the pressure measurements from the PMN-PT plate, it was clear that linearly extrapolating the low voltage transmit sensitivity measurements is not accurate. This is thought to be due to a combination of acoustic non-linearity in the water, and non-linearity in the lens material at high strains [120]. The details of this are beyond the scope of this paper but might be explored in future work.

Each of these designs could be used in a combined imaging and therapy transducer configuration, where the lens is used for focusing both imaging and therapy pulses. An aluminum lens, as used in previous work, would not function as a dual-purpose lens as well, due to the higher acoustic impedance and the presence of a matching layer for the therapy signal.

### 3.5.2 DUAL FREQUENCY TRANSDUCER

In the dual frequency device, the therapy transducer lens was modified to reduce the maximum height by 0.5 mm at the cost of 5% less surface area contributing to the focal pressure. Considering this difference, adding the pump transducer reduced the transmit sensitivity by only 5% compared to the air-backed therapy only transducer. The destructive coupling layer on the back does emulate air-backing as the model suggested.

The experiment using the PMN-PT plate was quite sensitive to the positioning of the transducer being tested; the angle of incidence of the pulse on the detector significantly affected the result. Care was taken to ensure the transducer and detector were parallel, however the results are not as accurate as if this test were performed using a calibrated hydrophone that could withstand these pressures. Regardless of this, it still clearly demonstrates that the pump transducer can significantly reduce the cavitation threshold of the therapy pulse.

### 3.5.3 EX VIVO ABLATION EXPERIMENT

The ultrasound images showed that this device is capable of ablating tissue with a high level of precision. This could be clearly monitored in real time, using the imaging endoscope. The ablated spots appeared more spherical than the shape of the high-pressure

region predicted by the radiation pattern. This is likely due to the beam being blocked by the bubble cloud once initiated. The lesions produced also showed good radial symmetry, despite the transducer having a square aperture.

Based on the stiffness of brain tumors measured by *Chauvet et. al.* [121] and a study on the effect tissue stiffness has on cavitation threshold [24], a threshold in the range of 24 - 25 MPa is expected. Given that this transducer was capable of cavitating in water, it is expected to be capable of ablating tumor tissue as well.

When power Doppler was used, the rapid motion of the bubble cloud created a strong Doppler signal, showing up as a bright colored spot in the image. This is useful for differentiating the area that is actively being ablated from any bright spots in the B-mode image due to bubbles left behind from previous bursts. This is similar to other cavitation detection schemes used by other groups [122].

Pulsing the pump transducer to generate pressures on the order of 1 MPa following ablation using the 5 MHz transducer, appeared to reduce the time it took for the residual microbubbles to collapse [123]. This was merely an interesting observation and not formally quantified during testing.

The ablation rate wasn't characterized in this study, but a qualitative estimate from a recorded video clip was  $\sim 0.1 \text{ mm}^3/\text{s}$ . Based on this it would take  $\sim 278$  minutes to ablate a  $1 \text{ cm}^3$  tumor. However, the rate is expected to increase as a larger void is created, and the shock scattering effect is more pronounced. Tumors in excess of this size would require a more macroscopic tool such a CUSA. This device is better suited for precision removal of

tumor tissue where fine margins are required that are beyond the capability of existing methods.

The use of acoustic lenses for transcranial focused ultrasound has been recently introduced [124]. A device similar to the one presented in this paper could be useful for studying transcranial histotripsy on rodents. Although, generating the pressure levels required for this would be challenging with a device this size when considering the attenuation of the in-tact skull.

#### 3.5.4 FUTURE WORK

The future direction of this work will be focused on gaining more overhead on the focal pressure, to allow further miniaturization. This could be done by replacing the PZT-5A with a higher output material such as PMN-PT. Also, using a custom designed pump transducer has the potential to significantly increase the overall output pressure. The off-the-shelf device used in this study was intended for operation below resonance and was found to fail at around 100 V operation. It worked as a proof of concept but could likely be improved. Additional lens materials will be evaluated, with a focus placed on finding a material that is more linear at high strains.

If desired, this device could easily be fabricated at a 90-degree angle to enable targeting of tissue perpendicular to the burr hole. In this case the Fresnel lens design would be especially advantageous. This could reach areas not easily accessible with a conventional CUSA device.

A more rigorous characterization of the device's ability to ablate tissue will be conducted. This would involve studying the effect of changing pulser settings (peak



negative pressure, number of cycles, PRF, etc.) and physical positioning (transducer angle of incidence, focal depth, etc.).

### 3.6 CONCLUSION

Several endoscope histotripsy devices were successfully designed, fabricated, and tested. This included various lens types with associated design trade-offs. The dual frequency concept was able to reduce the cavitation threshold of the 5 MHz therapy transducer by adding a 1 MHz pump transducer without affecting the device cross section. The pump transducer had a greater impact than expected from comparing the transmit sensitivity for the two transducers measured at low voltages. This highlights the advantage of using a lower frequency pump transducer for reducing frequency dependent losses, while benefiting from the small ablation size from a higher frequency transducer. The real time imaging of lesions being produced in the tissue was a promising step toward a useful endoscopic histotripsy device for practical applications, such as minimally invasive neurosurgery.

## **CHAPTER 4:**

# **EVALUATION OF PIEZOELECTRIC CERAMICS FOR USE IN MINIATURE HISTOTRIPSY TRANSDUCERS**

### **4.1 PREAMBLE**

After the previous study, a short follow up study [125] involved adding an imaging array in front of the dual-frequency transducer to test its effect on the focal pressure of the histotripsy device. Based on those results, it was suspected that the added attenuation of the imaging array stack would limit the smallest size of a stacked histotripsy/imaging device to about 6 x 6 mm. Simulations showed that an 8 mm diameter lens-based histotripsy transducer surrounding the existing 4 mm square imaging probe produced nearly equivalent pressure but would have an inherently less complicated fabrication process. For this reason, the attention was shifted to developing an 8 mm diameter histotripsy transducer with a hole for the imaging endoscope. Even with no imaging array in front of the histotripsy transducer, with such a small amount of active area, we would still be limited to maximum pressures near the cavitation threshold and some overhead beyond this was desired. Therefore, in this study, alternative materials were evaluated by simulating, fabricating, and testing transducers to failure in order to optimize the material used for the therapeutic element. Transducers with no hole or central imaging element were constructed to allow for a greater number to be built and tested in a reasonable timeframe.

The study presented in this chapter has previously been published in the Proceedings of the 2022 IEEE International Ultrasonics Symposium (IUS) [126] and is included here in an expanded form. The KLM simulation results previously used as a comparison to measurements and for estimating the cavitation threshold voltage, were updated to FEM simulations. Any content in the introduction section that is repeated from Chapter 1 is done so to retain the original flow of the published work.

© 2022 IEEE. Reprinted, with permission, from M. Mallay et al., "Evaluation of Piezoelectric Ceramics for use in Miniature Histotripsy Transducers," 2022 IEEE International Ultrasonics Symposium (IUS), Venice, Italy, 2022, pp. 1-4, doi: 10.1109/IUS54386.2022.9957153.

In reference to IEEE copyrighted material, which is used with permission in this thesis, the IEEE does not endorse any of Dalhousie University's products or services. Internal or personal use of this material is permitted. If interested in reprinting/republishing IEEE copyrighted material for advertising or promotional purposes or for creating new collective works for resale or redistribution, please go to [http://www.ieee.org/publications\\_standards/publications/rights/rights\\_link.html](http://www.ieee.org/publications_standards/publications/rights/rights_link.html) to learn how to obtain a License from RightsLink. If applicable, University Microfilms and/or ProQuest Library, or the Archives of Canada may supply single copies of the dissertation.

## 4.2 INTRODUCTION

Glioblastoma (GBM) is an especially aggressive form of brain cancer, with an extremely poor prognosis. The mean survival time of patients with this form of cancer is only 15 months [11]. Minimally invasive neurosurgical approaches result in improved

postoperative outcomes, including decreased risk of complications, compared to full craniotomies. Endoscopic tools and preoperative planning based on brain imaging (usually MRI) allow surgeons to significantly reduce the craniotomy size, leading to less surgical exploration and brain retraction [3], [5]. Craniotomies often result in the brain shifting from the position in the preoperative scans, making them less accurate [6]. The most commonly used tools in brain surgeries are ultrasonic aspirators, such as the cavitron ultrasonic surgical aspirator (CUSA), which have relatively large ablation sizes and lack image guidance [127]. This, in combination with brain shift limits the extent of resection, which is directly related to patient outcomes (survival and quality of life) [8], [9]. For this reason, there is a need for a high precision surgical tool with built-in imaging for correcting the mismatch between the intraoperative and preoperative brain position.

Histotripsy is a non-thermal, non-ionizing, mechanical ablation technique that works through focusing ultrasound to generate cavitation bubbles at a target location [17]. Sukovich et. al. demonstrated in vivo histotripsy on a pig brain, through a 5 cm craniectomy, producing lesions with precise boundaries [105]. A 30 cm aperture, 500 kHz, 256-element ultrasound array was used to demonstrate transcranial histotripsy by ablating a 15 mm<sup>3</sup> volume in a brain tissue sample, through a human skull cap, achieving a targeting accuracy of up to 1.5 mm [128]. However, this wouldn't be compatible with the surgical procedures currently used, and would require MRI imaging to monitor the progress, which is time consuming and not typically available.

Previously, our group presented work on miniature broadband histotripsy devices fabricated by bonding an acoustically impedance matched 5 MHz piezoceramic substrate to a parabolic aluminum lens with a Parylene-C matching layer deposited over the front

[100]. Recently, we demonstrated image-guided precision ablation in an in vivo rat brain using a near endoscopic (~10 mm diameter not including outer housing) combined ultrasound array and histotripsy device based on this design [18]. This device produced complete sub-millimeter ablations, while monitoring ablation progress in real time on the ultrasound image. These results were very promising, but a smaller outer diameter is still desired due to the limited access of the surgical tools. Currently, the minimum size of this transducer design is limited by the transmit sensitivity (pressure at focus per volt) of the piezoelectric substrate as well as the maximum drive voltage before failure.

Other therapeutic ultrasound modalities such as HIFU, which require transducers capable of sustained high-power operation, typically utilize hard ceramics for their high Q-factor and low losses to prevent overheating [129]. In contrast histotripsy transducers operate at low duty-cycles (< 1%), using low time averaged power [14]. For this reason, ceramic loss isn't as critical when selecting piezoelectric materials for use in histotripsy transducers. This means that soft ceramics are preferred for this application because of their higher clamped dielectric constant and thickness mode coupling coefficient.

While other methods of increasing the output pressure have been studied, such as superimposing a lower frequency source [101], [110], piezoelectric materials with higher pressure outputs are always desirable. Devices built to date have been based on either PZT-5A/Epoxy composite or Pz39 (porous ceramic) [130]. While Pz39 was found to be more sensitive than PZT-5A composite, the transducer tested in that study failed when driven above 1 V/ $\mu\text{m}$  of thickness.

To further reduce the transducer size, we need to select an optimal piezoelectric substrate with high sensitivity and durability. In this work we have characterized 5 different piezoelectric ceramics that are good candidates for miniature histotripsy transducers. These are PZT-5A, CTS 3203HD (PZT-5H), Pz39, Pz54 (HIFU type PZT) and PMN-38 (electrostrictive).

## 4.3 METHODS

### 4.3.1 TRANSDUCER FABRICATION

Four transducers were fabricated for each of the 5 materials. 5 MHz, 45% volume fraction 1-3 composites were fabricated to achieve a good match to aluminum, except Pz39 which is already closely matched ( $Z = 18$  MRayls). The composites were manufactured using a 60  $\mu\text{m}$  dicing blade to cut 390  $\mu\text{m}$  deep kerfs, producing 120  $\mu\text{m}$  square pillars. After the pillars were cut, the samples were ultrasonically cleaned, dried with compressed air, and placed on a hot plate at 60°C for 10 mins. The kerfs were filled with West System 105/205 epoxy and taken off the heat to cure at room temperature overnight.

The samples were then lapped flat using 9  $\mu\text{m}$  Aluminum Oxide slurry, ultrasonically cleaned and dried. Then, the surface was plasma etched, and a 30 nm Chromium and 2  $\mu\text{m}$  Copper electrode were deposited. The samples were flipped and lapped to the final thickness (290 – 340  $\mu\text{m}$ ), and then electroded using the same method. With the sample still mounted to a glass slide a diamond hole saw was used to cut the composite to 8 mm diameter.

The finished composites were bonded to an 8 mm diameter machined aluminum lens with a focal length of 7 mm. Prior to bonding, the lens was sandblasted using 400 grit

silicon carbide powder and ultrasonically cleaned in acetone. The positive side of the composite was bonded to the back of the lens using West System 105/205 epoxy, this was pressed using a BJ2 spring-loaded bonding jig (Logitech, U.K.), as shown in Figure 4.1, while the epoxy cured at room temperature.

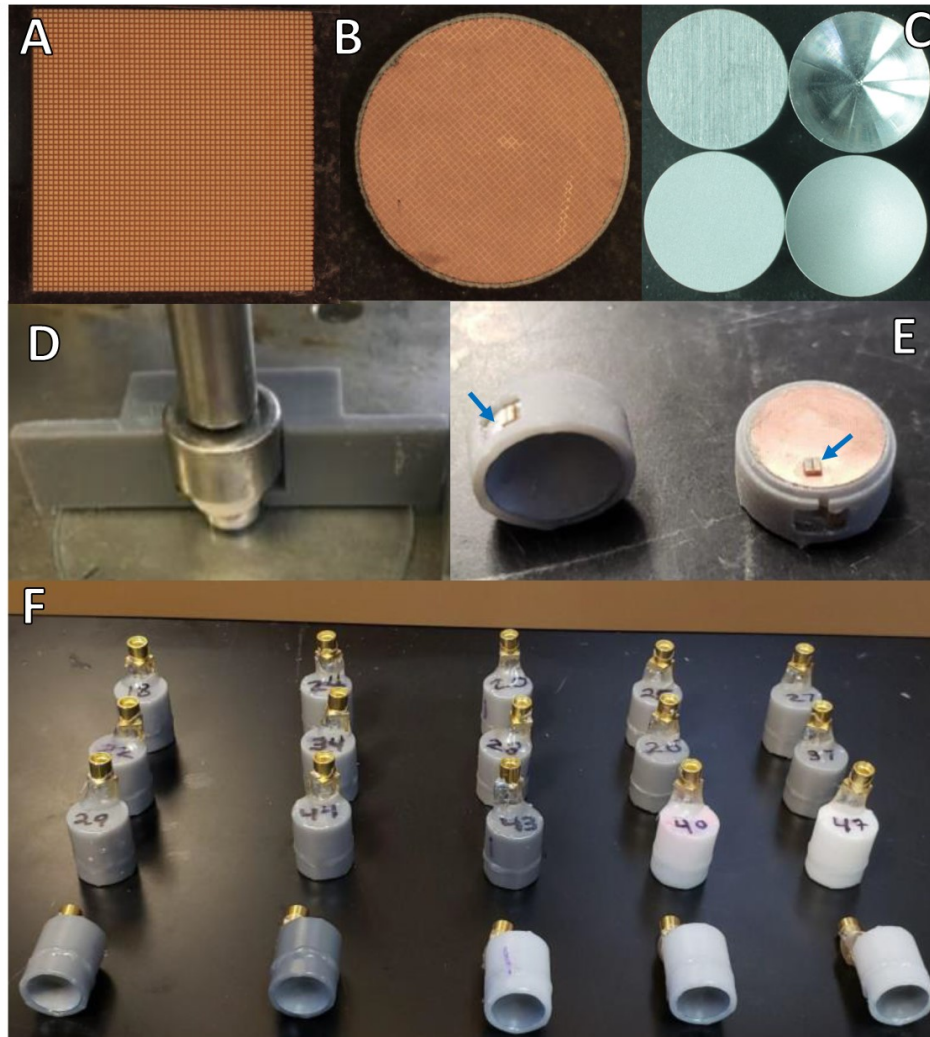


Figure 4.1: A) Piezoceramic after dicing to produce a grid of pillars. B) Finished 8 mm diameter 1-3 composite. C) Four 8 mm diameter aluminum acoustic lenses, as machined (top row) and after sand etching (bottom row). D) Composite and lens stack-up being pressed in bonding jig. E) Transducers in the case with blue arrows indicating the interposer PCBs. F) Full set of 20 finished transducers.

The transducer was placed in a 3D printed case and a small section of PCB with an exposed copper pad was glued to the back of the piezo and side of the lens. Three wirebonds were placed on each to connect the piezo negative electrode to one PCB and the side of lens to the other; the piezo positive electrode is connected through contact with the aluminum lens. The wirebonds were potted using aluminum oxide loaded epoxy, and wires were soldered to the pads to connect to an MMCX connector on the back half of the 3D printed case. The case halves were sealed using epoxy to air-back the transducers. The front face of the lens was cleaned, and a 90  $\mu\text{m}$  Parylene-C matching layer was deposited on all 20 transducers at once.

#### 4.3.2 TRANSDUCER SIMULATIONS

The electrical impedance of each composite was measured. For each sample, the effective coupling factor ( $k_t$ ), speed of sound ( $c$ ) and acoustic impedance ( $Z$ ) were calculated using the measured thickness ( $t$ ), resonance frequency ( $f_r$ ), anti-resonance frequency ( $f_a$ ), composite volume fraction ( $v$ ), and the densities of the piezoceramic ( $\rho_c$ ) and epoxy fill ( $\rho_e$ ) using Equations 4.1, 4.2, and 4.3.

$$k_t = \sqrt{\left(\frac{\pi f_r}{2f_a}\right) \tan\left[\frac{\pi(f_a - f_r)}{2f_a}\right]} \quad (4.30)$$

$$c = 2tf_a \quad (4.31)$$

$$Z = \rho c = (v\rho_c + (1 - v)\rho_e)c \quad (4.32)$$



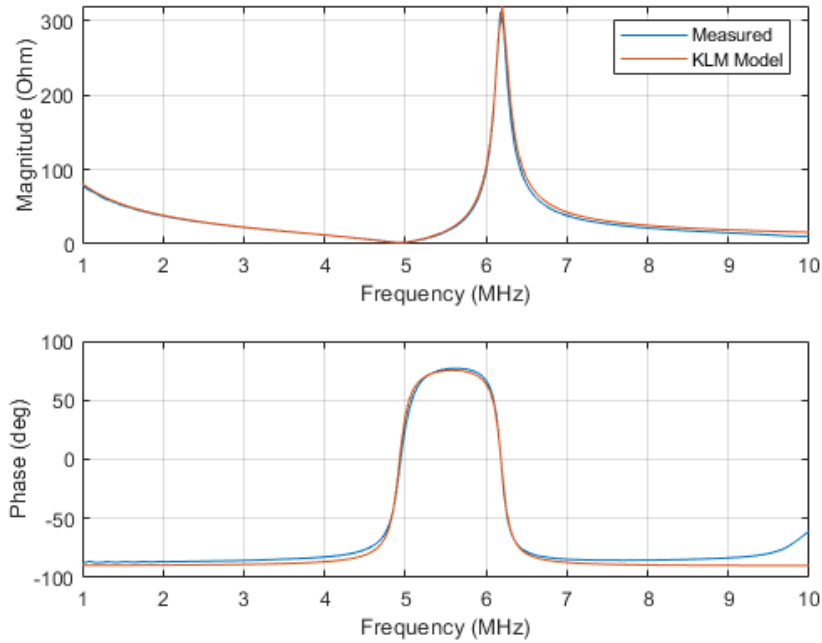


Figure 4.2: Measured electrical impedance from a PZT-5H composite sample, compared to the simulated impedance from the KLM model after fitting the data.

A clamped dielectric constant and attenuation coefficient were selected for each material to fit the KLM models to measured impedances. An example of the measured composite impedance compared to the KLM model is shown in Figure 4.2 for an 8mm diameter PZT-5H composite sample. The material parameters for each composite are given in Table 4.1.

An axisymmetric frequency domain finite element method (FEM) model of the transducer was created using COMSOL. The composite material was modelled as a homogeneous equivalent material, with value of  $\bar{\epsilon}_{33}$  and  $\bar{c}_{33}^E$  calculated based on the parameters from the KLM model fit. An epoxy bond line thickness of 3  $\mu\text{m}$  was selected based on prior experience modelling aluminum lens focused transducers using FEM. This

was justified by using a 3D optical profilometer (Profil3D, Filmetrics, San Diego, CA, USA ) to measure the surface of a composite and a sandblasted lens.

HITU Simulator V2.0 [99], an open-source high-intensity therapeutic ultrasound simulation package, was used to extrapolate the linear pressures from the FEM model, to simulate the non-linear focal pressure from the transducer. This was used to estimate the cavitation threshold voltage ( $V_{Cav}$ ) in water for the sensitivity of each material group, using the threshold for intrinsic cavitation in water of -27.4 MPa [24]. This simulation was later used to also estimate the peak negative focal pressure for each material using the measured sensitivity and peak-peak voltage at cavitation.

Table 4.1: Relevant material properties for each material. The clamped dielectric constants and  $k_{33}$  coupling coefficients from the datasheet for each material are shown for reference. The remaining properties are measured from the fabricated composite materials before bonding the lens or estimated using the KLM model.

Material	PZT5A	3203HD (PZT5H)	PZ54	PZ39	PMN38
Manufacturer	Piezo.com	CTS	Meggitt	Meggitt	TRS
Ceramic Clamped Dielectric Constant	900	1200	1441	1325	7600
Ceramic Coupling Factor, $k_{33}$	0.72	0.78	0.70	0.53	0.64
Thickness ( $\mu\text{m}$ )	309	290	303	312	340
Speed of sound (m/s)	3847	3751	3732	3643	3899
Density ( $\text{kg}/\text{m}^3$ )	4142	4196	4165	6400	4120
Acoustic Impedance (MRayls)	15.9	15.7	15.5	23.2	16.1
Effective Coupling Factor, $kt$	0.61	0.67	0.58	0.55	0.53
KLM Clamped Dielectric Constant	415	700	885	1665	3000
KLM Attenuation Coefficient ( $\text{Np}/\text{m}$ )	85	130	75	140	85

### 4.3.3 EXPERIMENTAL SETUP

The transducers are driven with a unipolar square wave burst generated using a custom pulse generator (pulser) connected through a  $50 \Omega$  coax cable, similar to that described in

[119]. The pulser is triggered using a Tektronix AFG3101C waveform generator and is powered by a 15 VDC wall supply and a TDK-Lambda Z+ series 650V DC power supply.

For both the electrical impedance and sensitivity measurements of the PMN-38 transducers, a bias voltage of 140 V ( $E = 4.1 \text{ kV/cm}$ ) was applied, and the AC signal was applied through a DC-blocking capacitor. For the other experiments, these transducers were simply pulsed in the same manner as the others; the DC-offset of the 8-cycle unipolar pulse biases the PMN-38 material during each burst.

A Precision Acoustics Fiber-optic Hydrophone System was used for pressure measurements. A custom designed passive cavitation detection set-up was used to determine the cavitation thresholds, including an in-house built detection hydrophone [131]. A MATLAB application was developed to automate the test procedure and data collection. The application uses the VISA communication protocol to connect to an oscilloscope to read the hydrophone signal, a function generator and high voltage power supply to control the pulser signal, and a National Instruments USB-6361 Data Acquisition Unit (DAQ) unit to read the cavitation detection transducer signal.

For the sensitivity measurements, the app increments the supply voltage over a range of 0.5 to 1.5 V with a step size of 0.1 V and repeats this over a frequency range of 5 to 7 MHz. The pulse waveform was probed near the transducer end of the cable. Both the hydrophone signal and pulse voltage waveforms were recorded. The voltage signal was processed by applying a low pass IIR filter with a 10 MHz cut-off frequency, and a steepness of 0.85. This was necessary to remove noise and the ringing resulting from the square pulse used to drive the transducer, which would skew the sensitivity measurements

as it was more pronounced at the lower end of the voltage range. The peak-peak voltage was calculated on the waveform after time windowing on the second half of the pulse to avoid the initial voltage overshoot. The same filter was applied to the hydrophone signal, but with minimal impact on the waveform. The sensitivity was taken from the slope of the linear curve fitting peak negative pressure as a function of peak-peak pulse voltage. A linear regression model was fit to the pressure versus voltage data and the slope of this line is the transmit sensitivity at that frequency.

The cavitation threshold measurements were performed in a tank of distilled water with the detection transducer directed at the focus of the transducer under test, and perpendicular to its transmit aperture, as shown in Figure 4.3. The output signal was read from an NI DAQ and processed by setting a threshold based on the sum of the FFT signal between 70 and 120 kHz, the frequency range that the detection device reported the greatest increase in signal power during cavitation events. For each trial, the transducer was pulsed with 100 eight-cycle bursts, over a 100 V range. At each voltage increment, the number of cavitation events is recorded, representing the cavitation probability. A sigmoid curve was fit to the data using non-linear least squares regression and the voltage corresponding to 50% cavitation probability was recorded as the cavitation threshold voltage. The water was vacuum degassed, placed in a covered tank and allowed to acclimatize to atmospheric conditions. A reference transducer was used to initiate cavitation within the test tank until a stable and known cavitation threshold was reached.

Next, an experiment was performed to test for saturation of the piezoelectric material. Using one transducer from each material, the surface pressure was recorded over the full available voltage range of the pulser supply. To prevent damage, the hydrophone was

positioned near the surface of the transducer close to the outer edge. The line from each material was normalized relative to  $V_{Cav}$  for that material. This was repeated for both a single-cycle and an eight-cycle pulse excitation. The pressure and pulse voltage waveforms were recorded and processed in a similar manner to the sensitivity measurements.

Finally, all transducers were tested to failure (or maximum pulser voltage) by pulsing using an 8-cycle, 1 kHz PRF pulse for 10 minutes, at increasing voltage levels. The cavitation threshold measurement was repeated after each voltage level to monitor for transducer failure. This was repeated until the maximum supply voltage (650 V) was reached, or the transducer failed. An increase in  $V_{Cav}$  of more than 10% was designated as failure.

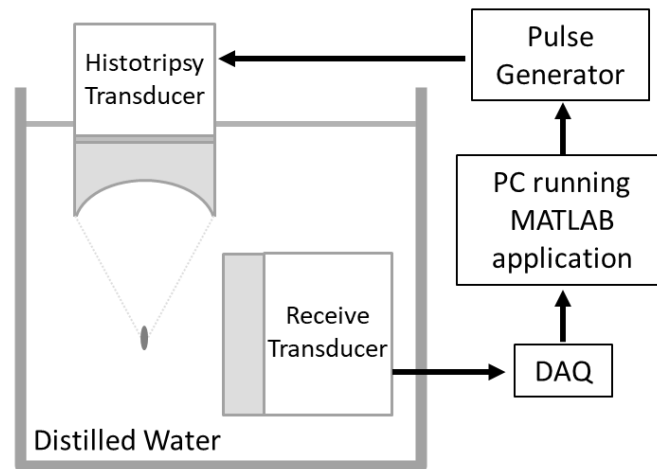


Figure 4.3: Block diagram showing the experimental setup for cavitation threshold measurements.

## 4.4 RESULTS

### 4.4.1 ELECTRICAL IMPEDANCE

The electrical impedance of each finished transducer was measured. Figure 4.4 shows the impedance curve from a typical transducer in each material group. The average electrical impedance at the operating frequency was 26.0, 14.5, 13.1, 12.1, and 6.0  $\Omega$ , for the PZT-5A, PZT-5H, Pz54, Pz39, and PMN-38 transducers, respectively.

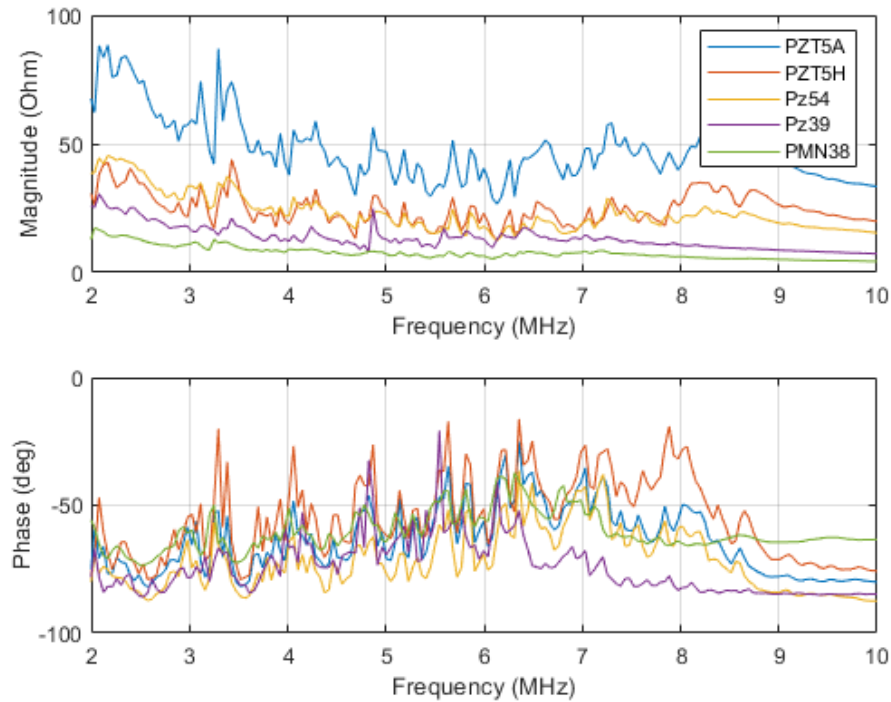


Figure 4.4: Measured electrical impedance magnitude and phase for one transducer from each material group.

### 4.4.2 TRANSMIT SENSITIVITY

The sensitivity versus frequency results from each material is summarized in Figure 4.5. The lines show the mean sensitivity for each set of 4 transducers, with error bars showing the standard deviation. The sensitivity increased with clamped dielectric constant

agreeing as expected from FEM simulations, with the exception of the PMN-38 transducers which had a sensitivity about half the expected value at low drive voltages. The sensitivities generally showed a linearly increasing trend with increasing frequency due to higher focal gain. Although 7 MHz had the highest sensitivity for most of the samples, this was not the optimal operating frequency, which is skewed toward the lower frequencies due to increasing non-linearity and attenuation as frequency increases.

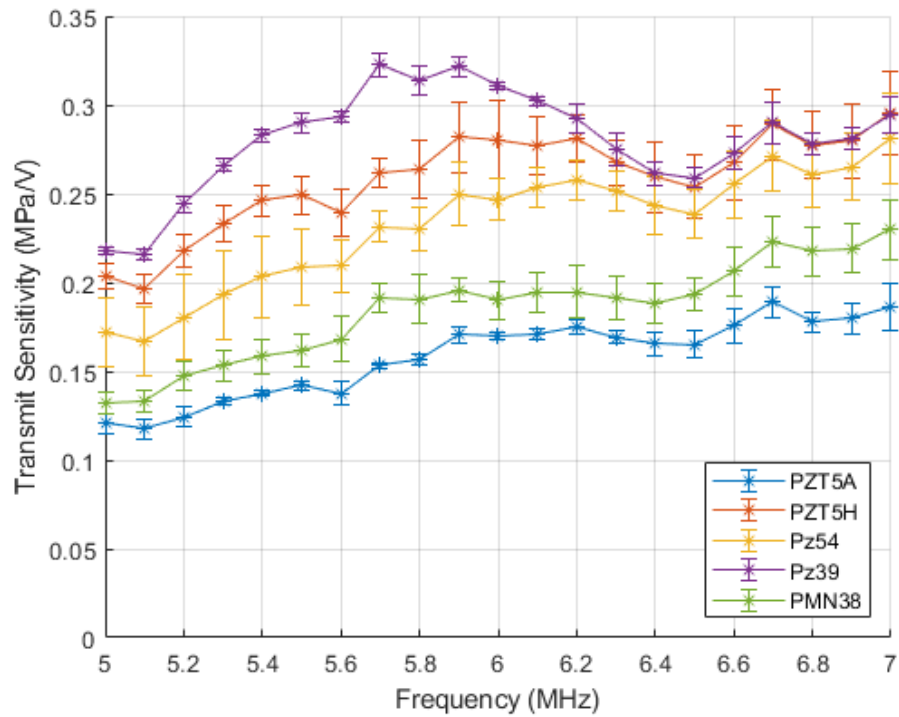


Figure 4.5: Mean transmit sensitivity versus frequency for each material, with error bars showing the standard deviation.

The optimal frequency was found by manually sweeping through the 5-7 MHz frequency range at 0.1 MHz steps, while just above the cavitation threshold and listening for the frequencies at which cavitation stops. The midpoint of these was selected as the operating frequency. There was no significant difference between all the composite

materials, for which an operating frequency of 6.2 MHz was selected, while 5.7 MHz was chosen for the Pz39 transducers. The average measured sensitivity of each material at the selected operating frequency was 0.175, 0.281, 0.258, 0.323 and 0.195 MPa/V for the PZT-5A, PZT-5H, Pz54, Pz39 and PMN-38 transducers, respectively.

#### 4.4.3 CAVITATION THRESHOLD IN WATER

An example cavitation probability S-curve is shown in Figure 4.6 with the dashed line showing the drive voltage corresponding to 50% cavitation probability. Figure 4.7 summarizes the cavitation threshold test results from all 20 transducers. This data followed the same trend as the expected thresholds from simulation, illustrated by the triangles and diamonds.

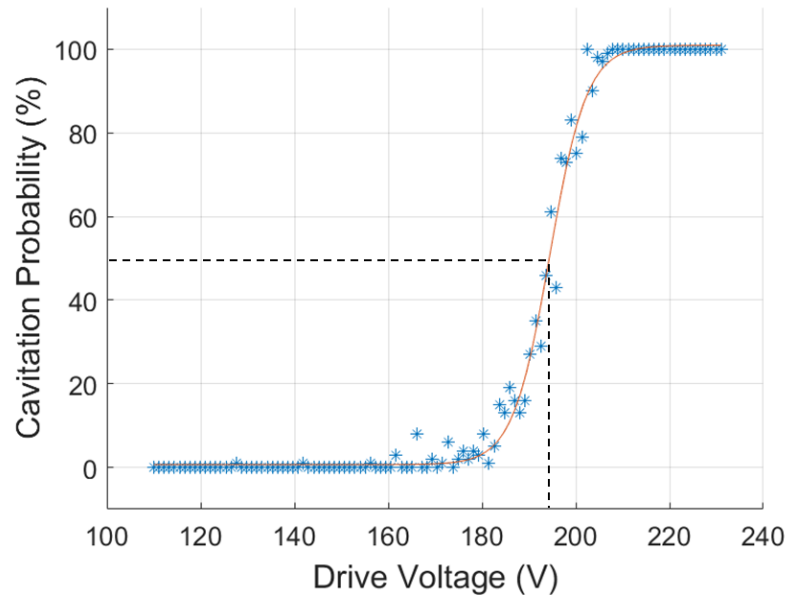


Figure 4.6: Data for a single trial from the cavitation threshold experiment for a PZT-5H transducer.



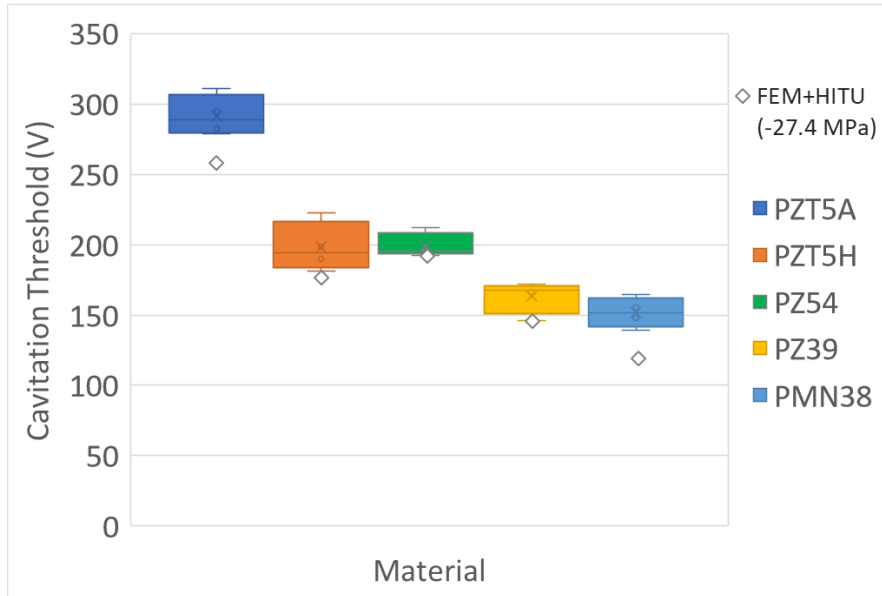


Figure 4.7: Box and whisker plot showing measured cavitation threshold voltage for each material group. The overlaid diamonds show the cavitation threshold voltage predictions for each material, using HITU to non-linearly extrapolate the FEM model sensitivities to the published intrinsic cavitation threshold in water.

As expected from the sensitivity measurements, PZT-5A required the highest voltage to reach the cavitation threshold, an average of 292 Vpp, while PZT-5H and Pz54 both required 199 Vpp, and Pz39 required 163 Vpp. Despite having a low measured sensitivity at low drive levels, PMN-38 had the lowest cavitation threshold voltage of 152 Vpp.

#### 4.4.4 SATURATION

The saturation test results are given in Figure 4.8. In the single cycle test, the measured pressure versus voltage curve for the Pz39, Pz54 and PZT-5H transducers became slightly non-linear at around 430-450 V, this occurred at about 525 V for the PZT-5A transducer. The 8-cycle data shows the output from the PZT-5A and PZT-5H transducers continuing to increase linearly with pulse voltage. The Pz54 transducer experienced failure during testing due to the Parylene matching layer partially delaminating from the lens, resulting

in a decrease in the slope of the curve. The Pz39 transducer experienced a material failure at 335 V during the 8-cycle pulse test, despite no sign of this during the single cycle test. A single cycle pulse wasn't enough to properly bias the PMN-38 transducer, so those results were omitted. When driven by the 8-cycle pulse it began to saturate around 200 V, due to the bias voltage increasing beyond the optimal level. The peak  $d_{33}$  for PMN-38 occurs at 4 kV/cm bias [132], which is  $\sim 136$  V for these transducers.

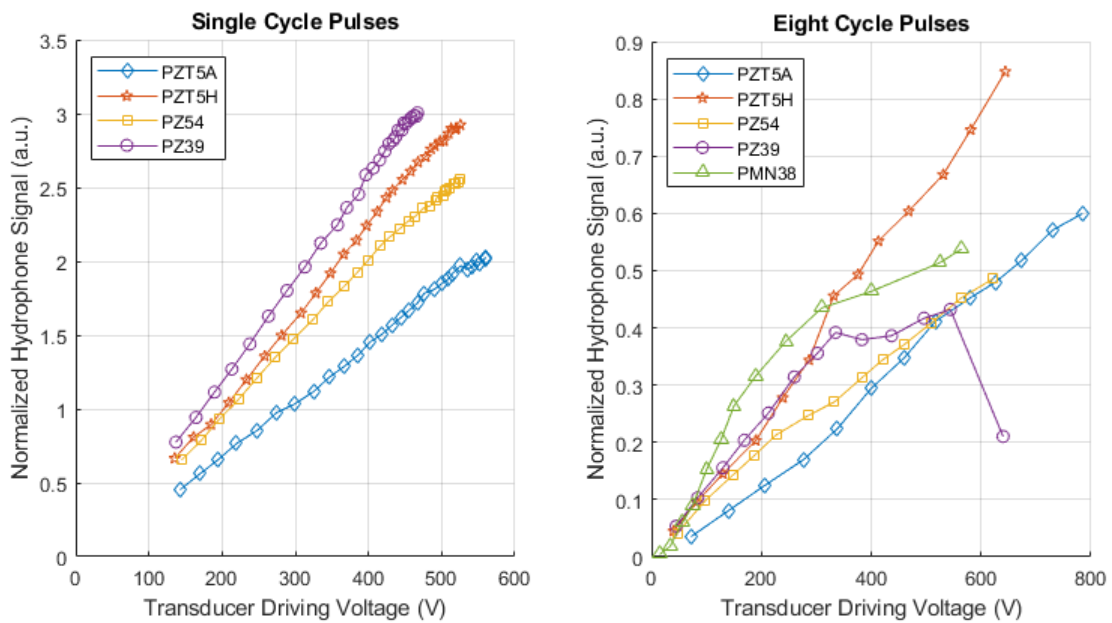


Figure 4.8: Normalized surface pressures recorded using a fiber hydrophone for single cycle pulses (left), and eight cycle pulses (right).

#### 4.4.5 FAILURE TEST

The results from the failure test are shown in Table 4.2. All transducers failed during the test with the exception of two PZT-5A transducers and one Pz54 transducer. The Pz39 transducers all experienced material failures at voltages ranging from 264 – 445 V. The PMN-38 transducers all failed due to either the wirebonds breaking, or the electrode around the wirebond connection burning away. Apart from one transducer where the piezo

delaminated from the lens and one wirebond failure both in the PZT-5H batch, the rest of the failures were caused by the Parylene-C layer partially delaminating from the lens.

Examples of these failures are shown in Figure 4.9.

Table 4.2: Summary of Failure Test Results. The transducers marked with an asterisk failed during the saturation measurements. The transducer peak currents were estimated from the measured voltage waveforms and the electrical impedances.

Material	Transducer Label	Failure Mode	Transducer Peak-Peak Voltage at Failure (V)	Transducer Peak Current at Failure (A)
PZT5A	18	Parylene delamination	Missing data	Missing data
	19	Survived	742	14
	22	Parylene delamination	626	12
	29	Survived	756	15
PMN38	20	Wirebond	Missing data	Missing data
	23	Wirebond	375	31
	41	Electrode	394	33
	43	Electrode	525	43
PZT5H	24	Parylene delamination	581	20
	34	Parylene delamination	637	22
	42	Piezo delamination	640	22
	44	Wirebond	580	20
PZ39	25	Material failure	264	11
	26	Material failure	445	18
	40	Material failure	383	16
	45	Material failure *	335	14
PZ54	27	Parylene delamination	574	22
	37	Survived	647	25
	47	Parylene delamination *	500	19
	48	Parylene delamination	651	25



Figure 4.9: Examples of transducer failures, Parylene delamination (left) and electrode failure (right).

#### 4.5 COMPARISON TO SIMULATIONS

In Figure 4.10, the simulated impedance curves from the FEM model are compared to measurements for each material. Overall, they line up very well, with the main differences being the shape and location of the spurious resonance modes, which is a result of the varying thickness of the lens, and the phase at frequencies above resonance.

The simulated sensitivities from the FEM model at the operating frequency, were 0.179, 0.265, 0.247, 0.317, and 0.378 MPa/V for the PZT-5A, PZT-5H, Pz54, Pz39 and PMN-38 transducers, respectively. A detailed comparison of measurements to simulations from 5- to 7-MHz is shown in Figure 4.11, displaying excellent agreement for all except the PMN-38 transducer. The reason for this is still unknown but is likely related to the method of biasing the transducer during testing.

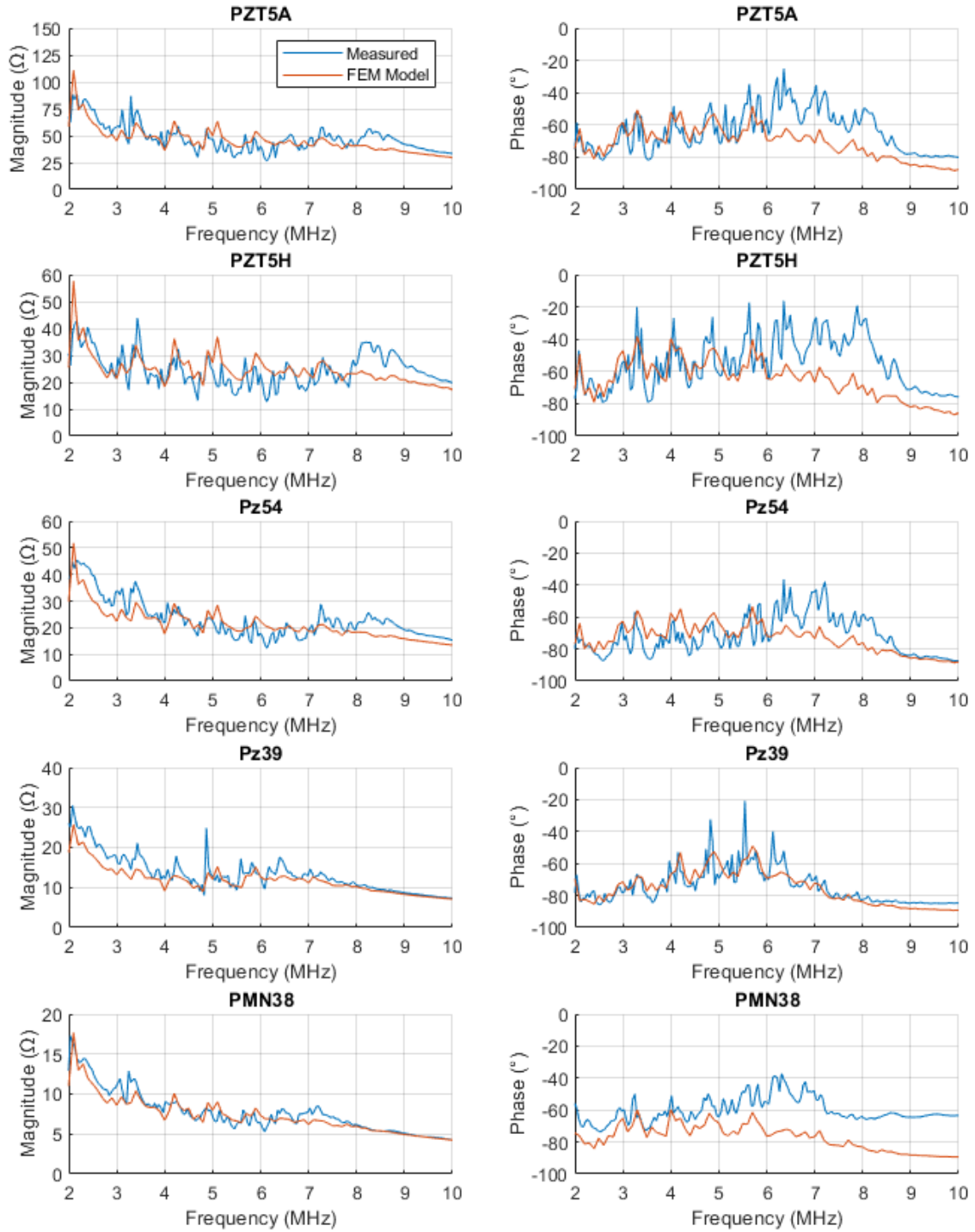


Figure 4.10: Measured electrical impedance magnitude and phase for one transducer from each material group, compared to the impedance simulated using the FEM model.

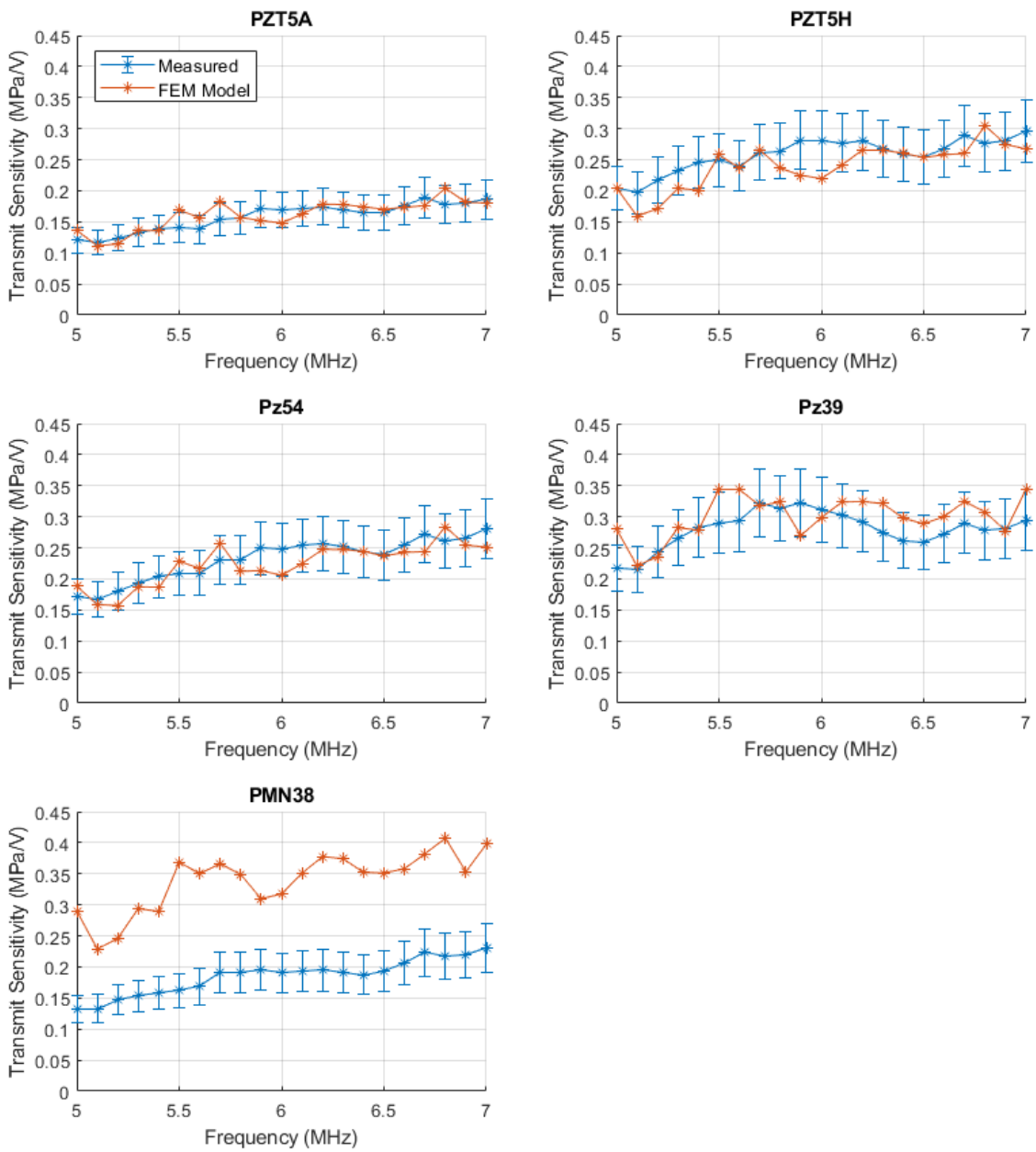


Figure 4.11: Mean transmit sensitivity versus frequency for each material, compared to the simulated transmit sensitivity from the FEM model. The error bars on the measured data show the  $\pm 17\%$  hydrophone sensitivity uncertainty.

The expected cavitation threshold voltage simulated using the FEM model in combination with the HITU model agreed fairly well with measurements, as shown in Figure 4.7. The relative distribution across different materials was an excellent match, although the simulations predicted a lower threshold in general. This is believed to be a result of the surface pressure distribution modelled as uniform in the HITU simulation, when in reality it is weighted more toward to the inner part of the transmitting surface, as shown in Figure 4.12. This would result in more non-linearity in the transmitted pressure wave.

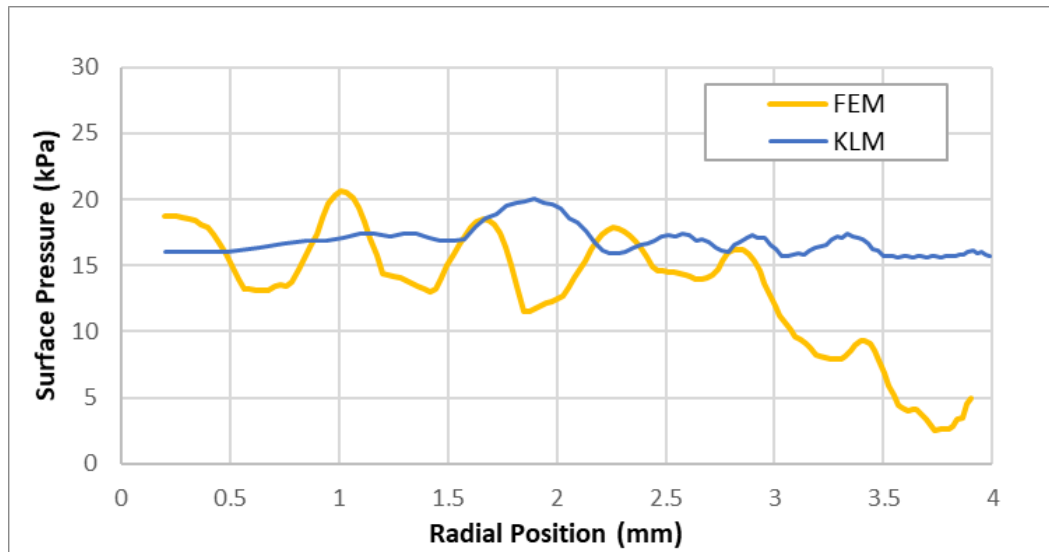


Figure 4.12: Surface pressure along the lens from the center to the perimeter of the transducer. Results from the FEM and KLM models are compared.

#### 4.6 DISCUSSION

The sensitivity measurements highlight the importance of using the actual measured voltage near the transducer for calculating the sensitivity, instead of simply using the supply voltage as was previously done. If the latter method was used, the PMN-38 and PZT-5A transducer would have roughly the same sensitivity, however due to the greater

impedance mismatch between the cable and transducer for the PMN-38 transducers, the transducer pulse voltage was about half the supply voltage; in contrast the voltage across the other transducers was about 1.2 – 1.5 times higher than the supply voltage.

The PMN-38 transducers had a mean non-linearly extrapolated peak negative pressure at cavitation (using measured sensitivity and voltage at cavitation in the HITU model) between -21 MPa, while the other four materials ranged from -28.6 to -30.3 MPa. Using the average extrapolated pressure at cavitation from the other materials and the measured cavitation threshold voltages for PMN-38, the average sensitivity should be 0.348 MPa/V, which is much higher than the measured value and is closer to the expected 0.378 MPa/V from the FEM model.

An alternative approach to estimating the focal pressure is to use the KLM-based transducer model outlined in [100]. This model divides an axisymmetric transducer into a set of parallel connected 1D transducer models. While the FEM model produces more accurate results, it takes longer to run and isn't as widely available as MATLAB so there are cases where the KLM approach is still valuable. As shown by Figure 4.12, the KLM model produces a near uniform surface pressure, while in the FEM model the pressure drops off near the perimeter of the lens. A reasonable estimate of the focal pressure was obtained by reducing the transducer radius in the KLM model to 3.33 mm to fit the measured focal pressure. The mean surface pressure across the transducer face from the KLM model was multiplied by the focal gain to estimate the transmit sensitivity (MPa/V) at the focus. While it may seem impractical to use this approach when it requires arbitrarily selecting an equivalent transducer diameter based on previous pressure measurements from



a transducer, this can be useful to quickly estimate the focal pressure for new composite designs based on a given lens geometry.

When the supply voltage was increased above 450 V, the pulser output began to saturate, which was worse for the higher dielectric materials. This is why the saturation test graph shows that PZT-5A transducer was tested to a higher voltage. The Pz39 material failed when driven with 5.7 MHz, 8-cycle, 1 kHz PRF pulses at 264 V or above. This presents itself as a gradual failure, characterized by reduced pressure output and a change in electrical impedance, that could be easily mistaken for de-poling. To rule this out, failed Pz39 transducers were re-poled using a 600V DC supply, at 100°C for up to 4 hours, with no change observed in electrical impedance or performance. Additionally, given that the same transducer that failed at 335 V in the 8-cycle test, was pulsed to 460 V using a single cycle without failing, this is thought to be resulting from fractures in the ceramic due to stress risers around the pores, as higher stresses are present in a multi-cycle pulse.

The peak current at failure for the PMN-38 transducers was 60% higher than the Pz54 transducer (2nd highest), which could explain the electrode failure. Increasing the electrode thickness and/or distributing wirebonds over more contact points could solve this problem.

The Parylene delamination was limited to a roughly 2.5 - 3 mm diameter circle concentric with the lens, which is consistent with the region of high surface pressure from the FEM simulation graph in Figure 4.12. Also, the ring-like pattern roughly lines up with the axially symmetric local stress maxima from the model. The Parylene-Aluminum adhesion could be improved by optimizing the sand grit, plasma etching the lens surface, and/or using a chemical adhesion promoter such as Silane A-174. In future builds,

wirebonds should be placed closer to the outer edge of the transducer to minimize the vibration they experience.

The Parylene delamination failure mode makes it difficult to directly compare material performance as this is a property of the transducer build process, not the material used. To compare the performance for each material, the linearly extrapolated pressure at failure was calculated by multiplying the sensitivity by the voltage at failure for each transducer. However, this didn't show any statistically significant differences between the transducers that survived and any of the failure modes. It may be tempting to say Pz54 is a better choice than PZT-5H, based on the results from transducers 37, 42 and 44. But, given that they share the same fabrication methods, including the electrode, this outcome is likely just due to tolerances in the build process.

With a 3.9 mm square hole for the imaging array added to the center of the transducer, the simulated sensitivity is reduced by ~32%. Comparing this voltage to the observed voltage at failure, an 8 mm diameter co-registered transducer built with PZT-5H is expected to have at least a factor of 2 safety margin above its cavitation threshold voltage in water. The simulated in-brain cavitation threshold from Landry et al. [18] was -31.6 MPa. At this higher focal pressure, the PZT-5H transducers would be expected to cavitate at 346 V, which is still below the lowest failure voltage that was observed.

#### 4.7 CONCLUSION

The performance of broadband lens-focused 8 mm diameter miniature histotripsy transducers fabricated using five piezoelectric materials was evaluated. As expected, the materials with higher clamped dielectric constant had higher transmit sensitivity and lower

cavitation threshold voltage. The results were non-linearly extrapolated using HITU simulator yielding the anticipated peak negative pressures at cavitation. These were similar to the published values for free-field cavitation in water. The pressure output for these transducers did not saturate at high driving voltages ( $> 500\text{V}$  for PZT-5A) as previously thought [133], with the exception of PMN-38 which was non-linear due to the bias voltage increasing.

PMN-38 and Pz39 were the most sensitive materials, but both consistently failed. PMN-38 failures were attributed to the higher current, while the porous structure of Pz39 is thought to be the cause of its failures. Even though the PZT-5A transducers were driven to a higher voltage, because of the lower sensitivity the linearly extrapolated pressure was lower than the other materials. There was no significant difference between failure performance of Pz54 and PZT-5H (CTS 3203HD) transducers, but the latter performed better during the saturation experiment and had a slightly higher sensitivity and lower cavitation threshold voltage.

## **CHAPTER 5:**

### **AN 8 MM ENDOSCOPIC HISTOTRIPSY ARRAY WITH INTEGRATED HIGH-RESOLUTION ULTRASOUND IMAGING**

#### **5.1 PREAMBLE**

The outcome of the previous section informed the selection of PZT-5H composite as the best candidate for the miniature histotripsy transducer. Experience with using lens-focussed devices in experiments [18] suggested that an annular array based design could improve on two weak points in the existing device: the concave lens made acoustic coupling more challenging, and the fixed focal length limited the ablation depth and possibly the ablation rate. The aim of this study was to create an 8 mm diameter annular array histotripsy transducer with integrated ultrasound imaging and compare the performance to a lens-based transducer similar to the one described in the previous study but with a central hole. The work presented in this chapter is based on a manuscript that has been accepted for publication in “Ultrasonics”. Some content in the introduction section repeated from Chapter 1 has been left to retain the flow of the manuscript.

## 5.2 INTRODUCTION

Minimally invasive neurosurgical approaches to tumor resection result in improved postoperative outcomes, including decreased risk of complications, compared to full craniotomies. Endoscopic tools and preoperative planning based on brain imaging, usually magnetic resonance imaging (MRI), allow surgeons to significantly reduce the craniotomy size, leading to less surgical exploration and brain retraction [3], [5]. Craniotomies often result in the brain shifting from the position in the preoperative scans, making them less accurate [6]. The most commonly used tool in brain surgeries are ultrasonic aspirators, such as the Cavitron Ultrasonic Surgical Aspirator (CUSA), which have relatively large ablation sizes and lack image guidance [7]. This limitation in combination with brain shift restricts the extent of resection, which is directly related to patient survival and quality of life outcomes [8], [9]. Surgeons also don't want to risk over resecting healthy tissue to ensure the cancer is fully removed. For this reason, residual tumor tissue is often left behind post-surgery. This is particularly dangerous for glioblastoma (GBM) as it is an aggressive form of brain cancer, with a mean patient survival time of only 15 months [11]. A retrospective review of primary GBM resection in 128 patients found a mean residual tumor volume of 1.2 cm<sup>3</sup> based on comparing preoperative and postoperative MR images [134]. Intraoperative ultrasound is a promising method of correcting the mismatch between the intraoperative and preoperative brain position [6]. Based on this, there is a need for a high precision surgical tool with integrated ultrasound imaging.

Histotripsy is a non-thermal, non-ionizing, mechanical ablation technique that works through focusing ultrasound to generate cavitation bubbles at a target location [14]. Preclinical research has shown that histotripsy treatment produces a stronger immune

response than radiotherapy or thermal ablation and produced an abscopal effect (regression of untreated tumors) [19]. The abscopal effect was also observed in a case report from a preclinical trial on treating liver tumors with histotripsy [20]. This cavitation-based ablation method results in minimal cellular damage margins, as small as 100  $\mu\text{m}$  [18], at the boundaries of the ablated region. Additionally, it can be readily monitored using ultrasound imaging in real time.

There has been significant progress on non-invasive methods of brain tumor ablation in recent years. Transcranial HIFU has successfully been used to partially ablate a recurrent glioblastoma tumor with no adverse effects [30]. More recently, transcranial histotripsy has been demonstrated using a 128 element, 700 kHz, MR compatible phased array transducer inside an MRI scanner to treat eight pigs *in vivo*, with a section of the pig skull replaced with a human cadaver skull cap [31]. While this is a very promising step toward a fully non-invasive method of brain tumor ablation, the mean shift between the target and observed ablation zone was 2.3 mm, which could lead to residual tumor or over resection comparable to surgical resection. Also, this surgical approach requires MR imaging to monitor the progress, which is time consuming, expensive, and often has limited availability.

While there are several existing minimally invasive ablation modalities used for brain tumor resection that can improve treatment outcomes, particular for unresectable tumors, including radiofrequency (RF) ablation, laser interstitial therapy (LITT), radiosurgery, and high intensity focussed ultrasound (HIFU) thermal ablation, these are still limited in accuracy by the image guidance techniques currently used in surgical resection [136], [13], [45]. The addition of a single surgical tool combining real time high-resolution

(40 - 130  $\mu\text{m}$ ) ultrasound image guidance integrated with high-precision ( $\sim 0.5 - 1 \text{ mm}$ ) non-thermal ablation would improve the accuracy beyond what is currently available [46]. We hypothesize that a small form-factor image guided histotripsy system designed to fit into the current minimally invasive neurosurgical workflow could be used in conjunction with existing surgical instruments to improve the extent of resection.

Figure 5.1 shows a concept diagram of the proposed histotripsy-based surgical tool using integrated intraoperative ultrasound to target and ablate residual tumor remaining after surgical resection of a 40 mm tumor through a 20 mm diameter burr hole. The resection cavity would be filled with saline as required to allow the ultrasound to be acoustically coupled into the brain.

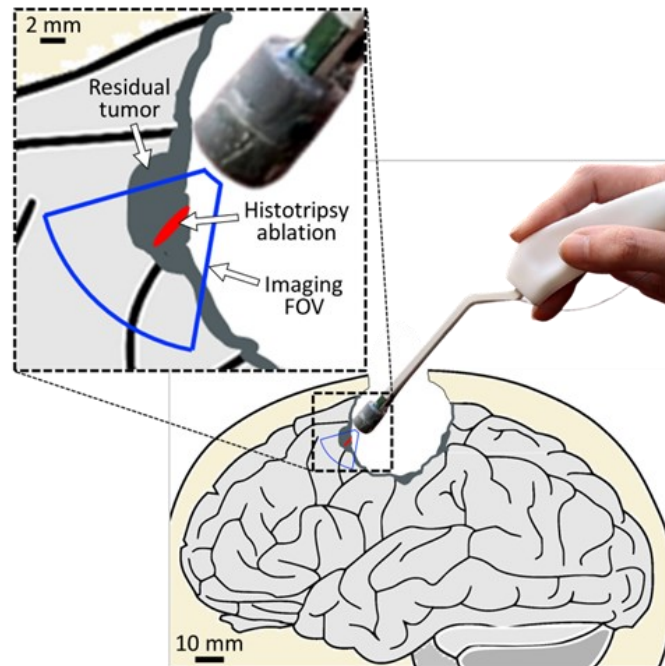


Figure 5.1: Concept diagram of an image guided histotripsy device ablating residual tumor during removal of a 40 mm tumor through a 20 mm burr hole. The field-of-view of the ultrasound imaging phased array, the histotripsy focal region and the residual tumor are annotated in the inset image.

A future iteration of this device may include aspiration for removing the homogenized tissue but is beyond the scope of this prototype. Although this concept diagram shows a superficial brain tumor, this tool would also be compatible with tubular retractors (~12 - 28 mm width) currently used for accessing deep-seated tumors [137].

Previous miniature histotripsy transducers have typically been implemented using a lens focussed design. A piezoelectric composite is bonded to an acoustic lens, typically made from machined aluminum [100], [130], [138] or 3D printed resin [101], [139], surrounded by a case to air-back the transducer. To date, the only combined ultrasound imaging and cavitation-based ablation device with an endoscopic form factor reported in the literature is based on this concept [18], [100]. The ablation device is a 5 MHz, 1-3 PZT-5A/epoxy composite bonded to a 10 mm diameter elliptically focussed aluminum lens with 7 mm focal length. It has a 3D printed case surrounding the lens that adds 1.5-2 mm to the overall diameter and is coated in a Parylene-C matching layer. There is a 3.9 mm square hole in the centre for a 3.6 by 3.8 mm, 64-element, 30 MHz phased array imaging probe [117].

Using a concave lens limits the device to a fixed focus, with a maximum operating depth limited by the lens thickness. For example, an 8 mm lens-based transducer with 7 mm focal length (from the bottom of the lens curvature) can ablate at a maximum depth of 4.7 mm, while the 8 mm annular array can operate at depths ranging from 3 - 8 mm. Also, an annular array can be used to electronically steer the focus during treatment offering an increased depth of field, theoretically increasing the ablation rate.



In this work, we present an annular array focussed histotripsy device as the next step in the pursuit of a fully endoscopic combined ultrasound imaging and ablation probe. The 16-element array has an 8 mm outer diameter, with a 3.9 mm square hole to accommodate the existing 30 MHz imaging probe [117]. A 12-cycle pulse is used to generate a dense cavitation bubble cloud at the focus using shock-scattering histotripsy. The design and fabrication of both a forward-looking and side-looking histotripsy array form factor is described, with the intent of demonstrating that this concept could be adapted to different configurations, providing more options for tumor access. The device was characterized by measuring the electrical impedance, acoustic field, and cavitation threshold voltage in water. To allow for a direct comparison between the array and lens focussing methods, an 8 mm diameter aluminum lens-focussed transducer was also fabricated and characterised. The measured results from both the array and lens-based transducer are compared to simulations. Finally, the array was used to produce a lesion in a rat brain *in vivo*, while monitoring treatment in real time using b-mode imaging with a Doppler overlay used to visualize the cavitation bubble cloud.

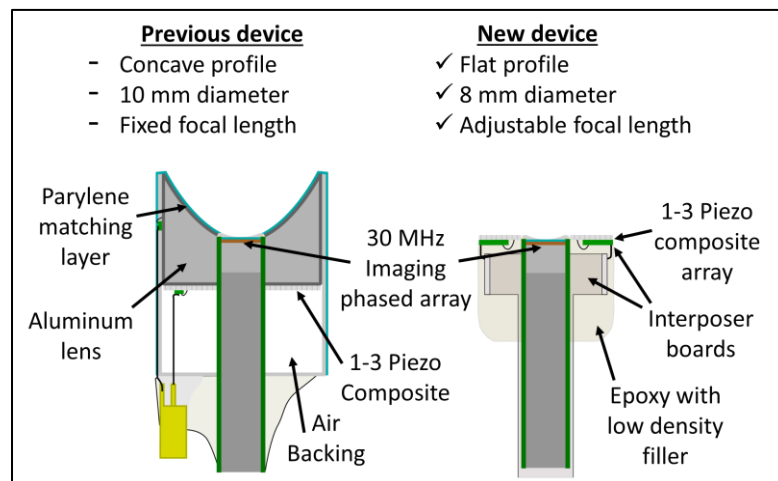


Figure 5.2: Diagram of the new image-guided annular-array histotripsy transducer concept compared to the previously published image-guided lens-focussed transducer.

## 5.3 METHODS

### 5.3.1 TRANSDUCER DESIGN AND FABRICATION

Figure 5.2 shows the annular histotripsy array design compared to the previous 10 mm aluminum lens-based design [100]. The array was fabricated using a 5 MHz, 1-3 dice and fill PZT-5H/epoxy composite with a 45% volume fraction (Smart Materials Corp., Florida, USA). A 355 nm picosecond laser micromachining system (Oxford Lasers Inc., Oxfordshire, UK) was used to cut the composite to an 8 mm outer diameter with a 3.9 mm square hole in the center. The composite was mounted on a glass slide using bonding wax, and the array elements were laser etched into the electrode on the negative side. The array pattern was designed for 16 equal area elements separated by 20  $\mu\text{m}$  wide kerfs between elements, cut 30  $\mu\text{m}$  deep into the composite.

Table 5.1 shows the design details for each element in the annular array, including inner and outer radii, width relative to the acoustic wavelength in water, and active area. The histotripsy array was designed to make use of the entire available aperture, the inner radius of element 1 starts just outside the width of the square hole, and the kerf between element 4 and 5 intersects the corners of the hole. This means the inner four elements were each divided into four sections, resulting in reduced area, and requiring a method of electrically connecting the sections. The number of array elements was selected based on the results from FEM simulations, shown in Figure 5.3.

Table 5.1: Design details of the 16-element annular array.

Element Number	Inner Radius (mm)	Outer Radius (mm)	Element Width (relative to $\lambda_{\text{water}}$ )	Element Area (mm <sup>2</sup> )
1	2.109	2.256	0.53	1.196
2	2.276	2.412	0.49	1.496
3	2.432	2.558	0.45	1.700
4	2.578	2.697	0.43	1.850
5	2.717	2.828	0.40	1.945
6	2.848	2.954	0.38	1.928
7	2.974	3.075	0.36	1.912
8	3.095	3.191	0.35	1.897
9	3.211	3.303	0.33	1.883
10	3.323	3.411	0.32	1.868
11	3.431	3.516	0.31	1.855
12	3.536	3.618	0.29	1.842
13	3.638	3.717	0.28	1.829
14	3.737	3.814	0.28	1.816
15	3.834	3.908	0.27	1.804
16	3.928	4.000	0.26	1.792

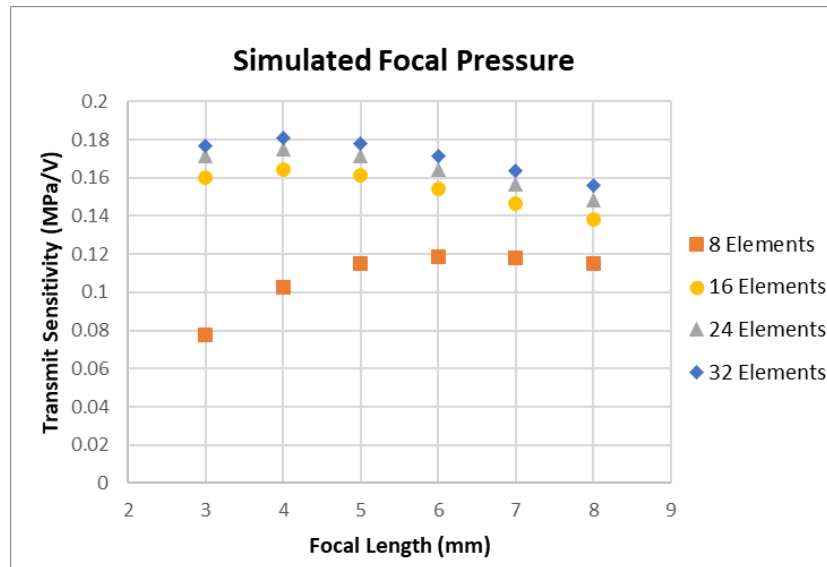


Figure 5.3: Linear focal pressure per volt versus focal length for annular arrays with 8, 16, 24 and 32 elements, simulated using FEM.

The fabrication of the forward-looking form factor histotripsy array is shown in shown in Figure 5.4. For this design, a set of two interconnect flexible PCBs were used to route electrical signals from the cable bundle connector to the array elements. One board was glued to the back of the array, and used to wirebond array elements to traces that are routed to pads around the perimeter. The black lines in Figure 5.4c are used to emphasize the wirebonds used to connect to the four sections of element 1, and the blue dashed line indicates the trace on the backing circuit board. The wirebond contact points were potted with alumina loaded epoxy, and wires were soldered to the pads. Then the array was backed with a low acoustic impedance epoxy mixture (West System 105/205/410). Silicone mold making rubber was used to make a 3.9 mm square cross section post to fill the hole during the backing step. The second board was mounted perpendicular to the array, wrapped around a cast epoxy part to line up the pads with the wires from the first board. The wires were soldered to the pads to connect the boards and potted in the same backing epoxy mixture. The front of the array was grounded by wire bonding to a small copper pad, which was connected to the ground plane on the flexible PCB by soldering a wire. No matching layer was applied.

The side-looking form factor histotripsy array was fabricated using a similar method, as shown in Figure 5.5. The end of the T-shaped flex PCB was removed, and the traces were exposed by scraping off the solder mask. The array elements were wirebonded to the traces, and 4-pad PCB sections were glued to the back of the array at three of the corners to connect the four inner elements around the hole. The wirebonds used to connect the four sections of element 1 are highlighted by the black lines in Figure 5.5a.

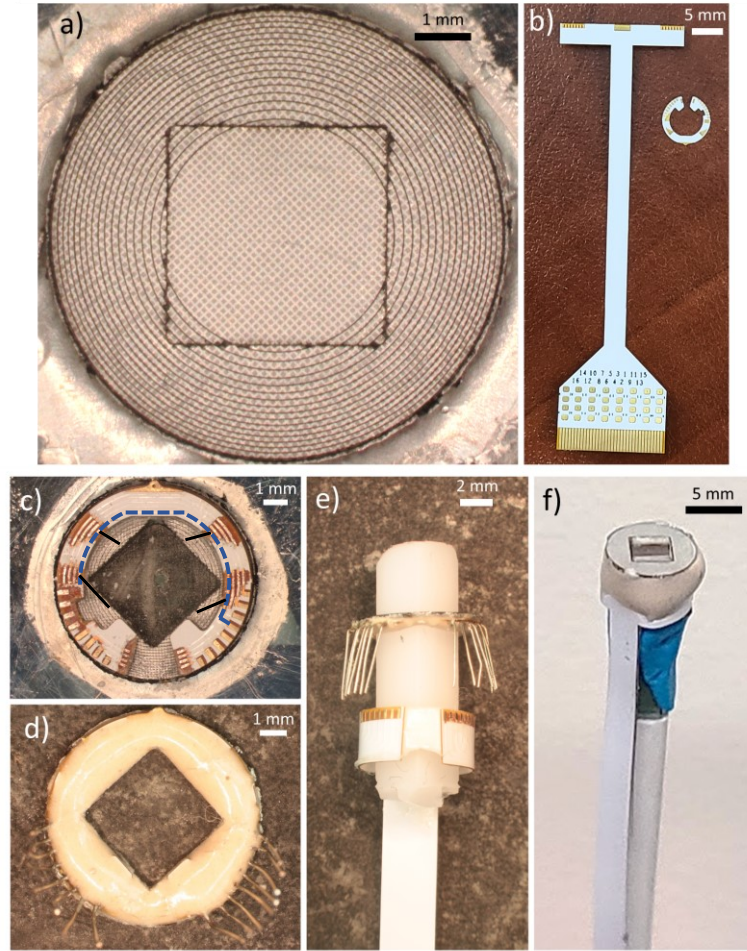


Figure 5.4: Fabrication of the forward-looking annular array. (a) Piezoelectric composite with array outline laser diced and elements etched. (b) Two interposer PCBs used to route array elements to cable bundle. (c) Array with interposer PCB bonded to back, with wirebonds used to connect array elements to traces. (d) Array after soldering wires to pads and applying backing epoxy. (e) Array stack and PCB before soldering wires to pads. (f) Finished array with imaging probe attached.

The 8 mm diameter lens-focussed transducer was based on the design described in a paper by Woodacre et al. [100]. The machined aluminum lens was bonded to the same PZT-5H composite material used for the array, using West System 105/205 epoxy resin. To minimize other differences between the lens transducer and the array, the transducer was backed with the same low acoustic impedance epoxy mixture used to back the annular array design instead of air-backing.

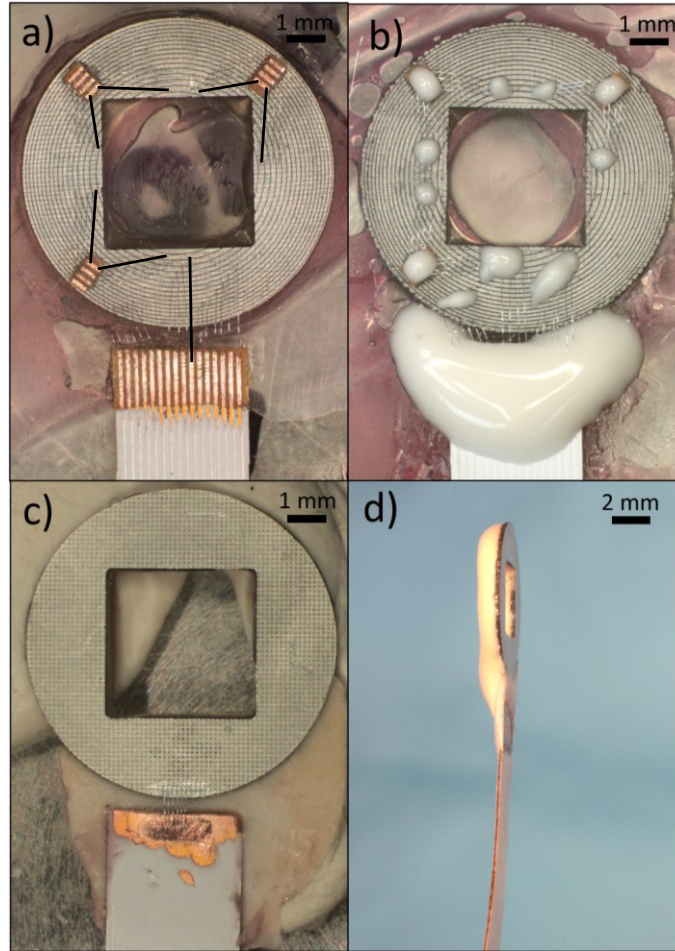


Figure 5.5: Fabrication of an annular array with a side-looking form factor. (a) Piezoelectric composite after laser dicing outline, etching array elements, and wirebonding elements to traces on the PCB. Small sections of the PCB were used to connect the inner four elements around the hole. (b) Wirebond contact points potted in alumina-loaded epoxy. (c) Front of the array after wirebonding to the ground plane on the PCB. (d) Side view of the finished array.

### 5.3.2 TRANSDUCER CHARACTERIZATION

The electrical impedance of each array element was measured using an Agilent 4294A Precision Impedance Analyser (Agilent Technologies, Santa Clara, USA). A Van Dyke equivalent circuit model was fit to the mean impedance data. This was modelled in LTSPICE and used to determine the shunt capacitor value that tuned the impedance

magnitude of each array element to  $50 \Omega$  at the resonance frequency, to match the impedance of the flex PCB.

A custom designed 16 channel high voltage pulse generator based on [119], shown in Figure 5.6, was used to drive the array. This pulser consists of a motherboard that uses an FPGA with a 250 MHz clock frequency to precisely generate beamforming delays with 4 ns temporal resolution. The signals from the FPGA are routed to four PCIe slots on the motherboard. Each slot has a four channel pulser card with a gate driver used to switch an N-channel SiCFET to output a high voltage pulse. A 0 - 650 V adjustable high voltage supply (TDK-Lambda Z+ series, Neptune, NJ, USA) is connected to a capacitor bank on the pulser card capable of supplying the high instantaneous current required during switching. The outputs from the pulser cards are routed through an interposer board to a 2 m long cable bundle; the individual cable for each channel has a DC resistance of  $15 \pm 0.5 \Omega$ . The flexible PCB used to connect the cable bundle to the array has a 470 pF shunt tuning capacitor across each array element for impedance matching. The lens focussed transducer was pulsed using a single channel pulser board, the same HV supply and a signal generator.

The acoustic pressure field was measured using a Fiber-optic Hydrophone System (Precision Acoustics Ltd, Dorchester, UK), with the hydrophone fiber mounted in a water tank pointing vertically up toward the surface of the water. The annular array was mounted to a 3-axis servo-motor positioning stage (Thorlabs Inc., Newton, NJ, USA) and lowered into the tank so that the transmitting surface is normal to the hydrophone fiber. The hydrophone has an outer diameter of  $125 \mu\text{m}$  with a sensor diameter of  $10 \mu\text{m}$ , and a nominal sensitivity at 5.4 MHz of 231.63 mV/MPa.



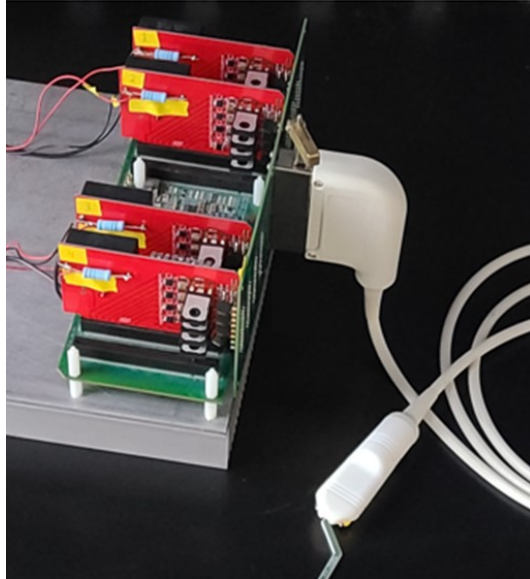


Figure 5.6: The custom designed 16-channel pulse generator connected to the cable bundle. The motherboard (green) contains an FPGA which was used to trigger N-FETs on the pulser cards (red) with the required beamforming delays to focus the array.

The transmit sensitivity (linear focal pressure versus voltage) of the array was measured with it focussed to 3 to 8 mm in 1 mm steps, at the array resonance frequency for a supply voltage of 1 V. This was measured by focussing the array to a given point, and using the positioning stage to move the array until the hydrophone was measuring the peak focal pressure. The hydrophone output waveform and the voltage waveform across array element 8 was recorded. This along with the hydrophone calibration was used to calculate the transmit sensitivity of the array. The pulse frequency was selected by manually adjusting the frequency during hydrophone testing to find the frequency that had the maximum transmit sensitivity, then the data was recorded at this frequency. For simplicity it was assumed that the optimal frequency didn't change between array foci, so the pulse frequency was selected using the 5 mm focus.



For each focal length the acoustic field was recorded over a grid of points spanning 2 mm in the radial direction and 5 mm in the axial direction. The step resolution was 0.05 mm and 0.1 mm in the radial and axial directions, respectively. A total of 2091 data points were recorded for each radiation pattern.

One metric that was used to compare the performance of the transducers at high drive levels was the cavitation threshold voltage ( $V_{\text{Cav}}$ ), which is defined as the peak-peak pulse voltage at which cavitation occurs in water for 50% of the pulses. This was measured using a custom passive cavitation detection set-up described in detail in [131]. The transducer is pulsed in a water tank, with a custom detection hydrophone positioned nearby. The pulse voltage is measured at the transducer end of the cable using an oscilloscope. The hydrophone signal is recorded by an NI USB-6343 data acquisition (DAQ) device (National Instruments, Austin, TX, USA) as the pulse voltage is gradually incremented over a range, with 300 pulses at each voltage. The frequency spectrum of the received signal is used to determine if cavitation occurred for each individual pulse. A sigmoid curve is fit to the data of the percentage of pulses that produced cavitation at each voltage level, and from this the 50% cavitation voltage is estimated. All cavitation testing and the ablation experiment were done using a 12-cycle pulse with a 1 kHz pulse repetition frequency (PRF).

### 5.3.3 ACOUSTIC SIMULATIONS

A Finite Element Method (FEM) model of the transducer with 2D axial symmetry was developed using the Acoustics Module in COMSOL Multiphysics. The square hole in the transducer was treated as a circular hole with equivalent area. The 1-3 piezoelectric

composite material was modelled as an equivalent homogenous material using the equations developed by Smith and Auld for thickness mode oscillations [96], which are used to calculate equivalent piezoelectric properties from the material properties of PZT-5H ceramic, the properties of the epoxy, and the composite volume fraction. The Poisson's ratio and loss factor of the epoxy were adjusted to match the measured electrical impedance of an unloaded (in air) composite sample. The backing layer was modeled using the same principle, with equivalent material properties calculated using the epoxy properties, the micro-balloon filler properties, and the mix ratio. A loss factor of 0.02 was applied to the  $c_{33}^E$  element of the composite elasticity matrix, while the  $c_{13}^E$  element was fully damped to suppress lateral waves in the composite.

The FEM model was used to compare the focal pressure for various focal lengths from arrays with 8, 16, 24, and 32 elements. The result from this model study is shown in Figure 5.3; there was a significant improvement in focal pressure between 8 and 16 elements, and only a minor increase as a greater number of elements was used. Based on this data, a 16-element array was selected to keep the array fabrication and pulser complexity low.

To avoid potential hydrophone damage, the focal pressure was only measured at low voltages ( $< 1$  MPa). Estimates of the array peak focal pressure when driven at  $V_{Cav}$  were obtained using HITU Simulator v2.0 [99]. This was done for the lens transducer, and the array focussed to each of the focal lengths tested at low voltage. The transmit sensitivity in the model was scaled to match measurements at low voltage (at linear pressures), then the source pressure was scaled by the measured  $V_{Cav}$ .

The computational grid settings used in the HITU code for the 2D axisymmetric simulation were: 512 harmonics, 15 points per wavelength in the r-direction, and 80 points per wavelength in the z-direction. It should be noted that the code scales the radial grid based on number of harmonics. This resulted in a grid with a step size of 3.43  $\mu\text{m}$  in the axial (z) direction and 2.06  $\mu\text{m}$  in the radial (r) direction, for a total of 874 grid points across the transducer face.

By default, the pressure source is calculated by approximating a spherically focussed transducer as an equivalent source originating from a plane located at  $z = d - \sqrt{d^2 - a^2}$ , where “d” is the focal length and “a” is the transducer radius. While this approximation seems to be valid for higher f-numbers (i.e. the 7 mm focal length pressure output agreed with expected results), the low f-number of the array meant that the resulting focal pressure quickly diverged from the expected result as the array f-number was decreased. To solve this problem, a line of points across the face of the array was defined in the FEM model, and the complex pressure was evaluated at each point. This data was imported into MATLAB and defined as a custom pressure source at  $z = 0$  in the HITU simulator code.

The accuracy of this method was verified by comparing the axial pressure distribution results for a 1 V input to the results from the FEM model. The 3 mm focal length had the greatest error, but these results were still acceptable with 5% lower beamwidth and 2% higher peak amplitude.

#### 5.3.4 CO-REGISTERED HISTOTRIPSY AND IMAGING

After the histotripsy array was characterized, the imaging probe was positioned in the center hole. The tolerance was tight enough that the bubble cloud in water could be seen in the image slice regardless of the position of the imaging array. However, this can be misleading as the bubble cloud in tissue is significantly smaller than the cloud observed in water because the tissue stiffness impedes bubble expansion [140]. So, it is possible for the bubble cloud to be out of the imaging plane when tested in tissue. For this reason, a tissue phantom (2% Agarose, 1.2% SiO<sub>2</sub>) was used as a medium for more accurately co-aligning the two devices. The ablation transducer was held fixed using a clamp, and the imaging array was manually adjusted using a fixture with 3-axis positioning adjustment mounted to a ball socket (to adjust tilt angles). The imaging probe position was adjusted while pulsing the histotripsy array and monitoring the B-mode image, until the full extent of the line appeared equally in the image. The water dish was carefully moved without touching the devices, and superglue was used to permanently fix them together.

Finally, the combined device was tested *in vivo* on an adult male Wistar rat. All procedures were approved by the Dalhousie University Committee on Laboratory Animals (protocol 23-039). The rat was anesthetized with isoflurane and the head was placed in a stereotaxic frame. The scalp was incised and a 10 mm diameter craniectomy was performed, leaving the dura intact. A mound of ultrasound gel was deposited on the dura and the histotripsy/imaging device, mounted on a rigidly held micromanipulator, was positioned over the site. The high-frequency imaging array was used in real time during the experiment to position the histotripsy array treatment zone in the brain, to monitor the bubble cloud formation during treatment, and to visualize the lesion that was produced

after treatment. The array's capability to produce both a single spot ablation and a rapid line ablation were tested. For the line pulse sequence, the array focus was swept from 3 to 8 mm at 0.25 mm steps with 4 pulses per focal point.

After the experiment, the rat was sacrificed, and the brain was fixed. The brain was saturated in 30% sucrose solution and cryo-embedded in frozen sectioning medium. For the region treated with the line pulse sequence, 15  $\mu\text{m}$  thick sections were collected with a cryostat and the sections were stained with hematoxylin and eosin (H&E).

## 5.4 RESULTS

### 5.4.1 LOW VOLTAGE CHARACTERIZATION

The electrical impedance of array elements 5 through 15 were very well grouped together and matched well with simulations. Elements 4 through 1 exhibited a progressively higher impedance magnitude, as expected due to the decreasing element area, while element 16 appeared slightly damped, likely due to damage from laser cutting the array outline. The impedance curves are shown in Figure 5.7. The measured thickness mode electromechanical coupling coefficient of the composite before array fabrication was 0.64. This was slightly reduced to 0.59 after array fabrication. The mean resonance frequency of the array was 5.4 MHz, with the impedance magnitude and phase at this frequency measuring 135  $\Omega$  and  $-37.6^\circ$ , respectively. After adding the 470 pF tuning capacitors, the mean impedance magnitude and phase was 55  $\Omega$  and  $-77.7^\circ$ , respectively.

The measured transmit sensitivity for the array focussed to 3 mm though 8 mm and the lens focussed transducer, are shown in Figure 5.8, with error bars indicating the  $\pm 17\%$  uncertainty of the hydrophone sensitivity. These are compared with the simulated sensitivity from the FEM model. The measured sensitivity matches closely with simulated values from the FEM model for most of the range of array foci tested. The measured data diverges from simulated data as the f-numbers in decreased, illustrated by the 3 mm focus in this case. The sensitivity of the lens focussed transducer was higher than expected but the simulation was still just within the error bars.

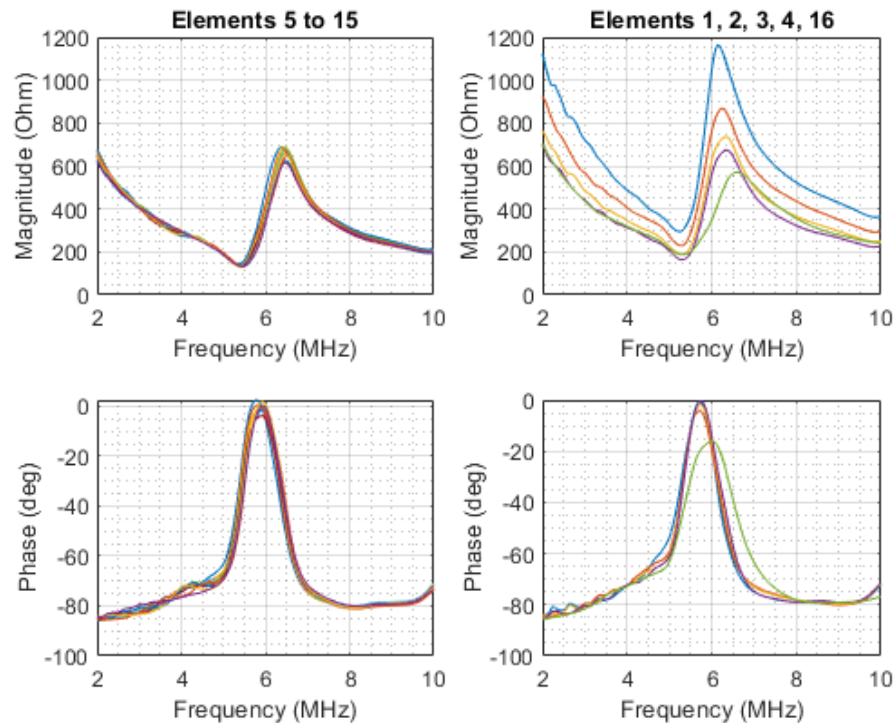


Figure 5.7: Measured electrical impedance magnitude and phase of each array element. The column on the left shows elements 5 through 15 separately to highlight the excellent grouping observed between array elements. The column on the right shows elements 1 through 4, which have reduced area due to the square hole, and element 16, which appeared to be damaged from laser cutting the array outline.

Figure 5.9 shows measured and simulated 2D colormaps of the acoustic pressure field (radiation patterns), for the lens focussed transducer and the array focussed to 3 mm, 5 mm, and 7 mm (stitched together). The vertical axis corresponds to the axial direction, with zero indicating the surface of the composite. The horizontal axis corresponds to the radial direction (parallel to the array). The measured radiation patterns are in excellent agreement with the FEM models qualitatively, capturing the shape and relative amplitude of the off-focus pressure very well. The main difference is the slight wobble in the measured data, which is an artifact of instability in the positioning stage used. Metrics from the acoustic field data are shown in Table 5.2, including the actual focal length, axial 3 dB beamwidth and radial 3 dB beamwidth. The actual focal length and axial beamwidth agree very well with simulations (mostly within  $\pm 5\%$ ), while the measured radial beamwidths are all 20 - 60% higher than expected.

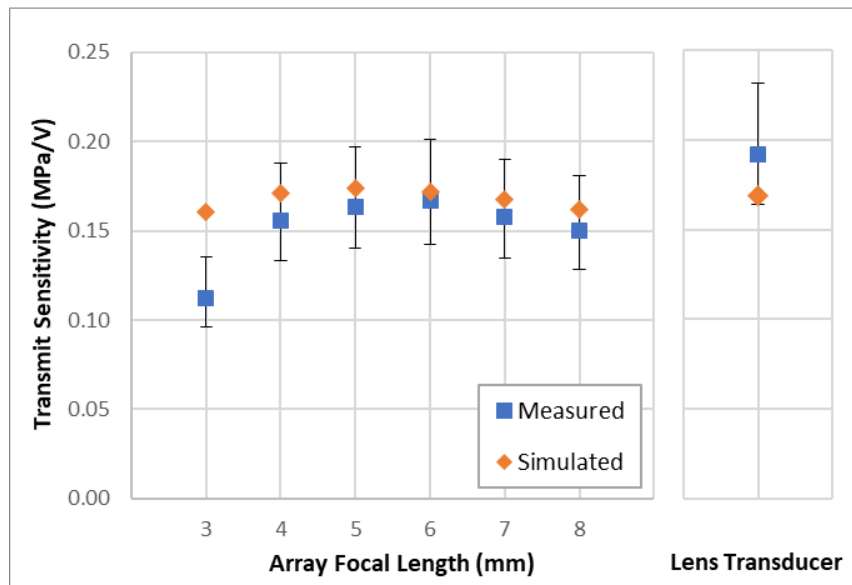


Figure 5.8: Measured transmit sensitivity compared to FEM model results for the array focussed to several foci, and the lens focussed transducer. Error bars on the measured data represent the  $\pm 17\%$  uncertainty of the hydrophone sensitivity.

Table 5.2: Comparison of acoustic field measurements from annular array and lens-based transducer to FEM simulations.

		Lens focussed transducer	Array focussed to:		
			3 mm	5 mm	7 mm
Actual Focal Length (mm)	Measured	6.60	3.12	4.96	6.73
	Simulated	6.75	2.97	4.80	6.59
Axial 3dB Beamwidth (mm)	Measured	1.43	1.07	1.73	2.68
	Simulated	1.48	1.22	1.82	2.77
Radial 3dB Beamwidth (mm)	Measured	0.19	0.17	0.25	0.30
	Simulated	0.16	0.12	0.16	0.22

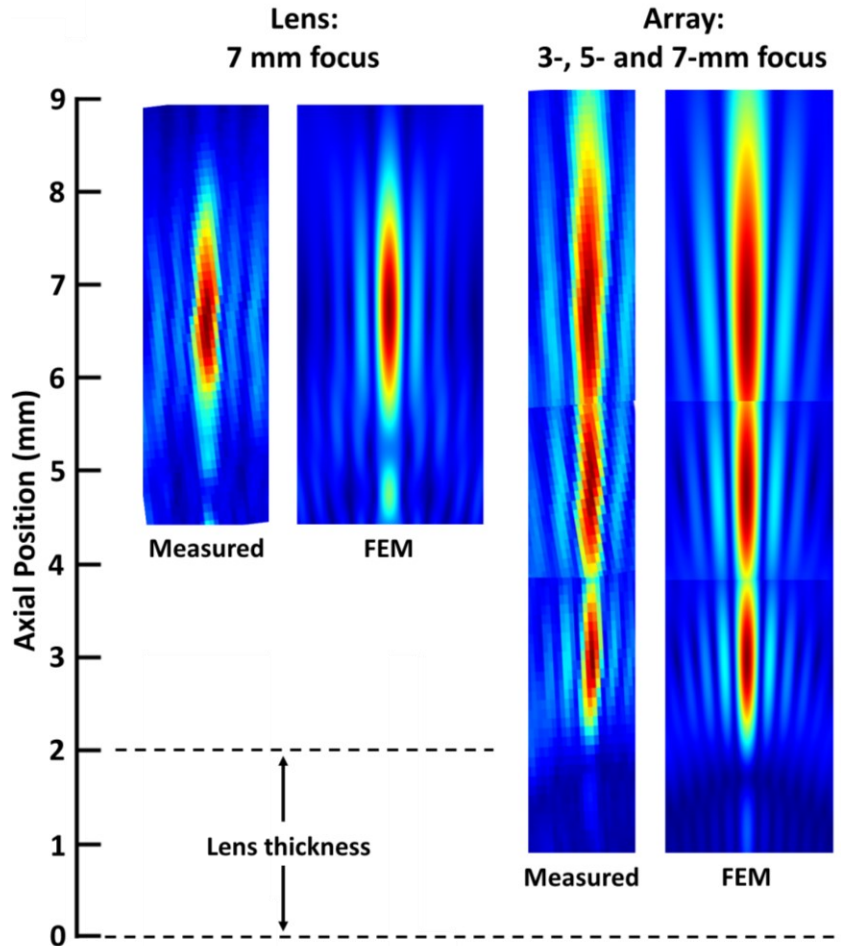


Figure 5.9: Measured and simulated radiation patterns showing the normalized peak focal pressure of the lens focussed transducer compared to the array focussed to 3 mm, 5 mm, and 7 mm. The vertical axis shows the distance from the surface of the composite, with the dashed line illustrating the maximum thickness of the lens.



## 5.4.2 CAVITATION VOLTAGE IN WATER

A measured voltage pulse is shown in Figure 5.10, from a typical array element during operation. Figure 5.11 shows an example data set from the cavitation threshold voltage experiment, for the array focussed to 3 mm in water. Individual data points show the average percentage of pulses that produced cavitation out of 300 pulses (split into three trials) for a given drive voltage. In this case the estimated  $V_{Cav}$  is 254 V<sub>PP</sub>.

The results from the  $V_{Cav}$  experiment are shown in Table 5.3, along with the simulated peak acoustic intensity at the surface, peak acoustic power, and peak focal pressures from the non-linear acoustic simulation. The simulated peak negative pressures at  $V_{Cav}$  for the array focussed to 4 through 7 mm had a mean of -29.0 MPa, with a standard deviation of 0.6 MPa. Considering the hydrophone measurement uncertainty, experimental error in the  $V_{Cav}$  measurement, and simulation inaccuracies, this is an acceptable agreement with the published cavitation threshold of  $-27.4 \text{ MPa} \pm 1.1 \text{ MPa}$ , measured in water at 3 MHz [83]. No publications have reported the cavitation threshold above this, but there was a similar threshold for 1.5- and 3-MHz, so it's assumed the threshold doesn't change much at higher frequencies. The results for the lens transducer, 3 mm focus and 8 mm focus were significantly different than expected and are further examined in the discussion section.

Figure 5.12 shows the pressure waveforms at the focus from the HITU simulations for each array focal length. The source acoustic power used in the model was based on the measured transmit sensitivities scaled by the measured cavitation voltage.

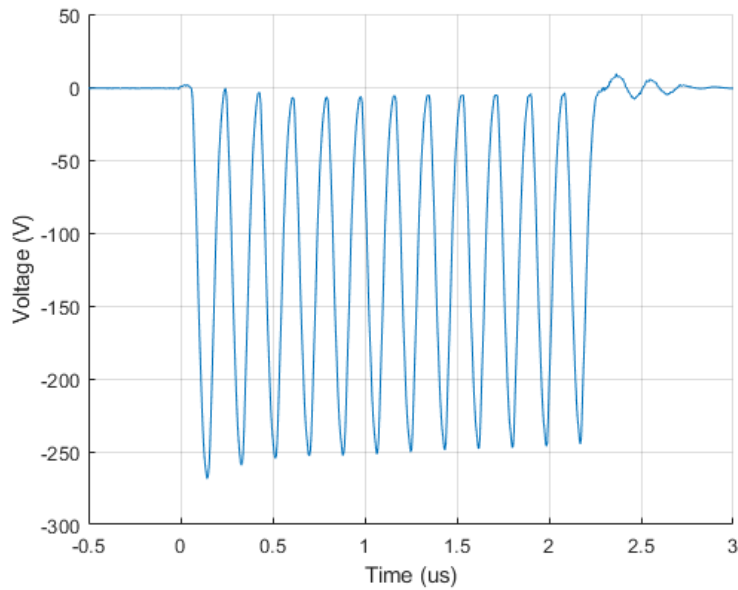


Figure 5.10: A typical 5.4-MHz 12-cycle voltage pulse probed across the tuning capacitors at the end of the cable with the high voltage supply set to 195 V.

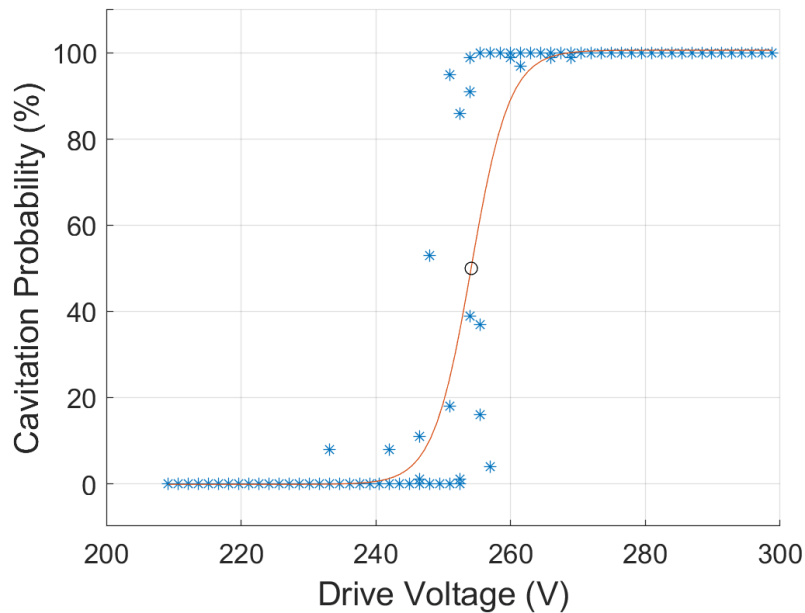


Figure 5.11: An example probability curve from the cavitation threshold voltage measurement in water for the array focused to 3 mm. The asterisks show the average cavitation percentage across three trials of 100 pulses each, for each drive voltage. The red line is a sigmoid curve fit to this data. The circle indicates the estimated cavitation threshold voltage corresponding to a 50 % cavitation probability.

Table 5.3: Cavitation threshold voltages measured in water and the corresponding surface peak acoustic intensity, acoustic power, and focal pressures from non-linear simulations.

	Acoustic Lens	Array focussed to:					
		3 mm	4 mm	5 mm	6 mm	7 mm	8 mm
Measured Cavitation Threshold Voltage ( $V_{pp}$ )	336	254	253	278	325	398	498
Simulated Peak Intensity ( $W/cm^2$ )	1548	290	321	424	631	1015	1675
Simulated Peak Acoustic Power (W)	661	102	112	149	221	356	587
Simulated Peak $P_{NEG}$ (MPa)	-32.2	-24.0	-28.2	-28.7	-29.4	-29.7	-30.8
Simulated Peak $P_{POS}$ (MPa)	150.7	41.8	100.0	154.4	150.7	146.8	141.3

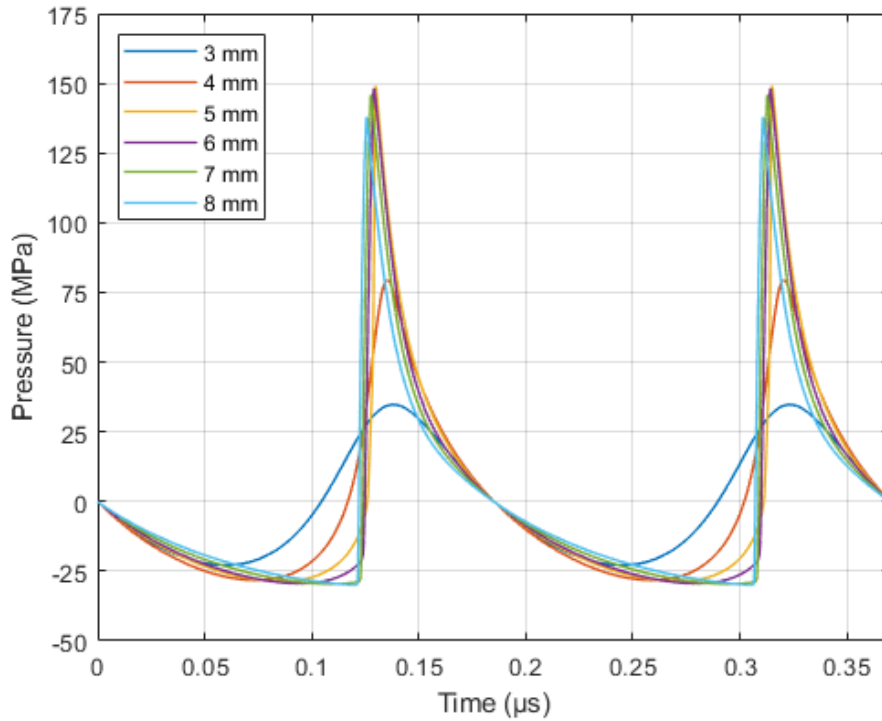


Figure 5.12. Simulated non-linear focal pressure waveforms at the array focus, using the measured transmit sensitivity (linear focal pressure per volt) and driving voltages corresponding to the cavitation threshold voltages given in Table 5.3.

### 5.4.3 TISSUE PHANTOM

The image on the left in Figure 5.13 shows the side looking array being tested in water. This image is composed of three separate images of the array producing a bubble cloud at 3-, 5-, and 7-mm focal lengths.

The image on the right in Figure 5.13 is composed of 4 different B-mode images captured while testing the histotripsy array in the tissue phantom. The array was focussed to 3 mm, 5 mm, 7 mm, and then swept through the 3 to 8 mm line pulse sequence described in the methods section. A pulse voltage of 360 V<sub>PP</sub> was used for each.

For the line sweep, the Doppler overlay was frame averaged to show the full extent of the treatment in a single image. Comparing the single focal points, the bubble cloud size decreased as the focal length was increased. This was expected due to the acoustic waves transmitting farther into the phantom meaning increased losses and more significant non-linear effects resulting in a lower peak negative focal pressure.

By comparison the bubble cloud of the “line” appears to have a more uniform width than the individual points. This seems to suggest that by sweeping in a line with overlapping foci, the farther away focal points build off the previous bubble cloud from the inner focal point.

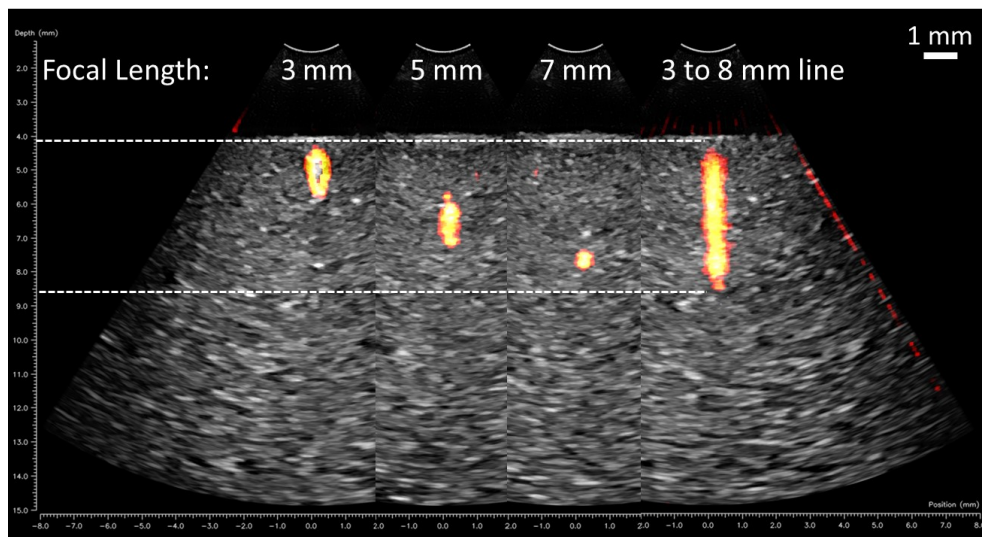
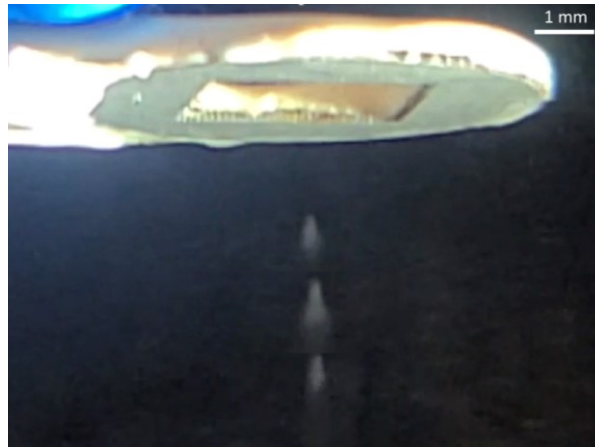


Figure 5.13: (Top) Image of the side looking array operating in water with a bubble cloud visible at 3-, 5- and 7-mm focal lengths, composed of separate images for each focal point. (Bottom) Four B-mode images captured during the tissue phantom test, from 3 individual focal lengths and the line pulse sequence. The Doppler signal was overlaid to show the bubble cloud.

#### 5.4.4 IN VIVO RAT BRAIN

The array was able to successfully produce both a single spot ablation with the array focussed to 3 mm, and a 4 mm long line ablation in the rat brain by sweeping the focus axially from 3 - 8 mm. The “line” ablation example that is shown in Figure 5.14 was created by treating for 18 seconds using a 370 V<sub>PP</sub>, 5.4 MHz, 12 cycle, 1 kHz PRF pulse sequence. From left to right Figure 5.14 shows the Doppler signal overlaid on the B-mode

image highlighting the bubble cloud during treatment, the line shaped lesion imaged shortly after the treatment, and the histology of the lesion.

Unfortunately, the brain slices were not in the same plane as the lesion, meaning that several tissue slices had to be combined to capture the full extent of the line ablation. Regardless, when stitched together the tissue slices show that the brain tissue was ablated with a uniform width as expected from the tissue phantom measurements.

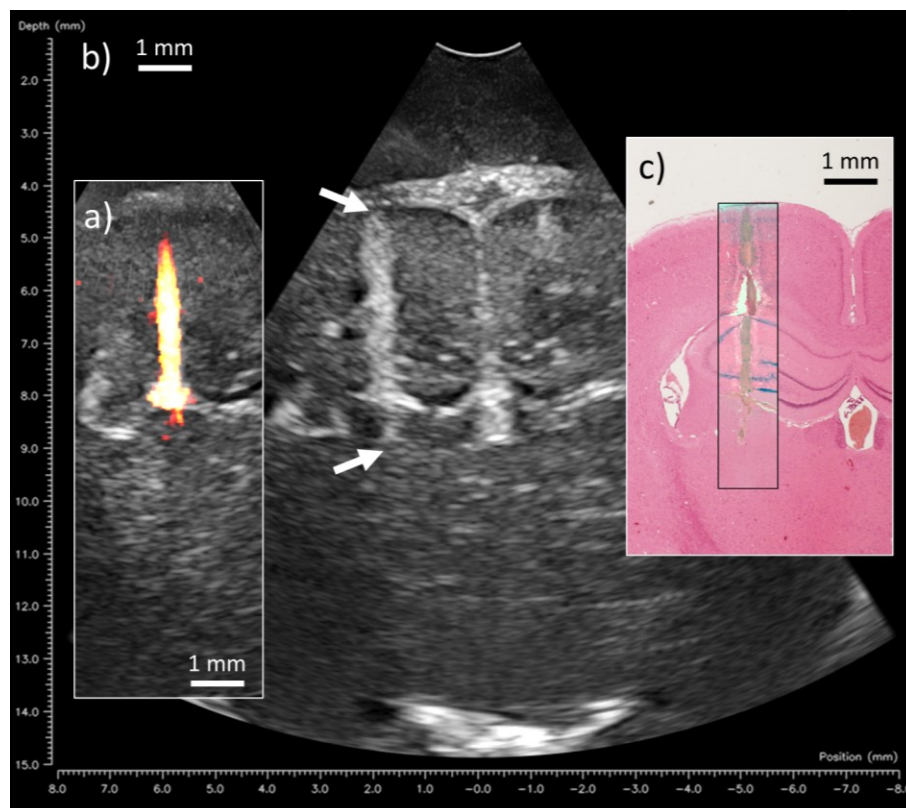


Figure 5.14: *In vivo* rat brain ablation experiment results. (a) B-mode image during ablation with doppler overlay showing bubble cloud. (b) B-mode image of the ablated line after treatment, the endpoints of the line are indicated by the arrows. (c) Composite image of several tissue slices overlaid to show the full extent of the ablated line. The black rectangle highlights the region of interest.

## 5.5 DISCUSSION

This study demonstrated the feasibility of a miniaturized annular histotripsy array with co-registered imaging. Overall, the measured results matched simulations remarkably well, with some exceptions.

The mismatch between measurement and simulation for the 3 mm focal length transmit sensitivity is likely due to the array elements having an increased effective width in reality because of the piezoelectric composite pillars overlapping into the neighboring elements. This would cause a reduced focal pressure for focal lengths closer to the array due to the elements having a narrower directivity, which has a significant impact on the pressure contributed by the outer elements. This effect is not captured in the FEM model, as it uses a homogeneous substrate material.

The thickest part of the lens is 1.9 mm from the bottom of its curvature, and the actual focal length was 6.6 mm. This means that its maximum operational depth is only 4.7 mm. Interestingly, despite the lens-focussed transducer operating at a higher frequency than the array (6.5 MHz vs 5.4 MHz), the lens focus is comparable to the array focus for a focal length that falls somewhere between 4 and 5 mm, which is a comparable operational depth.

The measured radiation pattern of the lens-based transducer showed a significant pre-focal pressure zone that was also observed in the FEM model. This off focus pressure buildup appears to be due to a vibrational mode in the width dimension of the lens, observed in the FEM modeling. The measured peak pressure in this region was about 50% of the peak focal pressure, which could lead to unintended pre-focal cavitation during treatment. This was not observed in the array radiation patterns, which should be noted as

another advantage of focussing using a planar annular array instead of an acoustic lens in this application.

The discrepancy between the simulated and expected non-linear focal pressure for the lens transducer data likely stems from an overestimated measured sensitivity. If the sensitivity predicted by the FEM model is used instead, the simulated minimum and maximum focal pressure is -29.6 MPa and 150.2 MPa, respectively, much closer to that of the array for the same focal length.

The reason for the approximately linear decrease in peak negative pressure as the focal length is increased from 4 to 8 mm is unclear, however the peak positive pressure also decreases linearly as the focal length is increased from 5 to 8 mm, which might explain the change. However, it could simply be due to experimental error or an artifact of the simulation, as the opposite trend was expected for shock scattering cavitation due to a wider focal region at higher f-numbers. The array was tested from the 3 mm focus to the 8 mm focus in order, with the maximum drive voltage set to the minimum value necessary to capture the probability curve ( $\sim 50$  V above the  $V_{Cav}$  for each). The array output pressure dropped slightly after testing the 7 mm focal length. This was confirmed by re-measuring the previous cavitation thresholds. This means the measured  $V_{Cav}$  for the 8 mm focus is likely higher than it should be, which would explain the higher-than-expected peak negative pressure. The third order approximation for the diffraction operator was used in the HITU simulator code, which is only accurate to a minimum f-number of 0.5 (propagation angle  $\theta \leq 45\%$ ) [99]. The 3 mm focal length violates this, which might explain the lower-than-expected focal pressure.



A tissue phantom made with a 2% Agarose, 1.2% SiO<sub>2</sub> concentration was used due to availability at the time of testing. A phantom made with 1% agarose concentration is expected to be more representative of brain tissue, as the cavitation threshold matches that of fat for a 1 kHz PRF [140], and the *in vivo* Young's modulus of brain tissue is very similar to fat [141]. It would be useful to have a phantom that had the same cavitation threshold and bubble cloud size as brain tissue, however this was outside the scope of the study and would require evaluation of the device in several different phantom compositions.

A single array was used for all the transmit sensitivity, acoustic field, and cavitation threshold voltage measurements. Unfortunately, several array elements failed during the cavitation threshold test when the array was focussed to 7 mm and driven to 450 V<sub>pp</sub>. A different array (made using the same design and materials) was used for the tissue phantom and *in vivo* experiment. This device wasn't fully characterized but was briefly tested in water. A pulse voltage of ~360 V<sub>pp</sub> was required to produce a bubble cloud over the full 3 mm to 8 mm range. This suggests that the array had a higher output pressure than the one used for characterisation experiments.

In the B-mode image, the treated region gradually showed up as hyperechoic post-ablation, over a span of about 10 - 20 seconds. Based on results from previous *in vivo* ablation experiments using a similar device [18], this is believed to be due to blood filling the cavity and coagulating. In that study, histological analysis (performed by an experienced histopathologist) of some ablated regions was found to contain coarsely mixed purple and red colored areas, believed to be homogenized brain tissue and blood respectively. One brain was paraffin embedded and sectioned at 5 μm, which showed intact red blood cells in the red colored regions.

In future work, the device performance should be evaluated in detail through more rigorous *in vivo* testing. Better understanding the ablation size for the individual foci, and for the line sweep would be a necessary next step in order to eventually use this device clinically. The study should also investigate the effect of changing various pulse settings such as number of cycles, frequency and PRF, as well as line sweep settings, including number of pulses per focal point and spacing between focal points. Results from future rodent studies involving post-ablation recovery will be used to assess the safety of applying such high acoustic pressures in the brain.

While this device was designed with brain tumor resection in mind, the initial *in vivo* results show that it could also be extremely useful for preclinical rodent experiments. The existing device would work well for mice experiments; for rat experiments a larger diameter therapy array could be used to increase the maximum focal length, enabling treatment in any location in the brain.

## 5.6 CONCLUSION

In this study we presented a new design for an 8 mm diameter, image-guided, annular array focussed histotripsy transducer. This design has several advantages over the previously published lens-focussed design including a flat aperture and an axially steerable focus. To allow for a direct comparison an 8 mm diameter aluminum lens-focussed transducer was fabricated and tested along with the array. FEM models were used to select the number of array elements and to provide a comparison for low voltage characterization of the array and lens-focussed transducer. Several arrays were fabricated using a PZT-5H composite material, in both a forward- and side-looking form factor. For a range of focal

lengths, the transmit sensitivity and acoustic field was measured at low voltages, then the cavitation threshold voltage in water was determined.

Low voltage measurements matched simulations well, with only the 3 mm array focus in disagreement, which could be due to modelling the composite as a homogeneous material. The lens transducer had slightly higher sensitivity than the array, but the difference was within hydrophone uncertainty. The measured sensitivity and cavitation thresholds were used to estimate the focal pressure at cavitation using HITU simulator, yielding peak negative pressures that were close to the published threshold in water, with explanations provided for the data points that disagreed with theory. The cavitation threshold measurements in water indicated that the array outperformed the lens-focused transducer for a comparable operating depth. Finally, the array was tested in a tissue phantom and an *in vivo* rat brain. The histotripsy array was used to produce an elongated lesion in the brain by rapidly steering the focus axially from 3 - 8 mm. Real time ultrasound B-mode and Doppler imaging was used to target the tissue and monitor ablation progress. Histology confirmed the targeted tissue was fully homogenized.

We believe this work represents a significant advancement in endoscopic image-guided histotripsy technology and could eventually be applied to existing neurosurgical workflows to improve resection precision, potentially improving patient outcomes.

## **CHAPTER 6:**

### **CONCLUSION**

This thesis outlines work completed toward further miniaturization of ultrasound image-guided histotripsy devices, beyond the 10 mm diameter transducer previously published. The initial assumption was that incorporating the imaging array in front of the therapy transducer was the best approach to minimize the active aperture.

The first study, presented in Chapter 3, explored adding a lower frequency pump transducer behind the main transducer, increasing the focal pressure to help offset the loss from transmitting through an imaging array placed in front. The dual frequency concept was able to reduce the cavitation threshold without increasing the active aperture size. The efficacy of the pump transducer on lowering the pressure required by the main therapy transducer was greater than expected based on a linear combination of low voltage focal pressures. This highlights the advantage of using a lower frequency pump transducer for reducing frequency dependent losses, while benefiting from the small ablation size from a higher frequency transducer.

A follow-up experiment after this study made it clear that there would be a substantial loss in pressure, and significant fabrication challenges involved with incorporating the imaging array into the stacked design. While a 5 x 5 mm square device was small compared to previous histotripsy transducers, the largest dimension was still about 7 mm not including the case and imaging array interconnects. FEM simulations suggested that the

outer envelope of this stack design would be larger than that of a lens-focused transducer surrounding the 4 x 4 mm imaging probe. For this reason, it was decided to move away from the stacked design. However, that approach would still be valuable for transducers without integrated ultrasound-guidance such as IVUS (intravenous ultrasound) transducers.

The study in Chapter 4 explores finding piezoelectric materials that can produce higher focal pressure compared to the previously used material. Five piezoelectric ceramics were evaluated by fabricating 1-3 piezo/epoxy composite materials and building them into 8 mm diameter lens-focused transducers. In general, the low voltage characteristics agreed with simulations, with the exception of the sensitivity of the PMN-38 transducers. Materials with higher clamped dielectric constant had higher transmit sensitivity and lower cavitation threshold voltage. The non-linear extrapolation of measurements using HITU simulator yielded the anticipated peak negative pressures at cavitation, which were similar to the published values for free-field cavitation in water. PMN-38 and Pz39 were the most sensitive materials, but both consistently failed. PMN-38 failures were attributed to the higher current, while the porous structure of Pz39 is thought to be the cause of its failures. Pz54 and PZT-5H (CTS 3203HD) transducers performed similarly, with the latter having better performance during the saturation experiment and a slightly higher sensitivity and lower cavitation threshold voltage.

Finally, in Chapter 5, a new approach of using a 16-element annular array instead of the acoustic lens was explored for an 8 mm diameter, image-guided histotripsy transducer. The therapy array performance was compared to an aluminum lens-based device. Overall, measurements agreed very well with simulations, with only the closest array focal point

diverging from expected results. This is thought to be due to modelling the composite as a homogeneous material, when in reality the individual pillars overlap multiple elements. Based on cavitation threshold measurements in water, for a comparable operating depth, the array outperformed the lens-focused transducer. The histotripsy array was used to produce an elongated lesion in vivo in a rat brain by rapidly steering the focus axially from 3 – 8 mm. Real time ultrasound B-mode and Doppler imaging was used to target the tissue and monitor ablation progress. Histology confirmed the targeted tissue was fully homogenized.

As a whole, this body of work is believed to represent a significant advancement in endoscopic image-guided histotripsy technology. Hopefully, it will help permit the application of histotripsy to more minimally invasive procedures, including the resection of brain tumors. This could allow surgeons more control and precision when treating difficult to resect tumors such as glioblastoma, potentially improving patient outcomes.

## 6.1 FUTURE WORK

The dual frequency design should be revisited to better optimize the frequency and layer thickness selection. The two frequencies and layer thickness could be chosen so that the transmission coefficient is a minimum for the high frequency, and a maximum for the low frequency. This would allow a much higher-pressure output from the pump transducer.

Based on simulations, increasing the volume fraction of the composite material can significantly increase the output pressure from both the lens-focused and annular array transducers. This was not investigated, because only the 45% volume fraction composite was available at the time. For Chapter 4, which involved composite fabrication, the same

volume fraction was used because there was previous experience with the performance of that design, and it is more challenging to fabricate higher volume fraction composite. The optimal volume fraction was found through KLM modelling to be about 85%, but the available dicing saw blade would limit it to about 75%. This should be investigated as a way to improve the pressure output of these devices.

More in depth *in vivo* experiments should be performed using the array-based histotripsy transducer. The test described in Chapter 5 was relatively brief and intended as a proof of concept. It would be valuable to perform statistical testing on the lesions produced by individual focal points, as well as lines of varying length. A better understanding of this will be critical to treatment planning based on the ultrasound image, ensuring that the ablation is contained to only the intended region and can produce repeatable results. As part of this work, the pulse parameters should also be optimized, such as the PRF, focal point spacing and dwell time.

The plan for eventual clinical adoption of this ultrasound-guided histotripsy device involves a study on the efficacy of this transducer at ablating implanted tumors in mice, a pivotal longitudinal study on tumor removal in dogs (which are commonly diagnosed with glioblastoma) in collaboration with Dr. Eli Vlaisavljevich at Virginia Tech, and assuming these studies are successful, clinical testing in humans.

## BIBLIOGRAPHY

- [1] A. St. John, I. Caturegli, N. S. Kubicki, and S. M. Kavic, “The Rise of Minimally Invasive Surgery: 16 Year Analysis of the Progressive Replacement of Open Surgery with Laparoscopy,” *JSLs*, vol. 24, no. 4, p. e2020.00076, 2020, doi: 10.4293/JSLs.2020.00076.
- [2] C. Tsui, R. Klein, and M. Garabrant, “Minimally invasive surgery: national trends in adoption and future directions for hospital strategy,” *Surg Endosc*, vol. 27, no. 7, pp. 2253–2257, Jul. 2013, doi: 10.1007/s00464-013-2973-9.
- [3] R. Reisch, A. Stadie, R. A. Kockro, and N. Hopf, “The Keyhole Concept in Neurosurgery,” *World Neurosurgery*, vol. 79, no. 2, p. S17.e9-S17.e13, Feb. 2013, doi: 10.1016/j.wneu.2012.02.024.
- [4] Q. Lan *et al.*, “Microsurgical experience with keyhole operations on intracranial aneurysms,” *Surgical Neurology*, vol. 66, pp. S2–S9, Sep. 2006, doi: 10.1016/j.surneu.2006.06.039.
- [5] B. Badie, N. Brooks, and M. M. Souweidane, “Endoscopic and Minimally Invasive Microsurgical Approaches for Treating Brain Tumor Patients,” *J Neurooncol*, vol. 69, no. 1–3, pp. 209–219, Aug. 2004, doi: 10.1023/B:NEON.0000041884.93566.fb.
- [6] I. J. Gerard, M. Kersten-Oertel, J. A. Hall, D. Sirhan, and D. L. Collins, “Brain Shift in Neuronavigation of Brain Tumors: An Updated Review of Intra-Operative Ultrasound Applications,” *Front. Oncol.*, vol. 10, p. 618837, Feb. 2021, doi: 10.3389/fonc.2020.618837.
- [7] K.-W. Huang, P.-H. Lee, T. Kusano, I. Reccia, K. Jayant, and N. Habib, “Impact of cavitron ultrasonic surgical aspirator (CUSA) and bipolar radiofrequency device (Habib-4X) based hepatectomy for hepatocellular carcinoma on tumour recurrence and disease-free survival,” *Oncotarget*, vol. 8, no. 55, pp. 93644–93654, Nov. 2017, doi: 10.18632/oncotarget.21271.
- [8] M. Lacroix *et al.*, “A multivariate analysis of 416 patients with glioblastoma multiforme: prognosis, extent of resection, and survival,” *Journal of Neurosurgery*, vol. 95, no. 2, pp. 190–198, Aug. 2001, doi: 10.3171/jns.2001.95.2.0190.
- [9] K. L. Chaichana *et al.*, “Establishing percent resection and residual volume thresholds affecting survival and recurrence for patients with newly diagnosed intracranial glioblastoma,” *Neuro-Oncology*, vol. 16, no. 1, pp. 113–122, Jan. 2014, doi: 10.1093/neuonc/not137.
- [10] P. Shetty, U. Yeole, V. Singh, and A. Moiyadi, “Navigated ultrasound-based image guidance during resection of gliomas: practical utility in intraoperative decision-making and outcomes,” *Neurosurgical Focus*, vol. 50, no. 1, p. E14, Jan. 2021, doi: 10.3171/2020.10.FOCUS20550.



- [11] E. D. Bander, R. Magge, and R. Ramakrishna, “Advances in Glioblastoma Operative Techniques,” *World Neurosurgery*, vol. 116, pp. 529–538, Aug. 2018, doi: 10.1016/j.wneu.2018.04.023.
- [12] A. Claes, A. J. Idema, and P. Wesseling, “Diffuse glioma growth: a guerilla war,” *Acta Neuropathol*, vol. 114, no. 5, pp. 443–458, Nov. 2007, doi: 10.1007/s00401-007-0293-7.
- [13] P. D. Delgado-López and E. M. Corrales-García, “Survival in glioblastoma: a review on the impact of treatment modalities,” *Clin Transl Oncol*, vol. 18, no. 11, pp. 1062–1071, Nov. 2016, doi: 10.1007/s12094-016-1497-x.
- [14] Z. Xu, T. L. Hall, E. Vlasisavljevich, and F. T. Lee, “Histotripsy: the first noninvasive, non-ionizing, non-thermal ablation technique based on ultrasound,” *International Journal of Hyperthermia*, vol. 38, no. 1, pp. 561–575, Jan. 2021, doi: 10.1080/02656736.2021.1905189.
- [15] Z. Xu *et al.*, “Controlled ultrasound tissue erosion,” *IEEE Transactions on Ultrasonics, Ferroelectrics, and Frequency Control*, vol. 51, no. 6, pp. 726–736, Jun. 2004, doi: 10.1109/TUFFC.2004.1304271.
- [16] Z. Xu, J. B. Fowlkes, A. Ludomirsky, and C. A. Cain, “Investigation of intensity thresholds for ultrasound tissue erosion,” *Ultrasound Med Biol*, vol. 31, no. 12, pp. 1673–1682, Dec. 2005, doi: 10.1016/j.ultrasmedbio.2005.07.016.
- [17] W. W. Roberts, T. L. Hall, K. Ives, J. S. Wolf, J. B. Fowlkes, and C. A. Cain, “Pulsed Cavitation Ultrasound: A Noninvasive Technology for Controlled Tissue Ablation (Histotripsy) in the Rabbit Kidney,” *Journal of Urology*, vol. 175, no. 2, pp. 734–738, Feb. 2006, doi: 10.1016/S0022-5347(05)00141-2.
- [18] T. G. Landry *et al.*, “Endoscopic Coregistered Ultrasound Imaging and Precision Histotripsy: Initial *In Vivo* Evaluation,” *BME Frontiers*, vol. 2022, pp. 1–14, Jul. 2022, doi: 10.34133/2022/9794321.
- [19] A. Hendricks-Wenger, R. Hutchison, E. Vlasisavljevich, and I. C. Allen, “Immunological Effects of Histotripsy for Cancer Therapy,” *Front. Oncol.*, vol. 11, p. 681629, May 2021, doi: 10.3389/fonc.2021.681629.
- [20] J. Vidal-Jove, X. Serres-Creixams, T. J. Ziemlewicz, and J. M. Cannata, “Liver Histotripsy Mediated Abscopal Effect—Case Report,” *IEEE Trans. Ultrason., Ferroelect., Freq. Contr.*, vol. 68, no. 9, pp. 3001–3005, Sep. 2021, doi: 10.1109/TUFFC.2021.3100267.
- [21] A. D. Maxwell *et al.*, “Cavitation clouds created by shock scattering from bubbles during histotripsy,” *The Journal of the Acoustical Society of America*, vol. 130, no. 4, pp. 1888–1898, Oct. 2011, doi: 10.1121/1.3625239.

- [22] K.-W. Lin *et al.*, “Histotripsy beyond the intrinsic cavitation threshold using very short ultrasound pulses: microtripsy.,” vol. 61, no. 2, 2014.
- [23] N. R. Styn, J. C. Wheat, T. L. Hall, and W. W. Roberts, “Histotripsy of VX-2 Tumor Implanted in a Renal Rabbit Model,” *Journal of Endourology*, vol. 24, no. 7, pp. 1145–1150, Jul. 2010, doi: 10.1089/end.2010.0123.
- [24] E. Vlasisavljevich, “Investigations of the Cavitation and Damage Thresholds of Histotripsy and Applications in Targeted Tissue Ablation”.
- [25] E. Vlasisavljevich *et al.*, “Image-Guided Non-Invasive Ultrasound Liver Ablation Using Histotripsy: Feasibility Study in an In Vivo Porcine Model,” *Ultrasound in Medicine & Biology*, vol. 39, no. 8, pp. 1398–1409, Aug. 2013, doi: 10.1016/j.ultrasmedbio.2013.02.005.
- [26] E. Vlasisavljevich *et al.*, “Non-Invasive Ultrasound Liver Ablation Using Histotripsy: Chronic Study in an In Vivo Rodent Model,” *Ultrasound in Medicine & Biology*, vol. 42, no. 8, pp. 1890–1902, Aug. 2016, doi: 10.1016/j.ultrasmedbio.2016.03.018.
- [27] J. E. Lundt, S. P. Allen, J. Shi, T. L. Hall, C. A. Cain, and Z. Xu, “Non-invasive, Rapid Ablation of Tissue Volume Using Histotripsy,” *Ultrasound in Medicine & Biology*, vol. 43, no. 12, pp. 2834–2847, Dec. 2017, doi: 10.1016/j.ultrasmedbio.2017.08.006.
- [28] T. D. Khokhlova *et al.*, “Pilot in vivo studies on transcutaneous boiling histotripsy in porcine liver and kidney,” *Sci Rep*, vol. 9, no. 1, p. 20176, Dec. 2019, doi: 10.1038/s41598-019-56658-7.
- [29] T. G. Schuster, J. T. Wei, K. Hendlin, R. Jahnke, and W. W. Roberts, “Histotripsy Treatment of Benign Prostatic Enlargement Using the Vortx R x System: Initial Human Safety and Efficacy Outcomes,” *Urology*, vol. 114, pp. 184–187, Apr. 2018, doi: 10.1016/j.urology.2017.12.033.
- [30] D. Coluccia, J. Fandino, L. Schwyzer, E. Martin, and B. Werner, “First noninvasive thermal ablation of a brain tumor with MR-guided focused ultrasound,” 2014.
- [31] N. Lu *et al.*, “Transcranial Magnetic Resonance-Guided Histotripsy for Brain Surgery: Pre-clinical Investigation,” *Ultrasound in Medicine & Biology*, vol. 48, no. 1, pp. 98–110, Jan. 2022, doi: 10.1016/j.ultrasmedbio.2021.09.008.
- [32] L. Dixon, A. Lim, M. Grech-Sollars, D. Nandi, and S. Camp, “Intraoperative ultrasound in brain tumor surgery: A review and implementation guide,” *Neurosurg Rev*, vol. 45, no. 4, pp. 2503–2515, Aug. 2022, doi: 10.1007/s10143-022-01778-4.
- [33] S. Mahboob *et al.*, “Intraoperative Ultrasound-Guided Resection of Gliomas: A Meta-Analysis and Review of the Literature,” *World Neurosurgery*, vol. 92, pp. 255–263, Aug. 2016, doi: 10.1016/j.wneu.2016.05.007.

- [34] L. B. Nabors *et al.*, “Central Nervous System Cancers, Version 3.2020, NCCN Clinical Practice Guidelines in Oncology,” *Journal of the National Comprehensive Cancer Network*, vol. 18, no. 11, pp. 1537–1570, Nov. 2020, doi: 10.6004/jnccn.2020.0052.
- [35] T. J. Brown *et al.*, “Association of the Extent of Resection With Survival in Glioblastoma: A Systematic Review and Meta-analysis,” *JAMA Oncol*, vol. 2, no. 11, p. 1460, Nov. 2016, doi: 10.1001/jamaoncol.2016.1373.
- [36] Y. M. Li, D. Suki, K. Hess, and R. Sawaya, “The influence of maximum safe resection of glioblastoma on survival in 1229 patients: Can we do better than gross-total resection?,” *JNS*, vol. 124, no. 4, pp. 977–988, Apr. 2016, doi: 10.3171/2015.5.JNS142087.
- [37] D. Kondziolka, S. M. Shin, A. Brunswick, I. Kim, and J. S. Silverman, “The biology of radiosurgery and its clinical applications for brain tumors,” *Neuro-Oncology*, vol. 17, no. 1, pp. 29–44, Jan. 2015, doi: 10.1093/neuonc/nou284.
- [38] B. Lippitz, C. Lindquist, I. Paddick, D. Peterson, K. O’Neill, and R. Beaney, “Stereotactic radiosurgery in the treatment of brain metastases: The current evidence,” *Cancer Treatment Reviews*, vol. 40, no. 1, pp. 48–59, Feb. 2014, doi: 10.1016/j.ctrv.2013.05.002.
- [39] A. H. Shah and J. D. Heiss, “Neurosurgical Clinical Trials for Glioblastoma: Current and Future Directions,” *Brain Sciences*, vol. 12, no. 6, p. 787, Jun. 2022, doi: 10.3390/brainsci12060787.
- [40] H. A. Fadel *et al.*, “Laser Interstitial Thermal Therapy for First-Line Treatment of Surgically Accessible Recurrent Glioblastoma: Outcomes Compared With a Surgical Cohort,” *Neurosurgery*, vol. 91, no. 5, pp. 701–709, Nov. 2022, doi: 10.1227/neu.0000000000002093.
- [41] N. McDannold, G. T. Clement, P. Black, F. Jolesz, and K. Hynynen, “Transcranial Magnetic Resonance Imaging– Guided Focused Ultrasound Surgery of Brain Tumors: Initial Findings in 3 Patients,” *Neurosurgery*, vol. 66, no. 2, pp. 323–332, Feb. 2010, doi: 10.1227/01.NEU.0000360379.95800.2F.
- [42] Z. Izadifar, Z. Izadifar, D. Chapman, and P. Babyn, “An Introduction to High Intensity Focused Ultrasound: Systematic Review on Principles, Devices, and Clinical Applications,” *JCM*, vol. 9, no. 2, p. 460, Feb. 2020, doi: 10.3390/jcm9020460.
- [43] L. di Biase, E. Falato, and V. Di Lazzaro, “Transcranial Focused Ultrasound (tFUS) and Transcranial Unfocused Ultrasound (tUS) Neuromodulation: From Theoretical Principles to Stimulation Practices,” *Frontiers in Neurology*, vol. 10, 2019, Accessed: Jan. 05, 2024. [Online]. Available: <https://www.frontiersin.org/articles/10.3389/fneur.2019.00549>

- [44] L. Lamsam, E. Johnson, I. D. Connolly, M. Wintermark, and M. H. Gephart, “A review of potential applications of MR-guided focused ultrasound for targeting brain tumor therapy,” *Neurosurgical Focus*, vol. 44, no. 2, p. E10, Feb. 2018, doi: 10.3171/2017.11.FOCUS17620.
- [45] R. C. Miner, “Image-Guided Neurosurgery,” *Journal of Medical Imaging and Radiation Sciences*, vol. 48, no. 4, pp. 328–335, Dec. 2017, doi: 10.1016/j.jmir.2017.06.005.
- [46] O. Solheim, T. Selbekk, A. S. Jakola, and G. Unsgård, “Ultrasound-guided operations in unselected high-grade gliomas—overall results, impact of image quality and patient selection,” *Acta Neurochir*, vol. 152, no. 11, pp. 1873–1886, Nov. 2010, doi: 10.1007/s00701-010-0731-5.
- [47] K. Bingmer, A. Ofshteyn, S. L. Stein, J. M. Marks, and E. Steinhagen, “Decline of open surgical experience for general surgery residents,” *Surg Endosc*, vol. 34, no. 2, pp. 967–972, Feb. 2020, doi: 10.1007/s00464-019-06881-0.
- [48] V. Sun and Y. Fong, “Minimally Invasive Cancer Surgery: Indications and Outcomes,” *Seminars in Oncology Nursing*, vol. 33, no. 1, pp. 23–36, Feb. 2017, doi: 10.1016/j.soncn.2016.11.003.
- [49] M. Fujishiro, “Endoscopic submucosal dissection for stomach neoplasms,” p. 5.
- [50] H. Ono, “Endoscopic mucosal resection for treatment of early gastric cancer,” *Gut*, vol. 48, no. 2, pp. 225–229, Feb. 2001, doi: 10.1136/gut.48.2.225.
- [51] B. Martin-Perez, G. D. Andrade-Ribeiro, L. Hunter, and S. Atallah, “A systematic review of transanal minimally invasive surgery (TAMIS) from 2010 to 2013,” *Tech Coloproctol*, vol. 18, no. 9, pp. 775–788, Sep. 2014, doi: 10.1007/s10151-014-1148-6.
- [52] D. J. Boffa *et al.*, “Minimally Invasive Lung Cancer Surgery Performed by Thoracic Surgeons as Effective as Thoracotomy,” *JCO*, vol. 36, no. 23, pp. 2378–2385, Aug. 2018, doi: 10.1200/JCO.2018.77.8977.
- [53] B. J. Williams *et al.*, “Stereotactic radiosurgery for metastatic brain tumors: a comprehensive review of complications: Clinical article,” *JNS*, vol. 111, no. 3, pp. 439–448, Sep. 2009, doi: 10.3171/2008.11.JNS08984.
- [54] K. F. Chu and D. E. Dupuy, “Thermal ablation of tumours: biological mechanisms and advances in therapy,” *Nat Rev Cancer*, vol. 14, no. 3, pp. 199–208, Mar. 2014, doi: 10.1038/nrc3672.
- [55] J. Jagannathan *et al.*, “Gamma Knife radiosurgery to the surgical cavity following resection of brain metastases: Clinical article,” *JNS*, vol. 111, no. 3, pp. 431–438, Sep. 2009, doi: 10.3171/2008.11.JNS08818.

- [56] M. Tonutti, D. S. Elson, G.-Z. Yang, A. W. Darzi, and M. H. Sodergren, “The role of technology in minimally invasive surgery: state of the art, recent developments and future directions,” *Postgrad Med J*, vol. 93, no. 1097, pp. 159–167, Mar. 2017, doi: 10.1136/postgradmedj-2016-134311.
- [57] W.-J. Lee, “Single port laparoscopic surgery,” *J Korean Med Assoc*, vol. 53, no. 9, pp. 793–806, Sep. 2010, doi: 10.5124/jkma.2010.53.9.793.
- [58] M. Ahmed, C. L. Brace, F. T. Lee, and S. N. Goldberg, “Principles of and Advances in Percutaneous Ablation,” *Radiology*, vol. 258, no. 2, pp. 351–369, Feb. 2011, doi: 10.1148/radiol.10081634.
- [59] M. G. Lubner, C. L. Brace, J. L. Hinshaw, and F. T. Lee, “Microwave Tumor Ablation: Mechanism of Action, Clinical Results, and Devices,” *Journal of Vascular and Interventional Radiology*, vol. 21, no. 8, pp. S192–S203, Aug. 2010, doi: 10.1016/j.jvir.2010.04.007.
- [60] S. Missios, K. Bekelis, and G. H. Barnett, “Renaissance of laser interstitial thermal ablation,” *FOC*, vol. 38, no. 3, p. E13, Mar. 2015, doi: 10.3171/2014.12.FOCUS14762.
- [61] T. Mala, “Cryoablation of liver tumours – a review of mechanisms, techniques and clinical outcome,” *Minimally Invasive Therapy & Allied Technologies*, vol. 15, no. 1, pp. 9–17, Jan. 2006, doi: 10.1080/13645700500468268.
- [62] S. Shiina *et al.*, “A Randomized Controlled Trial of Radiofrequency Ablation With Ethanol Injection for Small Hepatocellular Carcinoma,” *Gastroenterology*, vol. 129, no. 1, pp. 122–130, Jul. 2005, doi: 10.1053/j.gastro.2005.04.009.
- [63] Y. Zhou *et al.*, “Challenges Facing Percutaneous Ablation in the Treatment of Hepatocellular Carcinoma: Extension of Ablation Criteria,” *JHC*, vol. Volume 8, pp. 625–644, Jun. 2021, doi: 10.2147/JHC.S298709.
- [64] N. Jourabchi, K. Beroukhim, B. A. Tafti, S. T. Kee, and E. W. Lee, “Irreversible electroporation (NanoKnife) in cancer treatment,” *Gastrointestinal Intervention*, vol. 3, no. 1, pp. 8–18, Jun. 2014, doi: 10.1016/j.gii.2014.02.002.
- [65] J. H. Rossmeisl *et al.*, “Safety and feasibility of the NanoKnife system for irreversible electroporation ablative treatment of canine spontaneous intracranial gliomas,” *JNS*, vol. 123, no. 4, pp. 1008–1025, Oct. 2015, doi: 10.3171/2014.12.JNS141768.
- [66] “Styker Sonopet.” Accessed: Dec. 13, 2022. [Online]. Available: [<https://www.stryker.com/us/en/nse/products/sonopet-ultrasonic-aspirator.html>](<https://www.stryker.com/us/en/nse/products/sonopet-ultrasonic-aspirator.html>)

- [67] “Integra CUSA.” Accessed: Dec. 13, 2022. [Online]. Available: [https://www.integralife.com/ca/cusa-clarity/category/cusa-tissue-ablation-cusa-clarity](https://www.integralife.com/ca/cusa-clarity/category/cusa-tissue-ablation-cusa-clarity)(https://www.integralife.com/ca/cusa-clarity/category/cusa-tissue-ablation-cusa-clarity)
- [68] “Soring LEVICS.” Accessed: Dec. 13, 2022. [Online]. Available: [https://www.soering.de/en/products/micro-instruments-for-neurosurgery/](https://www.soering.de/en/products/micro-instruments-for-neurosurgery/)(https://www.soering.de/en/products/micro-instruments-for-neurosurgery/)
- [69] F. Ebel, L. Greuter, R. Guzman, and J. Soleman, “Resection of brain lesions with a neuroendoscopic ultrasonic aspirator — a systematic literature review,” *Neurosurg Rev*, vol. 45, no. 5, pp. 3109–3118, Jul. 2022, doi: 10.1007/s10143-022-01837-w.
- [70] “Endoscopic skull base surgery: a comprehensive guide with illustrative cases.”
- [71] F. Epstein, “The Cavitron Ultrasonic Aspirator in Tumor Surgery,” *Neurosurgery*, vol. 31, no. Supplement 1, pp. 497–505, 1984, doi: 10.1093/neurosurgery/31.CN\_suppl\_1.497.
- [72] A. Sanoussi, V. De Blasi, J. S. Azagra, and E. Rosso, “How to perform a minimally invasive hepatic parenchymal transection: a clinical practice review,” *Dig Med Res*, vol. 5, pp. 31–31, Jun. 2022, doi: 10.21037/dmr-22-3.
- [73] S. Maeda and T. Nakamura, “Decalcification of a Heavily Calcified Common Femoral Artery and its Bifurcation with a Cavitron Ultrasonic Surgical Aspirator,” *n/a*, vol. 34, pp. 5–8, Jan. 2017, doi: 10.1016/j.ejvssr.2016.09.003.
- [74] K. Mahmoudi, A. Bouras, D. Bozec, R. Ivkov, and C. Hadjipanayis, “Magnetic hyperthermia therapy for the treatment of glioblastoma: a review of the therapy’s history, efficacy and application in humans,” *International Journal of Hyperthermia*, vol. 34, no. 8, pp. 1316–1328, Nov. 2018, doi: 10.1080/02656736.2018.1430867.
- [75] R. S. Riley and E. S. Day, “Gold nanoparticle-mediated photothermal therapy: applications and opportunities for multimodal cancer treatment,” *WIREs Nanomed Nanobiotechnol*, vol. 9, no. 4, Jul. 2017, doi: 10.1002/wnan.1449.
- [76] K. R. Hogstrom and P. R. Almond, “Review of electron beam therapy physics,” *Phys. Med. Biol.*, vol. 51, no. 13, pp. R455–R489, Jul. 2006, doi: 10.1088/0031-9155/51/13/R25.
- [77] B. Qiu, A. Aili, L. Xue, P. Jiang, and J. Wang, “Advances in Radiobiology of Stereotactic Ablative Radiotherapy,” *Front. Oncol.*, vol. 10, p. 1165, Aug. 2020, doi: 10.3389/fonc.2020.01165.
- [78] M. R. Folkert and R. D. Timmerman, “Stereotactic ablative body radiosurgery (SABR) or Stereotactic body radiation therapy (SBRT),” *Advanced Drug Delivery Reviews*, vol. 109, pp. 3–14, Jan. 2017, doi: 10.1016/j.addr.2016.11.005.

- [79] M. H. Phillips, K. J. Stelzer, T. W. Griffin, M. R. Mayberg, and H. R. Winn, “Stereotactic radiosurgery: a review and comparison of methods.,” *JCO*, vol. 12, no. 5, pp. 1085–1099, May 1994, doi: 10.1200/JCO.1994.12.5.1085.
- [80] A. Jawahar *et al.*, “Stereotactic radiosurgery using the Leksell Gamma Knife: current trends and future directives,” *FBL*, vol. 9, no. 1, Art. no. 1, Jan. 2004, doi: 10.2741/1294.
- [81] E. J. Lehrer *et al.*, “Stereotactic Radiosurgery and Immune Checkpoint Inhibitors in the Management of Brain Metastases,” *International Journal of Molecular Sciences*, vol. 19, no. 10, Art. no. 10, Oct. 2018, doi: 10.3390/ijms19103054.
- [82] Y.-F. Zhou, “High intensity focused ultrasound in clinical tumor ablation,” *WJCO*, vol. 2, no. 1, p. 8, 2011, doi: 10.5306/wjco.v2.i1.8.
- [83] E. Vlaisavljevich *et al.*, “Effects of Ultrasound Frequency and Tissue Stiffness on the Histotripsy Intrinsic Threshold for Cavitation,” *Ultrasound in Medicine & Biology*, vol. 41, no. 6, pp. 1651–1667, Jun. 2015, doi: 10.1016/j.ultrasmedbio.2015.01.028.
- [84] C. Edsall, E. Ham, H. Holmes, T. L. Hall, and E. Vlaisavljevich, “Effects of frequency on bubble-cloud behavior and ablation efficiency in intrinsic threshold histotripsy,” *Phys. Med. Biol.*, vol. 66, no. 22, p. 225009, Nov. 2021, doi: 10.1088/1361-6560/ac33ed.
- [85] A. Hendricks-Wenger *et al.*, “Histotripsy Ablation in Preclinical Animal Models of Cancer and Spontaneous Tumors in Veterinary Patients: A Review,” *IEEE Trans. Ultrason., Ferroelect., Freq. Contr.*, vol. 69, no. 1, pp. 5–26, Jan. 2022, doi: 10.1109/TUFFC.2021.3110083.
- [86] J. Vidal-Jove *et al.*, “First-in-man histotripsy of hepatic tumors: the THERESA trial, a feasibility study,” *International Journal of Hyperthermia*, vol. 39, no. 1, pp. 1115–1123, Dec. 2022, doi: 10.1080/02656736.2022.2112309.
- [87] S. Qu *et al.*, “Non-thermal histotripsy tumor ablation promotes abscopal immune responses that enhance cancer immunotherapy,” *J Immunother Cancer*, vol. 8, no. 1, p. e000200, Jan. 2020, doi: 10.1136/jitc-2019-000200.
- [88] S. Tohme, R. L. Simmons, and A. Tsung, “Surgery for Cancer: A Trigger for Metastases,” *Cancer Research*, vol. 77, no. 7, pp. 1548–1552, Apr. 2017, doi: 10.1158/0008-5472.CAN-16-1536.
- [89] A. Eranki *et al.*, “High-Intensity Focused Ultrasound (HIFU) Triggers Immune Sensitization of Refractory Murine Neuroblastoma to Checkpoint Inhibitor Therapy,” *Clinical Cancer Research*, vol. 26, no. 5, pp. 1152–1161, Mar. 2020, doi: 10.1158/1078-0432.CCR-19-1604.

- [90] T. Worlikar *et al.*, “Impact of Histotripsy on Development of Intrahepatic Metastases in a Rodent Liver Tumor Model,” *Cancers*, vol. 14, no. 7, p. 1612, Mar. 2022, doi: 10.3390/cancers14071612.
- [91] N. Zhang *et al.*, “Insufficient Radiofrequency Ablation Treated Hepatocellular Carcinoma Cells Promote Metastasis by Up-Regulation ITGB3,” *J. Cancer*, vol. 8, no. 18, pp. 3742–3754, 2017, doi: 10.7150/jca.20816.
- [92] H. Liao *et al.*, “Thermal Ablation Induces Transitory Metastatic Growth by Means of the STAT3/c-Met Molecular Pathway in an Intrahepatic Colorectal Cancer Mouse Model,” *Radiology*, vol. 294, no. 2, pp. 464–472, Feb. 2020, doi: 10.1148/radiol.2019191023.
- [93] R. S. C. Cobbold, “Foundations of Biomedical Ultrasound,” p. 516, 2002.
- [94] J. Curie and P. Curie, “Développement par compression de l’électricité polaire dans les cristaux hémihédres à faces inclinées,” *Bulletin de Minéralogie*, vol. 3, no. 4, pp. 90–93, 1880, doi: 10.3406/bulmi.1880.1564.
- [95] K. Uchino, *Advanced Piezoelectric Materials: Science and Technology*. Woodhead Publishing, 2017.
- [96] W. A. Smith and B. A. Auld, “Modeling 1-3 composite piezoelectrics: thickness-mode oscillations,” *IEEE Transactions on Ultrasonics, Ferroelectrics and Frequency Control*, vol. 38, no. 1, pp. 40–47, Jan. 1991, doi: 10.1109/58.67833.
- [97] B. Hadimioglu and B. T. Khuri-Yakub, “Polymer films as acoustic matching layers,” in *IEEE Symposium on Ultrasonics*, Honolulu, HI, USA: IEEE, 1990, pp. 1337–1340. doi: 10.1109/ULTSYM.1990.171581.
- [98] R. Krimholtz, D. A. Leedom, and G. L. Matthaei, “New equivalent circuits for elementary piezoelectric transducers,” *Electronics Letters*, vol. 6, no. 13, pp. 398–399, Jun. 1970, doi: 10.1049/el:19700280.
- [99] J. Soneson, “HITU Simulator v2.0”, Accessed: Jun. 11, 2021. [Online]. Available: [https://github.com/jsoneson/HITU\\_Simulator](https://github.com/jsoneson/HITU_Simulator)
- [100] J. K. Woodacre, T. G. Landry, and J. A. Brown, “A Low-Cost Miniature Histotripsy Transducer for Precision Tissue Ablation,” *IEEE Transactions on Ultrasonics, Ferroelectrics, and Frequency Control*, vol. 65, no. 11, pp. 2131–2140, Nov. 2018, doi: 10.1109/TUFFC.2018.2869689.
- [101] M. G. Mallay, J. K. Woodacre, T. G. Landry, N. A. Campbell, and J. A. Brown, “A Dual-Frequency Lens-Focused Endoscopic Histotripsy Transducer,” *IEEE Trans. Ultrason., Ferroelect., Freq. Contr.*, vol. 68, no. 9, pp. 2906–2916, Sep. 2021, doi: 10.1109/TUFFC.2021.3078326.



- [102] T. L. Hall, J. B. Fowlkes, and C. A. Cain, “Imaging feedback of tissue liquefaction (histotripsy) in ultrasound surgery,” in *IEEE Ultrasonics Symposium, 2005.*, Rotterdam, The Netherlands: IEEE, 2005, pp. 1732–1734. doi: 10.1109/ULTSYM.2005.1603200.
- [103] H. Tang *et al.*, “Application of CUSA Excel ultrasonic aspiration system in resection of skull base meningiomas,” *Chin J Cancer Res*, vol. 26, no. 6, 2014.
- [104] D. A. Orringer, A. Golby, and F. Jolesz, “Neuronavigation in the surgical management of brain tumors: current and future trends,” *Expert Review of Medical Devices*, vol. 9, no. 5, pp. 491–500, Sep. 2012, doi: 10.1586/erd.12.42.
- [105] J. R. Sukovich *et al.*, “In vivo histotripsy brain treatment,” *Journal of Neurosurgery*, vol. 131, no. 4, pp. 1331–1338, Oct. 2019, doi: 10.3171/2018.4.JNS172652.
- [106] J. R. Sukovich *et al.*, “Targeted Lesion Generation Through the Skull Without Aberration Correction Using Histotripsy,” *IEEE Trans. Ultrason., Ferroelect., Freq. Contr.*, vol. 63, no. 5, pp. 671–682, May 2016, doi: 10.1109/TUFFC.2016.2531504.
- [107] T. Lee, W. Luo, Q. Li, H. Demirci, and L. J. Guo, “Laser-Induced Focused Ultrasound for Cavitation Treatment: Toward High-Precision Invisible Sonic Scalpel,” *Small*, vol. 13, no. 38, p. 1701555, Oct. 2017, doi: 10.1002/sml.201701555.
- [108] M. Belzberg *et al.*, “Minimally invasive therapeutic ultrasound: Ultrasound-guided ultrasound ablation in neuro-oncology,” *Ultrasonics*, vol. 108, p. 106210, Dec. 2020, doi: 10.1016/j.ultras.2020.106210.
- [109] H. Kim *et al.*, “Miniaturized Intracavitary Forward-Looking Ultrasound Transducer for Tissue Ablation,” *IEEE Trans. Biomed. Eng.*, vol. 67, no. 7, pp. 2084–2093, Jul. 2020, doi: 10.1109/TBME.2019.2954524.
- [110] K.-W. Lin, A. P. Duryea, Y. Kim, T. L. Hall, Z. Xu, and C. A. Cain, “Dual-beam histotripsy: a low-frequency pump enabling a high-frequency probe for precise lesion formation,” *IEEE Trans. Ultrason., Ferroelect., Freq. Contr.*, vol. 61, no. 2, pp. 325–340, Feb. 2014, doi: 10.1109/TUFFC.2014.6722617.
- [111] J. Ma, S. Guo, D. Wu, X. Geng, and X. Jiang, “Design, fabrication, and characterization of a single-aperture 1.5-MHz/3-MHz dual-frequency HIFU transducer,” *IEEE Trans. Ultrason., Ferroelect., Freq. Contr.*, vol. 60, no. 7, pp. 1519–1529, Jul. 2013, doi: 10.1109/TUFFC.2013.2724.
- [112] Y. Sato, K. Mizutani, N. Wakatsuki, and T. Nakamura, “Design for an Aspherical Acoustic Fresnel Lens with Phase Continuity,” *Jpn. J. Appl. Phys.*, vol. 47, no. 5, pp. 4354–4359, May 2008, doi: 10.1143/JJAP.47.4354.

- [113] J. Ma, M. B. Steer, and X. Jiang, “An acoustic filter based on layered structure,” *Applied Physics Letters*, vol. 106, no. 11, p. 111903, Mar. 2015, doi: 10.1063/1.4915100.
- [114] M. Toda and M. Thompson, “Novel multi-layer polymer-metal structures for use in ultrasonic transducer impedance matching and backing absorber applications,” *IEEE Trans. Ultrason., Ferroelect., Freq. Contr.*, vol. 57, no. 12, pp. 2818–2827, Dec. 2010, doi: 10.1109/TUFFC.2010.1755.
- [115] X. Z. L. Luo and H. Luo, *Advanced piezoelectric materials : science and technology*. Woodhead Publishing, 2010.
- [116] S. Zhang, F. Li, X. Jiang, J. Kim, J. Luo, and X. Geng, “Advantages and challenges of relaxor-PbTiO<sub>3</sub> ferroelectric crystals for electroacoustic transducers – A review,” *Progress in Materials Science*, vol. 68, pp. 1–66, Mar. 2015, doi: 10.1016/j.pmatsci.2014.10.002.
- [117] A. Bezanson, R. Adamson, and J. A. Brown, “Fabrication and performance of a miniaturized 64-element high-frequency endoscopic phased array,” *IEEE Trans. Ultrason., Ferroelect., Freq. Contr.*, vol. 61, no. 1, pp. 33–43, Jan. 2014, doi: 10.1109/TUFFC.2014.6689774.
- [118] C. A. Samson, A. Bezanson, and J. A. Brown, “A Sub-Nyquist, Variable Sampling, High-Frequency Phased Array Beamformer,” *IEEE Trans. Ultrason., Ferroelect., Freq. Contr.*, vol. 64, no. 3, pp. 568–576, Mar. 2017, doi: 10.1109/TUFFC.2016.2646925.
- [119] J. A. Brown and G. R. Lockwood, “Low-cost, high-performance pulse generator for ultrasound imaging,” *IEEE Trans. Ultrason., Ferroelect., Freq. Contr.*, vol. 49, no. 6, pp. 848–851, Jun. 2002, doi: 10.1109/TUFFC.2002.1009345.
- [120] K. Morris, A. Rosenkranz, H. Seibert, L. Ringel, S. Diebels, and F. E. Talke, “Uniaxial and biaxial testing of 3D printed hyperelastic photopolymers,” *J of Applied Polymer Sci*, vol. 137, no. 8, p. 48400, Feb. 2020, doi: 10.1002/app.48400.
- [121] D. Chauvet *et al.*, “In Vivo Measurement of Brain Tumor Elasticity Using Intraoperative Shear Wave Elastography,” *Ultraschall in Med*, vol. 37, no. 06, pp. 584–590, Apr. 2015, doi: 10.1055/s-0034-1399152.
- [122] T. Li, T. Khokhlova, O. Sapozhnikov, M. O’Donnell, and J. Hwang, “A new active cavitation mapping technique for pulsed HIFU applications-bubble doppler,” *IEEE Trans. Ultrason., Ferroelect., Freq. Contr.*, vol. 61, no. 10, pp. 1698–1708, Oct. 2014, doi: 10.1109/TUFFC.2014.006502.
- [123] A. Shi, Z. Xu, J. Lundt, H. A. Tamaddoni, T. Worlikar, and T. L. Hall, “Integrated Histotripsy and Bubble Coalescence Transducer for Rapid Tissue Ablation,” *IEEE Trans. Ultrason., Ferroelect., Freq. Contr.*, vol. 65, no. 10, pp. 1822–1831, Oct. 2018, doi: 10.1109/TUFFC.2018.2858546.

- [124] G. Maimbourg, A. Houdouin, T. Deffieux, M. Tanter, and J.-F. Aubry, “Steering Capabilities of an Acoustic Lens for Transcranial Therapy: Numerical and Experimental Studies,” *IEEE Trans. Biomed. Eng.*, vol. 67, no. 1, pp. 27–37, Jan. 2020, doi: 10.1109/TBME.2019.2907556.
- [125] M. Mallay, T. Landry, J. Woodacre, and J. Brown, “An Endoscopic Tri-Frequency (1 MHz, 5 MHz, 30 MHz) Transducer for Combined Imaging and Therapy,” in *2020 IEEE International Ultrasonics Symposium (IUS)*, Sep. 2020, pp. 1–4. doi: 10.1109/IUS46767.2020.9251631.
- [126] M. Mallay *et al.*, “Evaluation of Piezoelectric Ceramics for use in Miniature Histotripsy Transducers,” in *2022 IEEE International Ultrasonics Symposium (IUS)*, Oct. 2022, pp. 1–4. doi: 10.1109/IUS54386.2022.9957153.
- [127] D. Jiang, N. Choudhury, V. Mora, and S. Delorme, “Characterization of Suction and CUSA Interaction with Brain Tissue,” in *Biomedical Simulation*, F. Bello and S. Cotin, Eds., in *Lecture Notes in Computer Science*. Berlin, Heidelberg: Springer, 2010, pp. 11–19. doi: 10.1007/978-3-642-11615-5\_2.
- [128] J. R. Sukovich, J. J. Macoskey, J. E. Lundt, T. I. Gerhardson, T. L. Hall, and Z. Xu, “Real-Time Transcranial Histotripsy Treatment Localization and Mapping Using Acoustic Cavitation Emission Feedback,” *IEEE Transactions on Ultrasonics, Ferroelectrics, and Frequency Control*, vol. 67, no. 6, pp. 1178–1191, Jun. 2020, doi: 10.1109/TUFFC.2020.2967586.
- [129] S. Zhang, R. Xia, L. Lebrun, D. Anderson, and T. R. Shrout, “Piezoelectric materials for high power, high temperature applications,” *Materials Letters*, vol. 59, no. 27, pp. 3471–3475, Nov. 2005, doi: 10.1016/j.matlet.2005.06.016.
- [130] J. K. Woodacre, T. G. Landry, and J. A. Brown, “Fabrication and Characterization of a 5 mm × 5 mm Aluminum Lens-Based Histotripsy Transducer,” *IEEE Trans. Ultrason., Ferroelect., Freq. Contr.*, vol. 69, no. 4, pp. 1442–1451, Apr. 2022, doi: 10.1109/TUFFC.2022.3152174.
- [131] T. G. Landry, M. G. Mallay, and J. A. Brown, “A Simple and Cost-Effective Benchtop Setup for Assessing Ultrasound-Induced Inertial Cavitation Probability,” *IEEE Sens. Lett.*, vol. 7, no. 6, pp. 1–4, Jun. 2023, doi: 10.1109/LSSENS.2023.3282076.
- [132] W. Ren, A. J. Masys, G. Yang, and B. K. Mukherjee, “The field and frequency dependence of the strain and polarisation in piezoelectric and electrostrictive ceramics,” *Ferroelectrics*, vol. 261, no. 1, pp. 27–32, Jan. 2001, doi: 10.1080/00150190108216260.
- [133] J. Woodacre and J. Brown, “An evaluation of PZT5A, PIN-PMN-PT Single Crystal, and High-Dielectric PZT for a 5mm x 5mm Histotripsy Transducer,” in *2019 IEEE International Ultrasonics Symposium (IUS)*, Oct. 2019, pp. 2596–2599. doi: 10.1109/ULTSYM.2019.8925688.

- [134] M. M. Grabowski *et al.*, “Residual tumor volume versus extent of resection: predictors of survival after surgery for glioblastoma: Clinical article,” *Journal of Neurosurgery*, vol. 121, no. 5, pp. 1115–1123, Nov. 2014, doi: 10.3171/2014.7.JNS132449.
- [135] L. Barazzuol, R. P. Coppes, and P. van Luijk, “Prevention and treatment of radiotherapy-induced side effects,” *Molecular Oncology*, vol. 14, no. 7, pp. 1538–1554, 2020, doi: 10.1002/1878-0261.12750.
- [136] A. Franzini *et al.*, “Ablative brain surgery: an overview,” *International Journal of Hyperthermia*, vol. 36, no. 2, pp. 64–80, Oct. 2019, doi: 10.1080/02656736.2019.1616833.
- [137] L. Marenco-Hillebrand, K. Alvarado-Estrada, and K. L. Chaichana, “Contemporary Surgical Management of Deep-Seated Metastatic Brain Tumors Using Minimally Invasive Approaches,” *Front. Oncol.*, vol. 8, p. 558, Nov. 2018, doi: 10.3389/fonc.2018.00558.
- [138] J. K. Woodacre, M. Mallay, and J. A. Brown, “Fabrication and characterization of a flat aperture Fresnel lens based histotripsy transducer,” *Ultrasonics*, vol. 131, p. 106934, May 2023, doi: 10.1016/j.ultras.2023.106934.
- [139] G. E. Stocker, M. Zhang, Z. Xu, and T. L. Hall, “Endocavity Histotripsy for Efficient Tissue Ablation—Transducer Design and Characterization,” *IEEE Trans. Ultrason., Ferroelect., Freq. Contr.*, vol. 68, no. 9, pp. 2896–2905, Sep. 2021, doi: 10.1109/TUFFC.2021.3055138.
- [140] E. Vlaisavljevich, A. Maxwell, M. Warnez, E. Johnsen, C. A. Cain, and Z. Xu, “Histotripsy-induced cavitation cloud initiation thresholds in tissues of different mechanical properties,” *IEEE Transactions on Ultrasonics, Ferroelectrics, and Frequency Control*, vol. 61, no. 2, pp. 341–352, Feb. 2014, doi: 10.1109/TUFFC.2014.6722618.
- [141] K. Miller, K. Chinzei, G. Orsengo, and P. Bednarz, “Mechanical properties of brain tissue in-vivo: experiment and computer simulation,” *Journal of Biomechanics*, vol. 33, no. 11, pp. 1369–1376, Nov. 2000, doi: 10.1016/S0021-9290(00)00120-2.

## APPENDIX A:

### COPYRIGHT PERMISSION


#### Figure 2.1:

This is an Open-Access article distributed under the terms of the Creative Commons Attribution Non-Commercial License (<http://creativecommons.org/licenses/by-nc/3.0/>) which permits unrestricted non-commercial use, distribution, and reproduction in any medium, provided the original work is properly cited.

#### Figure 2.2:

			
This is a License Agreement between Matthew Mallay ("User") and Copyright Clearance Center, Inc. ("CCC") on behalf of the Rightsholder identified in the order details below. The license consists of the order details, the Marketplace Permissions General Terms and Conditions below, and any Rightsholder Terms and Conditions which are included below. All payments must be made in full to CCC in accordance with the Marketplace Permissions General Terms and Conditions below.			
Order Date	28-Dec-2023	Type of Use	Republish in a thesis/dissertation
Order License ID	1431626-1	Publisher	RADIOLOGICAL SOCIETY OF NORTH AMERICAN
ISSN	1527-1315	Portion	Image/photo/illustration
<b>LICENSED CONTENT</b>			
Publication Title	Radiology	Publication Type	e-Journal
Article Title	Principles of and advances in percutaneous ablation.	Start Page	351
Author/Editor	Radiological Society of North America.	End Page	369
Date	01/01/1923	Issue	2
Language	English	Volume	258
Country	United States of America	URL	<a href="http://radiology.rsna.org/">http://radiology.rsna.org/</a>
Rightsholder	Radiological Society of North America		
<b>REQUEST DETAILS</b>			
Portion Type	Image/photo/illustration	Distribution	Worldwide
Number of Images / Photos / Illustrations	3	Translation	Original language of publication
Format (select all that apply)	Print, Electronic	Copies for the Disabled?	No
Who Will Republish the Content?	Academic Institution	Minor Editing Privileges?	No
Duration of Use	Life of current edition	Incidental Promotional Use?	No
Lifetime Unit Quantity	Up to 499	Currency	CAD
Rights Requested	Main product		
<b>NEW WORK DETAILS</b>			
Title	AN ULTRASOUND ENDOSCOPE FOR COMBINED IMAGING AND CAVITATION-BASED ABLATION	Institution Name	Dalhousie University
Instructor Name	Matthew Mallay	Expected Presentation Date	2024-02-29
<b>ADDITIONAL DETAILS</b>			
The Requesting Person / Organization to Appear on the License	Matthew Mallay		
<b>REQUESTED CONTENT DETAILS</b>			
Title, Description or Numeric Reference of the Portion(s)	Figure 5, 7 and 8	Title of the Article / Chapter the Portion Is From	Principles of and advances in percutaneous ablation.
Editor of Portion(s)	Ahmed, Muneeb; Brace, Christopher L; Lee, Fred T; Goldberg, S Nahum	Author of Portion(s)	Ahmed, Muneeb; Brace, Christopher L; Lee, Fred T; Goldberg, S Nahum
Volume / Edition	258	Publication Date of Portion	2011-02-01
Page or Page Range of Portion	351-369		

**Figure 2.3:**



**Decalcification of a Heavily Calcified Common Femoral Artery and its Bifurcation with a Cavitron Ultrasonic Surgical Aspirator**

Author: S. Maeda, T. Nakamura  
Publication: EJVES Short Reports  
Publisher: Elsevier  
Date: 2017

© 2016 The Author(s). Published by Elsevier Ltd on behalf of European Society for Vascular Surgery.

**Creative Commons Attribution-NonCommercial-No Derivatives License (CC BY NC ND)**

This article is published under the terms of the [Creative Commons Attribution-NonCommercial-No Derivatives License \(CC BY NC ND\)](#). For non-commercial purposes you may copy and distribute the article, use portions or extracts from the article in other works, and text or data mine the article, provided you do not alter or modify the article without permission from Elsevier. You may also create adaptations of the article for your own personal use only, but not distribute these to others. You must give appropriate credit to the original work, together with a link to the formal publication through the relevant DOI, and a link to the Creative Commons user license above. If changes are permitted, you must indicate if any changes are made but not in any way that suggests the licensor endorses you or your use of the work.

Permission is not required for this non-commercial use. For commercial use please continue to request permission via RightsLink.

[BACK](#) [CLOSE WINDOW](#)

**Figure 2.4a:**

**Authors Rights and Permissions**

Papers published in Volumes 1 Issue 1–Volume 26 Issue 4 (from 1996 to January 2021) are copyright IMR Press.

**Permission is not required when:**

IMR Press grants any third party the right to use the article freely, so long as its integrity is maintained and its original authors, citation details and publisher are identified.

Permission is not required to use original figures or tables for non-commercial and educational use (e.g., in a review article, or in a book that is not for sale) if the article is copyright IMR Press. Please include the full journal reference and, for articles published in Volumes 1 Issue 1–Volume 26 Issue 4 (from 1996 to January 2021), include "Copyright (copyright year) IMR Press" as a copyright note.

Starting from 1 February 2021, all *FBL* content is available online and is fully browsable and searchable. Articles published beginning from Volume 26 Issue 5 (2021) are under the terms and conditions of the [CC BY license](#). *FBL* is not authorized to grant permission for material published under either license, as the authors retain copyright. However, depending on the intended use, permission may not be required at all. For details, see: [Copyright & License](#).

IMR Press will insert the following note on the first page of the published text:

© Year The Author(s). Published by IMR Press. This is an open access article under the [CC BY 4.0 license](#).

**Figure 2.4b:**

## MDPI Open Access Information and Policy

All articles published by MDPI are made immediately available worldwide under an open access license. This means:

- everyone has free and unlimited access to the full-text of *all* articles published in MDPI journals;
- everyone is free to re-use the published material if proper accreditation/citation of the original publication is given;
- open access publication is supported by the authors' institutes or research funding agencies by payment of a comparatively low **Article Processing Charge (APC)** for accepted articles.

### Permissions

No special permission is required to reuse all or part of article published by MDPI, including figures and tables. For articles published under an open access Creative Common CC BY license, any part of the article may be reused without permission provided that the original article is clearly cited. Reuse of an article does not imply endorsement by the authors or MDPI.

**Figure 2.5:**

## MDPI Open Access Information and Policy


All articles published by MDPI are made immediately available worldwide under an open access license. This means:

- everyone has free and unlimited access to the full-text of *all* articles published in MDPI journals;
- everyone is free to re-use the published material if proper accreditation/citation of the original publication is given;
- open access publication is supported by the authors' institutes or research funding agencies by payment of a comparatively low **Article Processing Charge (APC)** for accepted articles.

### Permissions

No special permission is required to reuse all or part of article published by MDPI, including figures and tables. For articles published under an open access Creative Common CC BY license, any part of the article may be reused without permission provided that the original article is clearly cited. Reuse of an article does not imply endorsement by the authors or MDPI.

**Figure 2.14 and 2.15:**



**Requesting permission to reuse content from an IEEE publication**

**A Low-Cost Miniature Histotripsy Transducer for Precision Tissue Ablation**

Author: Jeffrey K. Woodacre  
Publication: IEEE Transactions on Ultrasonics, Ferroelectrics, and Frequency Control  
Publisher: IEEE  
Date: November 2018  
Copyright © 2018, IEEE

**Thesis / Dissertation Reuse**

The IEEE does not require individuals working on a thesis to obtain a formal reuse license, however, you may print out this statement to be used as a permission grant:

*Requirements to be followed when using any portion (e.g., figure, graph, table, or textual material) of an IEEE copyrighted paper in a thesis:*

- 1) In the case of textual material (e.g., using short quotes or referring to the work within these papers) users must give full credit to the original source (author, paper, publication) followed by the IEEE copyright line © 2011 IEEE.
- 2) In the case of illustrations or tabular material, we require that the copyright line © [Year of original publication] IEEE appear prominently with each reprinted figure and/or table.
- 3) If a substantial portion of the original paper is to be used, and if you are not the senior author, also obtain the senior author's approval.

*Requirements to be followed when using an entire IEEE copyrighted paper in a thesis:*

- 1) The following IEEE copyright/ credit notice should be placed prominently in the references: © [year of original publication] IEEE. Reprinted, with permission, from [author names, paper title, IEEE publication title, and month/year of publication]
- 2) Only the accepted version of an IEEE copyrighted paper can be used when posting the paper or your thesis on-line.
- 3) In placing the thesis on the author's university website, please display the following message in a prominent place on the website: In reference to IEEE copyrighted material which is used with permission in this thesis, the IEEE does not endorse any of [university/educational entity's name goes here]'s products or services. Internal or personal use of this material is permitted. If interested in reprinting/republishing IEEE copyrighted material for advertising or promotional purposes or for creating new collective works for resale or redistribution, please go to [http://www.ieee.org/publications\\_standards/publications/rights/rights\\_link.html](http://www.ieee.org/publications_standards/publications/rights/rights_link.html) to learn how to obtain a License from RightsLink.

If applicable, University Microfilms and/or ProQuest Library, or the Archives of Canada may supply single copies of the dissertation.